A Numerical Model for Short-term Sea Ice Forecasting in the Arctic

Ein numerisches Modell zur Meereisvorhersage in der Arktis

Jan Leonhard Lieser

Jan L. Lieser

Alfred-Wegener-Institut für Polar- und Meeresforschung
Postfach 120161
27515 Bremerhaven
Germany

The Arctic is an ocean
that plays at being land;
each little ridge and wrinkle stands,
as on a map, as larger than it self.

Here melt-pond solid seas
form over a liquid mantle -
geology's reversed! Continental
plates of ice collide to form

pressure-ridge mountain chains.
The illusion stands,
solid, almost, as real land;
until the POLARSTERN comes crashing through,

to remind the Arctic Ocean
that for all its grandeur,
it's really only water,
sailed by ships and sailors (and even scientists).

But then comes the Arctic winter
and by degrees, we're slowly squeezed
south; and the ocean closes up
behind us, like a zipper.

Andrew Feld (2001)

Contents

List of Figures

Abstract

The passage through the Arctic Ocean is the shortest sea route from European harbours to south-east Asian harbours (and vice versa). Also, bulk cargo and natural resources from high Arctic production locations can be transported with cargo ships through the coastal seas. However, less solar irradiation north of $70\,^\circ$ N and even no illumination during polar night in winter results in cold air temperatures and thus freezing of sea water forming sea ice. The Arctic sea ice extent varies between $\sim 9{\cdot}10^6$ km^2 in summer and $\sim 13{\cdot}10^6$ km^2 in winter. A major part of the sea ice is so called second and/or multi year ice and has a typical thickness of 1.5 to 2.5 m. Sea ice not only a very important variable in the Earth's climate system, but also represents a very effective barrier for ships in this region. Nowadays, modern and powerful icebreakers and specially designed and reinforced cargo ships are able to cope with these circumstances under favourable conditions.

Currently, decisions regarding route planning for ships sailing through ice-covered Arctic waters are based on remote sensing data, available daily, and on the knowledge and experience of ice pilots. This study presents a numerical model for predicting sea ice conditions in the Arctic for 5-10 days, providing an additional tool for the planning process. It is a dynamic-thermodynamic sea ice model applying a viscous-plastic rheology with a horizontal resolution of $^1\!/_4$ degree and a time step of 6 hours. For this thesis the model has been embedded in a forecast setting. A fast-ice parametrization is implemented to simulate off-shore polynyas, which are important for coastal shipping traffic. New oceanic forcing conditions showing a seasonal variability are used. Atmospheric forcing is obtained from the European Centre for Medium-Range Weather Forecasts (ECMWF) analyses/forecasts.

The best possible analysis of the current state of the sea ice concentration in the Arctic is achieved by assimilation of remote sensing data into the numerical model. This analysis is used as starting condition for a short term integration of the numerical model for the prediction of sea ice conditions (e.g. concentration and thickness). The results shown for two sample cases demonstrate, that the numerical model is not only able to reproduce past sea ice conditions for climatological studies, but also to forecast sea ice on short time scales.

Zusammenfassung

Die Passage durch den Arktischen Ozean ist der kürzeste Seeweg von europäischen Häfen zu Häfen in Südost-Asien (und umgekehrt). Außerdem können Massengüter und Rohstoffe von Produktionsstätten in der Arktis mit Frachtern entlang der Küstengewässer transportiert werden. Wenig Sonneneinstrahlung nördlich von $70\,^\circ$ N und gar keine Einstrahlung während des Polarwinters führen allerdings zu sehr niedrigen Lufttemperaturen und damit zur Bildung von Meereis. Das arktische Meereis bedeckt im Sommer etwa $9{\cdot}10^6$ km^2 des arktischen Ozeans, im Winter dehnt es sich bis auf $13{\cdot}10^6$ km^2 aus. Ein Großteil dieses Meereises besteht aus so genanntem mehrjährigem Eis und hat eine typische Dicke von 1.5 bis 2.5 m. Es ist nicht nur ein wichtiger Faktor des Klimasystems der Erde sondern stellt auch eine sehr effektive Barriere für die Schifffahrt in dieser Region dar. Moderne und kraftvolle Eisbrecher und speziell eisverstärkte Massengutfrachter können heutzutage mit diesen äußeren Umständen unter günstigen Bedingungen gut umgehen.

Derzeit werden Routen für Schiffe durch eisbedeckte Gewässer auf der Basis von täglich zur Verfügung stehenden Satellitendaten und dem Wissen und der Erfahrung von Eislotsen geplant. In dieser Arbeit wird ein numerisches Modell vorgestellt, mit dem die Eisverhältnisse für 5-10 Tage vorhergesagt werden können, was somit eine weitere Informationsquelle für den Planungsprozess darstellt. Das dynamisch-thermodynamische Meereismodell mit viskos-plastischer Rheologie wird mit einer horizontalen Auflösung von $^1/_4$ Grad und einem Zeitschritt von 6 Stunden betrieben. Es ist eine neue Festeis-Parametrisierung implementiert, die es erlaubt, küstennahe Polynien vorherzusagen, die für die Schifffahrt von großer Bedeutung sind. Außerdem sind neue ozeanische Randbedingungen mit saisonaler Variabilität installiert. Analysen/Vorhersagen des Europäischen Zentrums für Mittelfrist-Wettervorhersagen (ECMWF) werden als atmosphärische Antriebsdaten verwendet.

Für eine bestmögliche Beschreibung des Status der Meereiskonzentration in der Arktis werden Fernerkundungsdaten in das numerische Modell assimiliert. Eine solche Analyse wird als Startbedingung für eine anschließende Integration des Modells verwendet, um Eisparameter wie Eiskonzentration und Eisdicke vorherzusagen. Die Ergebnisse aus zwei Beispielstudien zeigen, daß das Modell nicht nur in der Lage ist, vergangene Eisverhältnisse für klimatologische Studien realistisch zu reproduzieren, sondern auch für kurze Zeiten vorherzusagen.

List of Acronyms

AARI:	Arctic and Antarctic Research Institute, Russia
AMI:	Active Microwave Instrument
AO:	Arctic Oscillation
ARCDEV:	Arctic Demonstration and Exploratory Voyage
AVHRR:	Advanced Very High Resolution Radiometer
BLUE:	Best Linear Unbiased Estimator
DMSP:	Defense Meteorological Satellite Program
ECMWF:	European Centre for Medium-Range Weather Forecasts
EMI:	Electromagnetic induction
ERS:	European Remote Sensing Satellites
ESA:	European Space Agency
FOV:	Field of View
GCM:	General Circulation Model
GFDL:	Geophysical Fluid Dynamics Laboratory
IBCAO:	International Bathymetric Chart of the Arctic Ocean
MOM:	Modular Ocean Model
NAO:	North Atlantic Oscillation
NASA:	National Aeronautics and Space Agency
NCEP:	National Centers for Environmental Prediction
NOAA:	National Oceanic and Atmospheric Administration
NOGAPS:	Navy Operational Global Atmospheric Prediction System
NSIDC:	National Snow and Ice Data Center
NSR:	Northern Sea Route
OI:	Optimal Interpolation
OLS:	Operational Linescan System
RA:	Radar Altimeter
RMSE:	Root Mean Square Error
SAR:	Synthetic Aperture Radar
SCM:	Successive Correction Method
SHEBA:	Surface Heat Budget of the Arctic Ocean
SIMIP:	Sea Ice Model Intercomparison Project
SIOM:	Sea Ice Ocean Model
SSM/I:	Special Sensor Microwave / Imager

Chapter 1

Introduction

Recently, much effort was made to improve the climatological component *sea ice* in numerical climate models. Most large scale coupled atmosphere-ocean general circulation models (GCMs) treat sea ice in an unsatisfactory manner but show the most dramatic response to changes in greenhouse gases in the polar regions. For instance, increasing CO_2 concentrations in the atmosphere will lead to increasing air temperatures with amplified frequencies in higher latitudes, which will most likely have an effect on the sea ice cover. At this time, numerical sea ice models have reached a level where it is possible to use them for short term sea ice forecasting.

In this work, a numerical model for Arctic sea ice will be presented and some attempts are made at predicting the sea ice state for a period of some days. To do so, it is necessary to know the physical laws which tell us something about the evolution of the physical variables and to have the best estimate of the initial conditions for these parameters.

1.1 Sea Ice and Climate

The Earth's climate system includes the atmosphere, the hydrosphere, the biosphere and the cryosphere.These subsystems are variably inter-connected. Owing to the specific conditions of the Earth's orbit around the sun all three phases of water (gaseous, liquid, and solid) are present at any time in these spheres. Most of the water is stored in the liquid phase in oceans, lakes, and rivers covering about 70% of the Earth's surface. In the atmosphere, water is transported as water vapour and as condensed water in clouds in liquid and solid phase. This water is eventually released as precipitation (e.g. rain or snow) over land or ocean, contributing to ice cover in cold regions.

Sea ice and its snow cover play a key role throughout the year in the energy balance and in the fresh water fluxes driving the ocean circulation. The
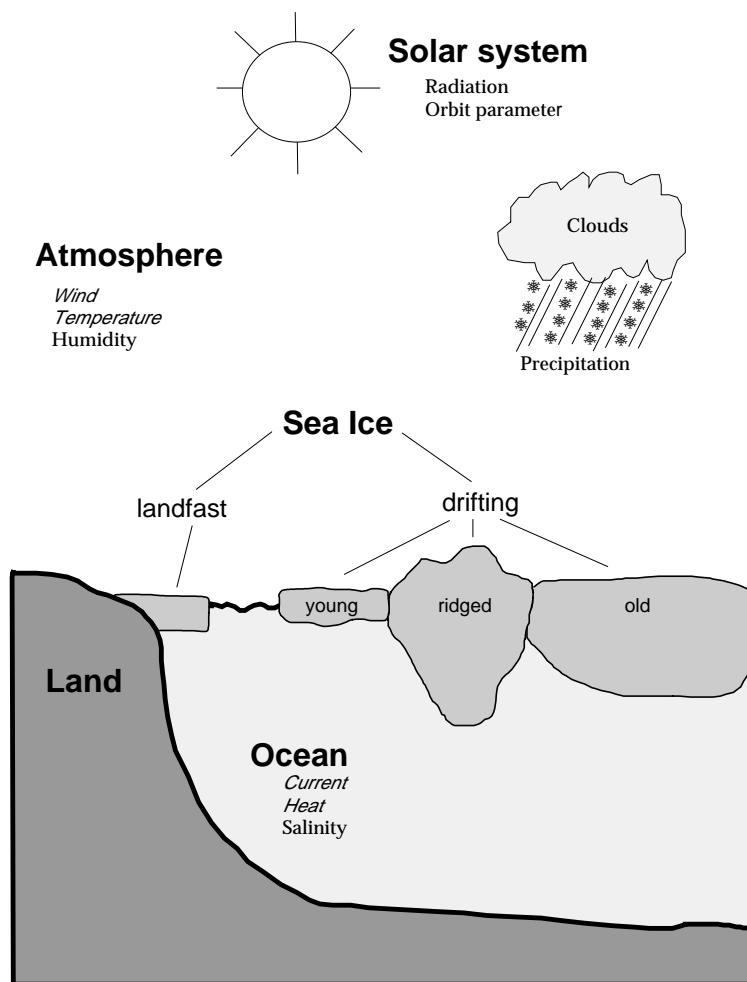
Figure 1.1: Sea ice in the climate system. Sea ice forms on the sea surface at high latitudes and thus modifies the interaction between the atmosphere and the ocean. Thermodynamic growth and decay are prescribed through the energy balance (including atmospheric and oceanic heat fluxes and heat conduction), whereas dynamic variables (e.g. drift velocities) can be determined from the momentum balance (including the effects of wind and ocean currents).

exchange of heat, moisture, momentum, and matter between the atmosphere and the ocean is reduced if sea ice is present, because it effectively separates the atmosphere from the ocean. Figure 1.1 presents a schematic picture of sea ice in the climate system. The properties of the sea ice cover are important during the summer season, when solar radiation is at it's maximum. However, in summer the sea ice properties change dramatically from a mostly compact, snow-covered surface during winter (see Figure 1.2) to an aged one comprising deteriorated snow, melt ponds and many open leads. Shrinking ice cover leads to more absorption of heat in the ocean, due to a reduction in the overall surface albedo. A warmed ice cover releases fresh water and transported contaminants as it melts. Freezing of sea water releases brine, owing to the ice crystal structure, which can not incorporate salt.

Sea ice is also an important habitat for biota living in brine channels or on the ice underside. More light penetrating a thinner ice cover to reach the upper parts of the water column stimulates biological activity, and a major part of the Arctic Ocean food chain is found within a few meters of sea ice and on the ice underside. The heat absorbed by the water could be released from the ocean again elsewhere and this may entail more exchange of moisture as well as a change in the circulation scheme of the ocean. Increased fluxes to the atmosphere will affect pressure systems, which again have an influence on the ice cover (e.g. by pushing ice floes around) and might finally change the environmental conditions for living creatures (polar animals as well as humans living close to polar regions). So, a change in one of the sub-systems of the Earth's climate will be followed by changes in the other sub-systems (see, for example, Smedsrud and Furevik, 2000).

The cryosphere is composed of bodies of water in its solid form. This includes sea ice as well as snow cover, glaciers and ice sheets, river ice, lake ice, seasonally frozen ground and permafrost. The word cryosphere comes from the ancient greek word $\kappa\rho\upsilon\sigma\varsigma$, meaning frost or icy cold. The cryosphere is an integral and important part of the Earth's dynamic systems. Feedback processes concerning surface energy and moisture exchange between the cryosphere, the hydrosphere and the atmosphere are a major factor in the evolution of global climate. Landscape changes result from the movement of land ice and changes in frozen ground, while storage of water in snow and ice is the major source of fresh water for many of the Earth's hydrological systems. Within the context of global change, concomitant changes in the extent of the cryosphere will have significant repercussions on climate, landscape processes, hydrological reservoirs of fresh water and associated socio-economic activities. Improved methods are needed to track the dynamics of the cryosphere because of difficulties in accomplishing this with standard point measurements. Methods for up-scaling from local measurements to larger areas must also be developed. Techniques of remote sensing are proving to be valuable research tools in elucidating and tracking the evolution of processes of the cryosphere and in the development of models for cryospheric systems.

Extent and thickness of the sea ice cover are sensitive indicators for the state of the Earth's climate, although it covers only 7% of the surface. On geological time scales the climate system shows large temperature variations, e.g. in sediment cores from Arctic sub-basins, indicating a highly variable sea ice cover (Spielhagen et al., 1997). The tracers found in those sediment cores are, for example, abundances and stable isotope compositions of microfossils which are included in the sediment under certain climatological conditions. High amounts of planktonic microfossils indicate relatively warm waters with a high
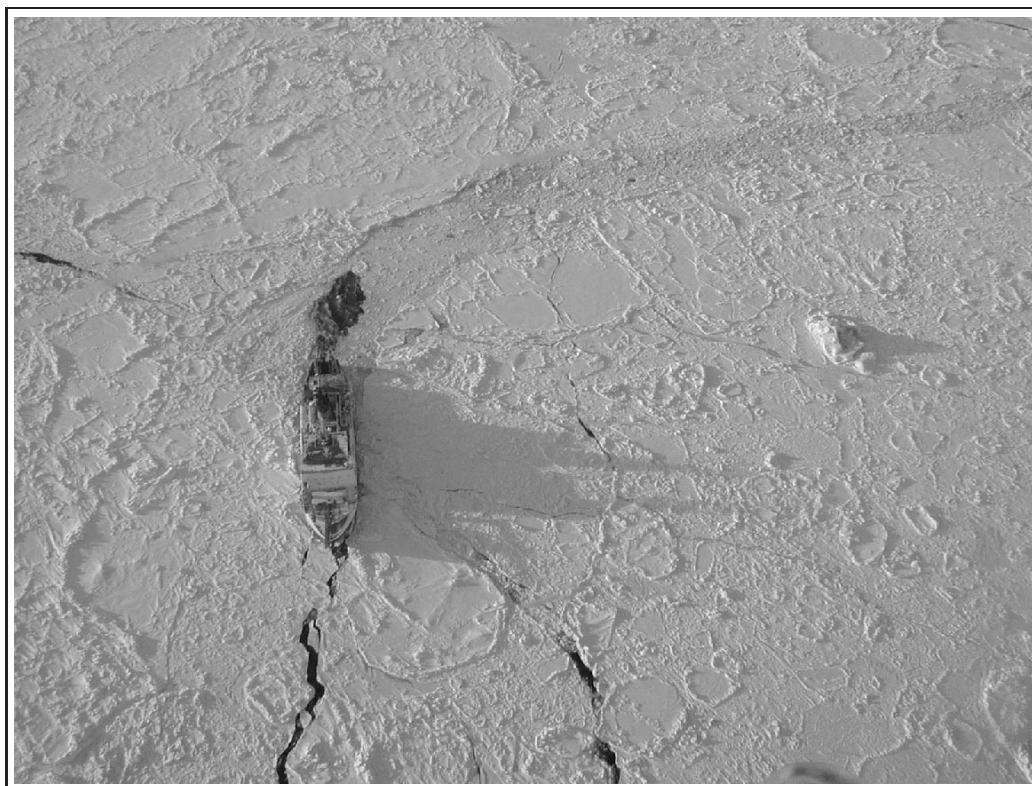
Figure 1.2: RV POLARSTERN in winterly conditions in the Arctic. Older sea ice floes of different size embedded in younger ice are visible in this photograph taken at a height of approximately 1000 ft. The ship-track (coming from the upper right corner) is ice covered immediately behind the ship. The ship is following a small crack to make best possible progress.

biological productivity and only a seasonal or even no ice cover, whereas layers with large quantities of coarse terrigenous ice-rafted detritus point to thick sea ice covers or even glaciation reaching far north from northern North America and/or northern Eurasia (Nørgaard-Pedersen et al., 1998). Coarse detritus was either transported by drifting icebergs from continental ice sheets (own observations in the eastern Arctic Ocean, 2001) or, in extreme cases, by ice shelves extending from land based glaciers (Polyak et al., 2001). Sediments can also be included in the sea ice during the freezing process on the Eurasian shelf region and then be transported through the ocean basin and released once the ice melts (Kolatschek, 1998).

Sea ice reacts not only passively to climate variations but also has an active influence for several reasons. The high albedo (the ratio of reflected to incoming radiation) of sea ice has a major influence on the Earth's radiation budget. Especially if the sea ice is covered with fresh snow, the albedo reaches values between 0.8 and 0.9. This acts like a sink for solar radiation, the main driving source for climate variations. This increases the meridional atmospheric temperature gradient between the poles and the Equator, which leads to intensified

westerly winds in the mid-latitudes. The dark ocean absorbs much more solar radiation and has a low albedo of about 0.1. Another important factor is the low thermal conductivity of sea ice, which makes it a heat insulator between the atmosphere, with minimum temperatures down to -30° C in winter in the central Arctic, and the relatively warm ocean near the freezing point of -1.8° C. Sea water is a composite of different materials (e.g. salts, solute gases, particles, live and dead organisms), so the forming sea ice is usually modified from being just frozen water. This leads also to a lowered freezing temperature compared to pure water. The heat exchange between the ocean and the atmosphere can easily reach values up to several 100 W/m^2. Just a thin layer of ice can reduce the transfer of latent and sensible heat significantly. With a thick ice cover these values are reduced by two orders of magnitude. A closed sea ice cover also alters the transfer of momentum from the atmosphere to the ocean. The shear stress caused by wind depends on the surface roughness of the ocean. Ocean waves are attenuated by sea ice and thus the momentum transfer is reduced. Storms can break up a sea ice cover and increase sea ice thickness locally by deforming the ice, building pressure ridges or overlapping ice floes. On the other hand, deformed sea ice with sails and keels reaching deep into the atmospheric and oceanic boundary layers respectively, intensifies the dynamic coupling of the ocean and the atmosphere and momentum fluxes between them.

Thermodynamic processes active during sea ice formation have a strong influence on water mass formation and circulation in the global oceans. During the freezing process of sea water only a small portion of the sea salt is incorporated into the ice. Most of the salt is drained out and thus forms a more dense and colder water mass. This destabilizes the water column and triggers convection which can reach down to the sea floor. This process contributes to the global thermohaline circulation that ventilates the deep basins of the world ocean (Gordon, 1986). Only at a very few locations, e.g. in the Weddell Sea (Carmack and Foster, 1975) and the Greenland Sea (Ronski, 2002), does this ventilation reach the bottom. During the ventilation dissolved oxygen and other substances are transported downwards.

Most sea ice in the Arctic Ocean is formed on the Eurasian shelf (e.g. Laptev Sea and Kara Sea). The dense water production by freezing sea water is important and contributes to convection and deep water formation of the Arctic Ocean, although large river outflow into this region freshens the sea water. In contrast to the destabilizing effect while freezing, melting sea ice is a source of fresh water and therefore has a stabilizing influence on the water column. This prevents deep convection. Sea ice is usually transported for several years and over distances of some 1000 km within the Arctic Ocean, so that sea ice drift is of major importance for the fresh water and heat budgets of the Arctic Ocean.

1.2   History and Motivation

For many centuries explorers and adventurers have searched for a shortcut to East Asia and its goods and markets through the north. Many failed attempts were made to find such a way along the Eurasian coast, referred to as the North-East-Passage. Nevertheless, each one contributed to the knowledge of the northern coast of the landmasses now known as Siberia. One of those unsuccessful seafarers was the Dutch navigator Willem Barents (ca. 1550 - 1598) who died on his last endeavour after his ships were wrecked at the northern tip of the island Novaya Zemlya. Before this mishap, he was able to prepare one of the first charts of the Arctic with much detail as shown in Figure 1.3. Since he was not able to pass the Kara Gate south of Novaya Zemlya he followed the coast northward but was trapped in the ice after managing to sail around the northern end of the island. The first expedition that really completed the North-East-Passage was a Swedish-Russian expedition lead by the Swedish geologist Nils Adolf Erik Baron Nordenskjöld (1832 - 1901) on the sailing boat *Vega* in 1878-79. Nordenskjöld was lucky to sail in a year that shows an anomalously warm peak in Northern Hemisphere temperature observations (see Folland et al., 2001), which may indicate advantageous sea ice conditions along the Siberian coast.

Nowadays, shipyards are able to build stronger hulls (out of steel instead of wood as in earlier centuries) that can better resist the forces of the ice, and ships are propelled by powerful aggregates. However, sea ice can still represent a firm barrier where ships can get stuck and even damaged. A sea ice forecast for several days will enable ships to plan their routes better and react well in advance on changing conditions. This work presents a numerical model developed as a forecasting tool to predict the behaviour of the Arctic sea ice cover for several days.

Figure 1.4 shows an occasion when RV Polarstern got stuck in thick ice north of Franz-Josef-Land in September 2001. After some ramming cycles during which the ship backed up for repeated attempts to break the ice further progress was made. Such an attempt is shown in the image. The shape of the ship's hull is clearly stamped into the sea ice floe. The British polar geographer Terence Armstrong (1920 - 1996) summarized the technique of sailing in ice covered seas as follows:

> "Curiously enough, the basic method of icebreaking is still what it's been for a good many decades: brute force. You simply drive a ship, which is a kind of projectile, at the ice and hope that the ice breaks first. Generally it does." (Armstrong, 1985)

To be a bit less dependent on the power of a ship's propulsion, a modelled forecast can be helpful for saving travelling time, as well as reducing the impact on
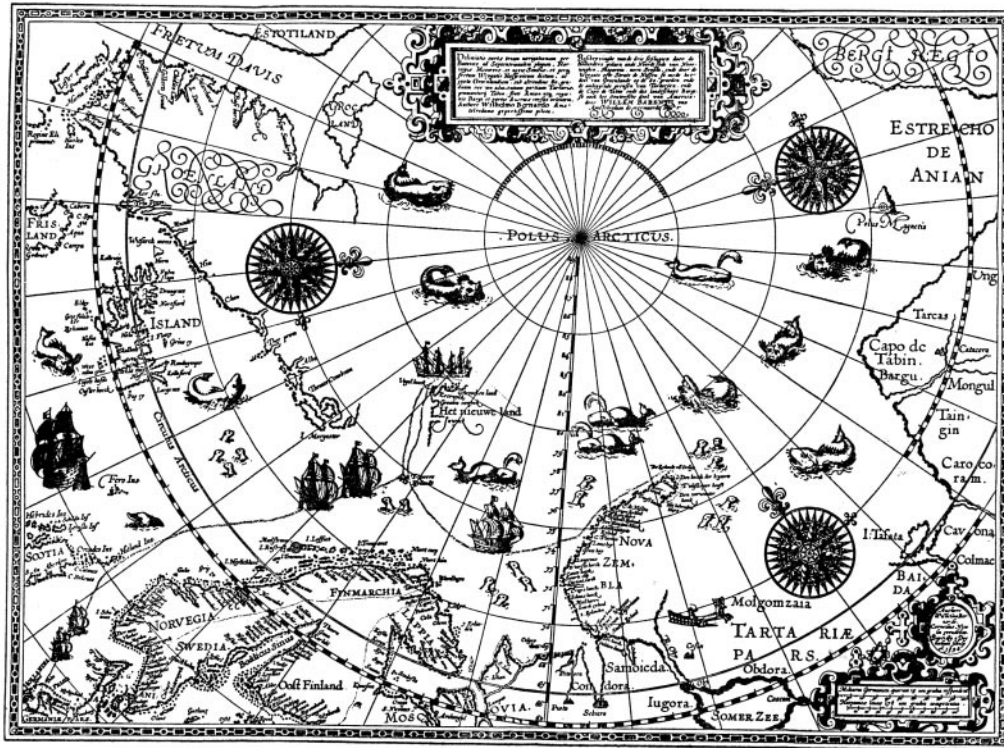
Figure 1.3: Chart of the Arctic by the Dutchman Willem Barents from 1598. This map was kindly provided by E. Seibold (2003).

Figure 1.4: RV POLARSTERN got stuck north of Franz-Josef-Land in September 2001. The ship is backing up for ramming. The ship's hull imprint is clearly visible in the sea ice.

the ship's hull, lowering environmental pollution (as a worst case scenario if a ship is damaged by the ice), and finally saving money.

Recent improvements in dynamic-thermodynamic sea ice modelling can be found e.g. in the Sea Ice Model Intercomparison Project (SIMIP) (Lemke et al., 1997; Kreyscher et al., 2000). SIMIP compared the performance of four different rheology schemes in numerical models to observational data. The model applying a viscous-plastic rheology (see Section 2.1.4) produced the overall most realistic simulations, and this version of the sea ice model provided the basis for the work presented here. As a further development of the model this study uses assimilation of satellite remote sensing data to improve the numerical description of the sea ice state to give a best estimate for predictions. If it is possible to predict the sea ice state at least for some days, it should be useful for ship routing guidance and assistance and therefore help to prevent ships getting stuck in convergent ice drift, for example.

1.3   Possible Applications

For several years, ice information has been available for the purposes of commercial navigation, public security and Navy use. For the Arctic Ocean ice maps are produced by national organizations in the USA, Canada, Russia, Norway, and Denmark on an operational basis.

There have also been attempts to predict sea ice conditions in the northern hemisphere. For example, the Navy Operational Global Atmospheric Prediction System (NOGAPS) offers a 120 hour forecast of sea ice concentration, drift, and thickness (Preller, 1994). Because of the special interest of the U.S. Navy these prediction systems focus on the western Arctic. The area of the Eurasian shelf seas receives little attention. Therefore, no statements on the condition of the fast ice areas and the trafficability of the straits along the North-East-Passage or Northern Sea Route (NSR) are produced.

The NSR is geographically the shortest route between harbours in northern Europe and East Asia. The track follows the Russian Federation coastline through the Barents Sea, Kara Sea, Laptev Sea, East Siberian Sea, and the Chuckchi Sea through the Bering Strait into the Bering Sea (see Figure 1.5). There are physical boundaries between the different parts of the NSR. The island Novaya Zemlya separates the Barents Sea and the Kara Sea. Further to the East the Kara and Laptev Seas are separated by the Severnaya Zemlya islands, and the Laptev and East Siberian Seas are separated by the New Siberian Islands. Finally, the East Siberian Sea and the Chukchi Sea are separated by Wrangel Island. Compared to the traditional track through the Suez Canal the NSR is just over half the distance. For example, the distance between the har-

Figure 1.5: The Northern Sea Route connects northern Europe with South East Asia via the Arctic Ocean. This Figure shows an example of a track from the North Sea to Japan (approx. 6900 nautical miles). The solid line indicates a possible track in favourable ice conditions if the route along the Siberian Coast (dotted alternative) is impassable due to closed key locations (e.g. , Kara Gate or Vilkitsky Strait). The dash-dotted line shows the conventional track through the Mediterranean, the Gulf of Suez, and the Indian Ocean (approx. 11100 nautical miles).

bour of Hamburg (Germany) and Yokohama (Japan) is 6920 nm via the NSR and 11073 nm through the Suez Canal. The route through the Arctic Ocean is only about 60% of the distance through the Red Sea and around India. Apart from geological (water depth in some areas) or political (atomic test sites on Novaya Zemlya) difficulties, not many ships are able to follow the NSR because of the ice conditions throughout the year. Most of the seas are ice covered and even in the summer months some straits may not be trafficable. Nevertheless, the Arctic Demonstration and Exploratory Voyage (ARCDEV) showed not only the importance of going along the NSR from Europe to Asia (or vice versa), but also the accessibility of locations along the coastline of the Russian Federation, even under winter conditions (Mikhailichenko et al., 1999).

1.4 Outline

The physical laws to describe the evolution of sea ice with a numerical model are described in Chapter 2. This also includes the improvements to the old model and a description of the newly installed atmospheric and oceanic boundary conditions. Chapter 3 briefly introduces the satellite remote sensing data used in this study. Results from model runs with the improved set-up are shown in Chapter 4 and validated using remote sensing observations. Methods to derive the best estimate of an initial state of the sea ice cover by assimilation of remotely sensed data into the model are illustrated in Chapter 5 which is followed by two examples of assimilated model runs in Chapter 6. Conclusions and outlook (Chapter 7) summarize the work carried out and suggest topics for further investigations.

Chapter 2

The Sea Ice Model

The description of sea ice with a numerical model considers both thermodynamic and dynamic processes. A complete dynamic-thermodynamic numerical sea ice model consists of four important components:

1. A momentum balance regarding the rheological properties of sea ice and prescribing the drift velocity.

2. An energy balance at the surface comprising the radiation balance, the sensible and latent heat flux and the heat conduction through the ice.

3. A model description for heat transfer through the ice and snow for a given surface temperature and oceanic heat flux.

4. A mass balance for ice and snow and a balance equation for the fractional coverage of ice (ice covered fraction for a given area) to calculate a new ice and snow thickness and ice concentration under consideration of the drift velocity (item 1.) and the freezing and melting rates (items 2. and 3.).

The sea ice model used in this work is a further development and combination of different versions of the fundamental work of Hibler III. (1979) and Parkinson and Washington (1979) for the formulations of the dynamic and thermodynamic processes, respectively. This new realization is based on the work done by Harder (1996) improving the dynamics of the numerical model and introducing sea ice roughness and age as prognostic variables. Kreyscher (1998) tested different rheology schemes with respect to the sea ice dynamics and found that the viscous-plastic parameterization including shear strain gives the most realistic estimates of sea ice conditions. A new description for sea ice roughness and pressure ridges was included by Steiner (1998) leading to a statistical prediction of pressure ridge distribution. Hilmer (2001) studied the modelled long-term sea ice variability and found that, in addition to good reproduction of the mean quantities, the model is also able to describe observed

features of inter-annual fluctuations of the Arctic sea ice cover. This includes the response of e.g. sea ice thickness to atmospheric variations such as the Arctic Oscillation (AO) or North Atlantic Oscillation (NAO). For a further description of the mechanisms and variability of the NAO refer to Brauch (2003).

Forcing data prescribing the upper and lower boundary conditions for the momentum, energy, and mass balances are needed to run the model. The following sections describe the basics of the physical and numerical specifications of the model and the improvements made.

2.1 Dynamics and Thermodynamics

The evaporation of water at lower latitudes and the freezing of sea water at higher latitudes are important distillation processes and thus driving forces of the ocean-wide thermohaline circulation. The melting of sea ice is, along with precipitation, a source of fresh water for the ocean (Aagaard and Woodgate, 2001). But since sea ice usually melts at different places than it was formed, the correct description of the physics of sea ice (dynamics and thermodynamics) is important for the description of water masses and therefore for the driving forces of the ocean circulation.

However, the most prominent role of sea ice in the climate system is the modification of heat exchange between the ocean and the atmosphere in polar regions. The heat transfer can be two orders of magnitude bigger for open water situations than in the presence of ice cover. Thus, the total area covered with sea ice as well as the regional distribution of the sea ice cover and open water are the most important quantities in terms of the climate system. If the ice cover is closed, the second important quantity is the thickness of the sea ice. A compact ice cover controls the heat transfer through the ice: the thicker the ice, the less heat can be transferred, and vice versa.

2.1.1 Continuum Approximation

On smaller scales, such as those that can be experienced by sailing a ship through the ice, the sea ice consists of ice floes varying in size from meters to kilometers, behaving like separate interacting bodies. In fact, ice floes vary not only in length and width but are also of inhomogeneous thickness and composition. On very small scales of μm to cm every single floe consists of at least two phases of water (solid and liquid) and may contain other chemical substances as well as biological organisms. Large scale numerical models calculate the mean effect of atmospheric and oceanic processes on a large number of ice floes in a certain region, which are considered as a continuous medium. Usu-

ally, those processes and phenomena occur on greater scales than the ice floes. The exact position or size of a single floe is of less importance for climatological studies than the fraction of the ocean covered with ice. Therefore, the so called sea ice concentration A (the fractional ice cover) is defined as a horizontal mean

$$A = \frac{1}{F_R} \iint_R I(x, y) \, dxdy \qquad (2.1)$$

of the ice covered area in region R of area

$$F_R = \iint_R 1 \, dxdy, \qquad (2.2)$$

where the ice indicator $I(x, y)$ is defined as 1 for ice present in grid cells and 0 for ice-free grid cells, creating a kind of ice mask.

By assuming the sea ice to be a two-dimensional continuum the quantities of the large scale means (e.g. ice concentration) should be continuously differentiable functions in space and time. The basis of this hypothesis is that an averaged quantity like the ice concentration represents a large number of small ice floes with a much smaller spatial dimension than the region considered. (An infinite number of objects of infinitely small size contribute to the mean in an idealized continuum approximation.) Although the grid resolution was significantly improved in this present realization (see Section 2.2), the model is still a large scale model, where the continuum hypothesis is still a reasonable approximation. The area of about 27×27 km represented by one grid cell is still big enough to represent a certain number of significantly smaller ice floes, but the number of grid cells required for calculating the whole model domain is still small enough to be practical for modern computers.

2.1.2   Model Variables

Analogously to sea ice concentration, other variables like ice volume and drift speed are defined as horizontal means for the region represented by the grid cell. The most important physical variables are briefly described below:

- Ice volume, h

  The ice volume per grid cell has the dimension of length, i.e. it describes the mean ice thickness of the horizontal region represented by the grid cell. In other words: the number h is the theoretical thickness of the ice if it were homogeneously distributed throughout the grid cell.

- Snow volume, h_s

  The snow volume per grid cell is defined similarly to the ice volume. It represents the mean vertical snow thickness for the whole grid cell.

- Ice concentration, A

  The areal fraction covered with sea ice - the sea ice concentration - gives the ice covered portion of a grid cell. It is a non dimensional number between 0 and 1 (i.e. 0% and 100%). Since the ice and snow volumes, h and h_s respectively, are calculated for the complete grid cell, the expected value for the ice thickness and the snow thickness of a mean ice floe in the grid cell can be calculated with the help of A. The ice floe thickness is given as h/A, the snow thickness on the ice floe as h_s/A. [1]

- Drift velocity, $\vec{u}$

  The two dimensional vector $\vec{u}$ is an estimate of the mean horizontal displacement of ice per time in a grid cell.

2.1.3 Balance Equations

The sea ice cover is mainly modified by two processes: thermodynamic growth (or decay) and advection.

Thermodynamic growth describes the freezing of sea water and thus the formation of sea ice as well as the melting of sea ice (negative growth). It is the source and the sink of sea ice. Owing to the low angle of incidence of solar radiation polar regions usually show a negative radiation balance. This leads to a cooling of the atmosphere and further to a cooling of the surface. If a cold atmosphere cools the oceanic boundary layer (the uppermost tens of metres) to the freezing point and continues withdrawing energy from the surface the result is a phase transition of water and sea ice is formed. Melting of sea ice is the same thermodynamic process in reverse: a warmer atmosphere and ocean surface heats the ice layer up to freezing point from above and below. Continued warming results in the phase transition from solid to liquid, i.e. melting. The energy balance at the ocean/atmosphere interface describes the thermodynamic ice growth.

The second process that modifies the regional distribution of the ice volume is the horizontal transport, also referred to as ice drift, or advection. Advection is responsible for the typical pattern of ice growth rates (positive and negative). Ice drift velocity is calculated using a simplified momentum balance, which corresponds to a force balance in which the inertia of sea ice is neglected. The temporal evolution of the prognostic variables - mean ice volume and mean ice

---

[1]The ice density is assumed to be constant here. Therefore, the ice volume can be calculated directly and more easily by applying the mass balance, as was done in the original formulations. That is why the ice thickness is not treated as a variable itself rather than using the terms ice volume over ice concentration h/A for the thermodynamic calculations.

concentration - is described by the following balance equations:

$$S_h = \frac{\partial h}{\partial t} + \nabla \cdot (\vec{u}h) \tag{2.3}$$

$$S_A = \frac{\partial A}{\partial t} + \nabla \cdot (\vec{u}A) \tag{2.4}$$

where h denotes the ice volume, A denotes the ice concentration and S represents the thermodynamic source or sink of the prognostic variables. If these terms are zero, the prognostic variables are conservative quantities. On the right hand side the equation is a form of continuity equation. The first term is the local temporal evolution and the second term is the advection, the in- and outflow of ice by horizontal exchange between adjacent regions.

   In contrast to the numerical sea ice model by Hibler III. (1979) the balance equations (2.3) and (2.4) have no explicit diffusion. The diffusion in Hibler's model does not describe a physical process, but only takes care of numerical stability. This artificial diffusion is needed for the numerical solution of the advection equation applying the central differences scheme. This scheme has the disadvantage of producing the numerical artifact of negative ice thicknesses (Fischer, 1995). Here, a modified upstream scheme is implemented as a numerical method for calculating the advection (Smolarkiewicz, 1983). This guarantees numerical stability without the need of including diffusion explicitly in the balance equations and does not produce negative values for quantities which may physically only take positive values.

2.1.4   Dynamics

The sea ice drift velocity $\vec{u}$ in equations (2.3) and (2.4) is derived from the momentum balance, which in Cartesian co-ordinates (Hibler III., 1979) is given by

$$m\frac{D\vec{u}}{Dt} = -mf\vec{k} \times \vec{u} + \tau_a + \tau_w - mg\nabla H + \vec{F} \tag{2.5}$$

where $D/Dt = \partial/\partial t + \vec{u} \cdot \nabla$ is the total derivative in time, m is the ice mass per unit area, f is the Coriolis parameter, $\vec{k}$ is the unit vector perpendicular to the surface, $\vec{u}$ is the sea ice velocity, g is gravitational acceleration, and H is the sea surface topography. The momentum balance (2.5) comprises the Coriolis force [2] $(-mf\vec{k} \times \vec{u})$, the air stress (τ_a), the water stress (τ_w), the surface tilt $(-mg\nabla H)$, and the force due to variation of internal ice stress $(\vec{F})$. The air and water stress as well as the internal stress are the dominant terms in equation (2.5) and are of

---

[2]Coriolis force is an apparent force named after the French mathematician Gustave Gaspard Coriolis (1792-1843). Any movement in the Northern hemisphere is diverted to the right, since the Earth is a rotating and therfore represents an accelerated system. The Coriolis parameter $f = 2\Omega \sin \varphi$ is a function of the rotation frequency $\Omega = 7.29 \cdot 10^{-5} s^{-1}$ and of latitude φ.

approximately equal magnitude. The local acceleration term is generally small and is neglected here.

These stresses are determined from simple nonlinear boundary layer theories with constant turning angle (McPhee, 1979). For the atmosphere

$$\tau_a = \rho_a c_a \mid \vec{U}_a \mid [\vec{U}_a \cos \phi + \vec{k} \times \vec{U}_a \sin \phi] \tag{2.6}$$

and for the ocean

$$\tau_w = \rho_w c_w \mid \vec{U}_w - \vec{u} \mid [(\vec{U}_w - \vec{u}) \cos \theta + \vec{k} \times (\vec{U}_w - \vec{u}) \sin \theta] \tag{2.7}$$

with
ρ_a	=	air density
ρ_w	=	water density
$\vec{U}_a$	=	geostrophic wind
$\vec{U}_w$	=	geostrophic ocean current
c_a	=	atmospheric drag coefficient
c_w	=	oceanic drag coefficient
ϕ	=	air turning angle
θ	=	water turning angle

The non-dimensional air and water drag coefficients c_a and c_w are assumed to be constant in space and time. The turning angle for the geostrophic ocean current is θ = -25°. The atmospheric turning angle is set to $\phi = 0^\circ$ and the surface wind is used as wind forcing $\vec{U}_a$. Usually $\mid \vec{U}_a \mid \gg \mid \vec{u} \mid$, therefore the relative velocity between ice drift and wind speed can be represented by the wind speed alone.

Rheology

The sea ice model accounts for shear and compressive deformation, but shows no resistance against divergent ice drift. The bulk and shear viscosities as well as the ice pressure are non-linear functions of the ice volume and the ice concentration. For normal strain rates the ice behaves like a plastic material whereas it shows viscous behavior for very small strain rates. A detailed description of the rheology scheme is given in Harder (1996) and Kreyscher (1998). In this realization of the numerical model a viscous-plastic rheology is implemented and Kreyscher et al. (2000) give a comparison of this rheology with other constitutive laws used in dynamic sea ice models. The internal forces $\vec{F}$ are calculated as the divergence of a two dimensional stress tensor σ which is related to the ice velocity field by a viscous-plastic rheology after Hibler III. (1979). Table 2.1 summarizes the main dynamic parameters and values.

Table 2.1: Dynamic parameters and values

Dynamic parameter	Symbol	Value
drag coefficient, atmosphere	c_a	$2.2 \cdot 10^{-3}$
drag coefficient, ocean	c_w	$5.5 \cdot 10^{-3}$
turning angle, atmosphere	ϕ	$0°$
turning angle, ocean	θ	$-25°$

2.1.5 Fast Ice

Sea ice, which is attached to a shore and is not drifting with ocean currents or pushed by wind stress, is called land-fast or just fast ice. Usually fast ice forms in autumn along the shores and between islands of the Arctic Ocean. When the melting season starts, the sea ice and fast ice breaks up due to wind stress, ocean currents and increasing solar radiation. Additionally, the fast ice release and retreat is influenced by river runoff, once river ice is melted and rivers discharge into the ocean again (Bareiss, 2002). In this numerical model version a fast ice parameterization is implemented. If sea ice exceeds a certain thickness over a defined ocean depth it is assumed to be steadily connected to the adjacent coast line. From observations in the Russian Arctic seas the limiting water depth for this assumption in shelf areas is set to 30 m. The fast ice is released as soon as thermodynamic processes melt the ice and dynamical processes push it offshore (J. Kolatschek, 2000, pers. comm.). This simple approach does not allow a dynamical break-up of fast ice since neither river runoff nor tidally induced motions are included in the numerical model, yet (see Section 7.2).

As can be seen from Figures 2.1 and 2.2 the parameterization works well in early summer situations. The so-called Western New Siberian Polynya reaches from Kotuy estuary to the New Siberian Islands with a landfast ice area between the coastline and the southern boundary of the polynya. The image in Figure 2.1 was taken from satellite NOAA-14 of the National Oceanic and Atmospheric Administration (NOAA) in late June 1995 with the Advanced Very High Resolution Radiometer (AVHRR) channel 1 (visible spectrum), which has a horizontal resolution of approximately 1.2 km. Dark values represent low albedos (open water and snow-free land), light values indicate high albedos (snow cover, sea ice and clouds). A model simulation for the same date (Figure 2.2) produces an ice-free area very similar in shape and dimension to that seen in the AVHRR image. Even smaller features like the ice tongue between the Lena delta and the Kotuy estuary are well represented. The ice conditions around the New Siberian Islands appear to be realistic as well.

Zyryanov and Korsens (2002) approached this problem with a regional Discrete Element Model for the Kara Sea. Their geomechanical model simulates
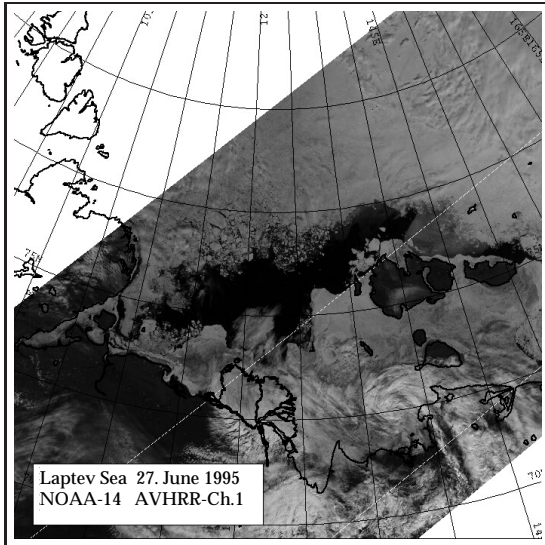
Figure 2.1: Satellite image of the Laptev Sea taken by the NOAA-14 satellite with AVHRR Channel 1 on 27 June 1995. (J. Bareiss, 2003, pers. comm.)
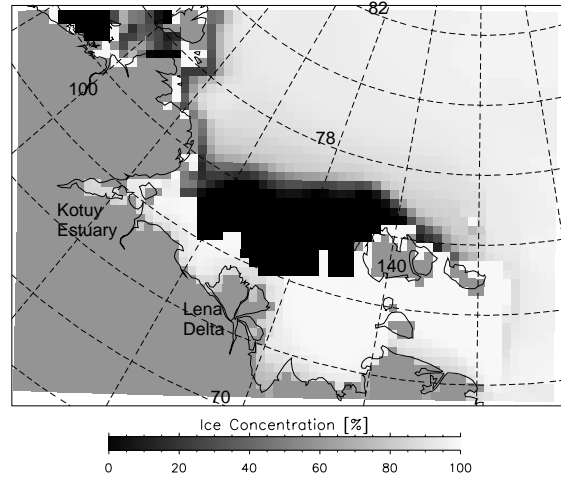
Figure 2.2: Model result of sea ice concentration for a simulation for 27 June 1995 showing the Laptev Sea region with fast ice and a polynya.

individual particles that can be bonded together and thus be treated as a continuum. However, since this is a different approach to the general physics it can not be considered for implementation in the model used in this study.

2.1.6 Thermodynamics

Both polar oceans, north and south, show a seasonally and regionally varying sea ice cover. This seasonality is most obvious in ice extent. At latitudes higher than $66°$ the incoming solar radiation shows extreme cyclic variations in sun elevation resulting in polar day and polar night. This effect is opposite in the two hemispheres, meaning that there is a phase shift of six months between north and south.

The seasonal cycle of sea ice is controlled by thermodynamic processes at the ocean-atmosphere boundary. Sea ice forms if sea water freezes at the surface of the oceans. This phase transition of water from liquid to solid is accompanied by heat release from the ocean surface to the atmosphere, after the ocean surface has already been cooled to freezing point. Melting of sea ice is the opposite phase transition caused by heat input to the ice either from above or below.

Parkinson and Washington (1979) formulated the thermodynamic evolution of sea ice using an energy balance of the uppermost stirred layer of the ocean, the so called mixed layer. The oceanic mixed layer is characterized by zero vertical gradient in temperature and salinity because of the input of turbulent kinetic

energy by the wind and in winter by convection. These forcing mechanisms mix the upper layer down to a characteristic depth, the mixed layer depth. In this model realization the properties of the mixed layer are described by a one dimensional model implementation with a fixed mixed layer depth, a simplification of Lemke (1987). The net heat flux in this mixed layer, Q_n, can be split into an atmospheric, Q_a, and an oceanic, Q_o, component. At the freezing point the energy budget is balanced by the release of latent heat and thus the formation of sea ice. In the presence of a sea ice cover the energy balance follows as

$$Q_a + Q_o + \rho_i L_i S_h = 0 \tag{2.8}$$

with ρ_i and L_i are the density and the specific heat of fusion for sea ice, respectively, and $S_h = \partial h/\partial t$ gives the change of sea ice volume in a grid cell. A change of 1cm in ice thickness per day corresponds to a heat flux $Q_n \approx 35$ Wm^{-2}.

For a more detailed description of the heat flux the energy balance equation (2.8) is applied to the upper and lower surface separately (Semtner, 1976). The change at the atmosphere-sea ice interface (melting) is calculated from

$$Q_a + Q_c + \rho_i L_i (\partial h/\partial t)_a = 0 \tag{2.9}$$

and the change at the ocean-sea ice interface (melting or freezing) is determined from

$$Q_o - Q_c + \rho_i L_i (\partial h/\partial t)_o = 0 \tag{2.10}$$

where Q_c is the conductive heat flux through sea ice. In this 0-layer model assumption the ice has no heat capacity, so Q_c at the upper and at the lower side of the ice is the same, but it enters the two equations with opposite signs. The temperature at the underside of the ice, T_b, is constant and equal to the freezing point of sea water $T_{f,o}$ = -1.86 °C (for salinity of 34) if sea ice is present. Basal freezing occurs if $(Q_o - Q_c) < 0$ and basal melting occurs if $(Q_o - Q_c) > 0$, according to equation (2.10). The surface temperature T_s of sea ice at the atmospheric boundary is a diagnostic variable determined from the surface energy balance and is limited by the fact that it can not exceed the freezing temperature $T_{f,a}$ of sea ice at the surface, which is set to the freezing temperature of fresh water ($T_{f,a} = T_0 \equiv 0$ °C) because the surface of sea ice is usually characterized by very low salinity.

The total thermodynamic change in ice volume

$$S_h = (\partial h/\partial t)_a + (\partial h/\partial t)_o \tag{2.11}$$

is called the thermodynamic growth rate with a positive sign for freezing and a negative sign for melting. To distinguish between the two processes the freezing rate is defined as $G_h = \max(S_h, 0)$ and the melting rate is defined as $M_h = \min(S_h, 0)$, where $G_h \geq 0 \geq M_h$.

Atmospheric Heat Flux Q_a

The atmospheric energy flux at the surface (over ice or open water) is

$$Q_a = Q_s + Q_l + R_{s,\downarrow} + R_{s,\uparrow} + R_{l,\downarrow} + R_{l,\uparrow} \tag{2.12}$$

with
Q_s = turbulent flux of sensible heat
Q_l = turbulent flux of latent heat
$R_{s,\downarrow}$ = incoming short-wave radiation flux
$R_{s,\uparrow}$ = outgoing short-wave radiation flux
$R_{l,\downarrow}$ = incoming long-wave radiation flux
$R_{l,\uparrow}$ = outgoing long-wave radiation flux.

The incoming short wave and long wave radiation ($R_{s,\downarrow}$ and $R_{l,\downarrow}$) is determined by external forcing. The turbulent heat fluxes of sensible and latent heat (Q_s and Q_l) are described with bulk formulae, which are also taken from external forcing, following Smith (1988)

$$Q_s = c_s c_p \rho_a \mid \vec{u}_a \mid (T_a - T_s) \tag{2.13}$$
$$Q_l = c_l L \rho_a \mid \vec{u}_a \mid (q_a - q_s) \tag{2.14}$$

where the exchange coefficients for sensible and latent heat are c_s and c_l, respectively, c_p is the specific heat capacity, ρ_a the density of air, T_a the air temperature at 2 m height, and the surface temperature of the ice is T_s. In the formula for the latent heat flux q_a is the specific humidity of air at 2 m height and q_s is the specific humidity of air directly at the ice surface, which is assumed to be saturated. The specific latent heat of fusion L is set to the value of evaporation over open water and sublimation in ice covered areas.

A major part of the incoming short wave solar radiation is reflected by ice and snow

$$R_{s,\uparrow} = -\alpha R_{s,\downarrow}. \tag{2.15}$$

The fraction of radiation reflected from the surface compared to that incoming is called the albedo α of the surface. Different surfaces have a different reflectivity and thus a different albedo. Open water areas absorb most of the short-wave radiation and have a very low albedo (α = 0.1). Owing to the low albedo, even quite small areas of open water have a significant influence on the energy balance of the mixed layer. Fresh snow cover has a very high albedo at about 0.8. Figure 2.3 gives the values for different surface types as used in the numerical model and shows examples of how these types look in the Arctic.

The emitted long wave radiation $R_{l,\uparrow}$ in the infrared spectrum is calculated using the Stefan-Boltzmann-law

$$R_{l,\uparrow} = -\epsilon_s \sigma_B T_s^4 \tag{2.16}$$
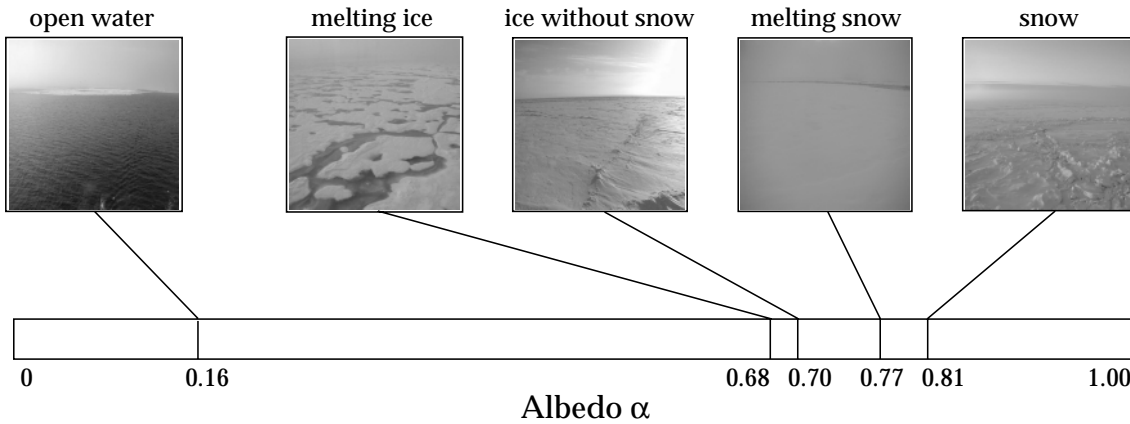
Figure 2.3: Values for different surface types in the Arctic Ocean as used in the numerical model. The sample images are taken from Haas and Lieser (2003).

for a grey body with a surface emissivity ϵ_s (here set to $\epsilon_s = 0.99$) and the Stefan-Boltzmann-constant $\sigma_B = 5.67 \times 10^{-8}$ W/m^{2}K^4.

Oceanic Heat Flux Q_o

The oceanic contribution to the energy balance - the oceanic heat flux Q_o - is calculated by a simple, prognostic, one dimensional mixed layer formulation with a constant mixed layer depth d. It accounts only for vertical heat fluxes and disregards horizontal heat exchange between grid cells. Input to this model are wind shear stress (or ice motion) and fresh water and heat flux from the sea ice model. The mixed layer model returns the oceanic heat flux Q_o to the sea ice model.

At the ice underside, where the mixed layer temperature is at freezing point $T_d = T_f$, the oceanic heat flux is equal to the heat flux from the deep ocean into the mixed layer ($Q_o = Q_t$). In summer in ice-free areas the mixed layer temperature T_d can increase and the mixed layer acts like a heat reservoir. This heat must be released to the atmosphere in autumn and winter before an ice cover can develop.

Ice Thickness Distribution and Open Water

In reality, sea ice is not a uniformly closed cover but consists of single floes of different size and thickness with areas of open water in between (see Figure 2.4). The heat flux over open water (described with an ice volume $h = 0$) can be two orders of magnitude higher than the local heat flux through a thick ice cover. Areas of open water are exposed directly to the atmosphere, whereas a closed ice cover acts as a good thermal insulator. An inhomogeneous ice cover with inhomogeneous ice thickness distribution will modify the heat exchange between

Figure 2.4: Photograph of typical Arctic sea ice conditions at the beginning of the winter season. This picture was taken on 13 September 2001 in the evening.
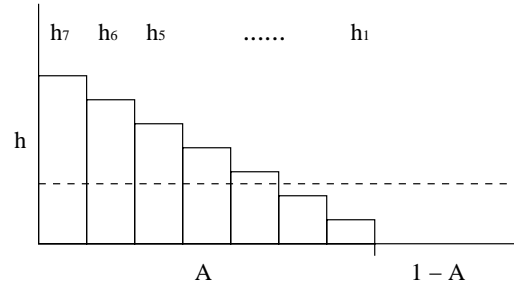

Figure 2.5: Ice volume distribution in seven ice classes for the calculation of the mean heat flux. The distribution is assumed to be uniform in the interval between 0 and $2h/A$. The mean ice thickness (dashed line), calculated as h/A, is the reference for the relative ice thicknesses for all classes.

the ocean and the atmosphere. Thinner parts of the cover will allow for a greater exchange of heat/energy than thicker ones. In this model the idealized grid cell contains seven ice classes with an evenly distributed ice thickness distribution ($1/7 \; h/A \leq D_k \leq 13/7 \; h/A$, see Figure 2.5). The thermodynamic energy balance is solved for every ice class separately and the corresponding net heat fluxes $Q(D_k)$ are added. To determine the heat flux over open water the energy balance (2.8) is solved directly.

Snow Cover and Conversion of Snow

If sea ice is present precipitation can accumulate so that ice floes are covered with a snow layer. This layer can be persistent throughout a summer season as in most regions in Antarctica, but it is usually transformed into liquid phase in the Arctic during the summer months. Two main processes are responsible for this snow conversion, one predominant for each polar region. Temporarily, in Antarctica ice floes can have a negative free-board (the height of an ice floe that is above sea level is called free-board) due to a heavy snow load. It pushes the ice-snow interface below sea level and sea water can flood the loosely packed snow cover. This happens if about one third of the total thickness (snow and sea ice) is snow load. The process is called flooding and with further freezing this water is converted into a thin, more saline ice layer on top of the sea ice, below the snow cover. The other process is percolation of meltwater downwards through the snow, forming a new thin ice layer composed of fresh water on top of the sea ice, so-called superimposed ice. Both transformations happen in both polar regions but flooding occurs more often in the south polar seas, where sea

Table 2.2: Thermodynamic parameters and values

Thermodynamic parameter	Symbol	Value
exchange coefficient for sensible heat	c_s	$1.75 \cdot 10^{-3}$
exchange coefficient for latent heat	c_l	$1.75 \cdot 10^{-3}$
the specific heat capacity of air	c_p	1004 J/kg K
the specific heat capacity of sea water	c_w	4010 J/kg K
surface emissivity	ϵ_s	0.99
lead closing parameter	h_0	0.75
heat conductivity of snow	k_s	0.31 W/m K
heat conductivity of sea ice	k_i	2.1656 W/m K
specific latent heat of sea ice	L_i	$3.34 \cdot 10^5$ J/kg
specific latent heat of evaporation	L	$2.50 \cdot 10^6$ J/kg
specific latent heat of sublimation	L	$2.83 \cdot 10^6$ J/kg
mean air pressure	p	1013 hPa
density of sea ice	ρ_i	910 kg/m^3
density of snow	ρ_s	300 kg/m^3
density of sea water	ρ_w	1026 kg/m^3
density of air	ρ_a	1.3 kg/m^3
Stefan-Boltzmann constant	σ_B	$5.67 \cdot 10^{-8}$ W/m^{2}K^4
freezing temperature of fresh water	$T_{f,a}$	$0\,^\circ$ C
freezing temperature of sea water	T_f	$-1.86\,^\circ$ C
mixed layer depth	d	25.4 m

ice is usually thinner and the snow load can push the free-board below sea level. In the Arctic Ocean sea ice in general is thicker (compared to the Antarctic) and the free-board is not pushed below sea level by snow. The snow layer on Arctic sea ice disappears almost completely during the summer months, whereas a snow cover may accumulate over several seasons in Antarctica. In the numerical model the snow conversion by flooding is implemented[3] in a way that the snow cover, which is below sea level, is converted to ice. This method follows the Archimedes principle and is described in more detail by Fischer (1995). The formation of superimposed ice is not simulated by the model, but is a task for further development. Observations in both the Antarctic by Haas et al. (2001) and in the Arctic by Nicolaus et al. (2003) showed that during the melting season the superimposed ice survives longer on the sea surface because it consists only of fresh-water ice, thus is less porous than sea ice and melts only at higher

---

[3]Although the flooding process is more dominant for the Antarctic environment it should be considered in the Arctic as well if the model starts with no ice cover. During spin up years this prevents from computing unrealistic snow thicknesses.

temperatures. This lengthens the ice-covered period for the area where super-imposed ice has formed.

The heat conductivity of snow k_s is seven times less than the heat conductivity of ice k_i. So even a thin snow cover acts as a good thermal insulator and reduces the thermodynamic growth rate of sea ice significantly. A second effect of fresh snow cover is the high albedo. This increases the reflection of solar energy which, in turn is no longer available for melt processes. To account for these effects, the numerical model includes a prognostic snow layer after Owens and Lemke (1990). The evolution of this snow layer is calculated in a way similar to the balance equations (2.3) and (2.4) as

$$S_s = \frac{\partial h_s}{\partial t} + \nabla \cdot (\vec{u} h_s). \tag{2.17}$$

It is advected with the same drift velocity $\vec{u}$ as sea ice. The source of snow is a specified precipitation rate P_w which is defined as snowfall at air temperatures $T_a < 0\,^\circ$ C. Only the amount of snow over the ice-covered fraction of a grid cell contributes to the snow layer. During the melting season the snow cover is reduced by thermodynamic processes. In the model the snow cover has to melt completely before the sea ice starts to melt from the top. Bottom melting is calculated independently and usually starts before top melting. The thermodynamic parameters and constants used in the numerical model and their values are summarized in Table 2.2.

2.2 Grid and Setup

The model describes the evolution of the characteristic variables of sea ice with continuously differentiable functions. To solve the functions numerically the equations are discretized in space and time. The physical quantities of the model are defined at a limited number of grid points. The prognostic evolution is calculated by integrating the corresponding differential equations with a finite time step Δt. Derivatives are approximated by finite differences (e.g. $\partial h/\partial t \approx \Delta h/\Delta t$). The grid used in this study is a so called Arakawa-B-grid. The grid points for the vector state variables (e.g. ice velocity) are shifted horizontally by half a grid spacing against the grid for the scalar state variables (e.g. ice volume). For a detailed description of the applied methods see Mesinger and Arakawa (1976).

The model reproduces the annual cycle and the variability of the sea ice conditions with a daily time step well (e.g. Hilmer, 2001). The version implemented here operates with a time step of six hours (Δt = 21600 s). This allows the local influence of atmospheric pressure systems to be taken into account. By reducing the time step from daily to six hours the grid resolution was increased from
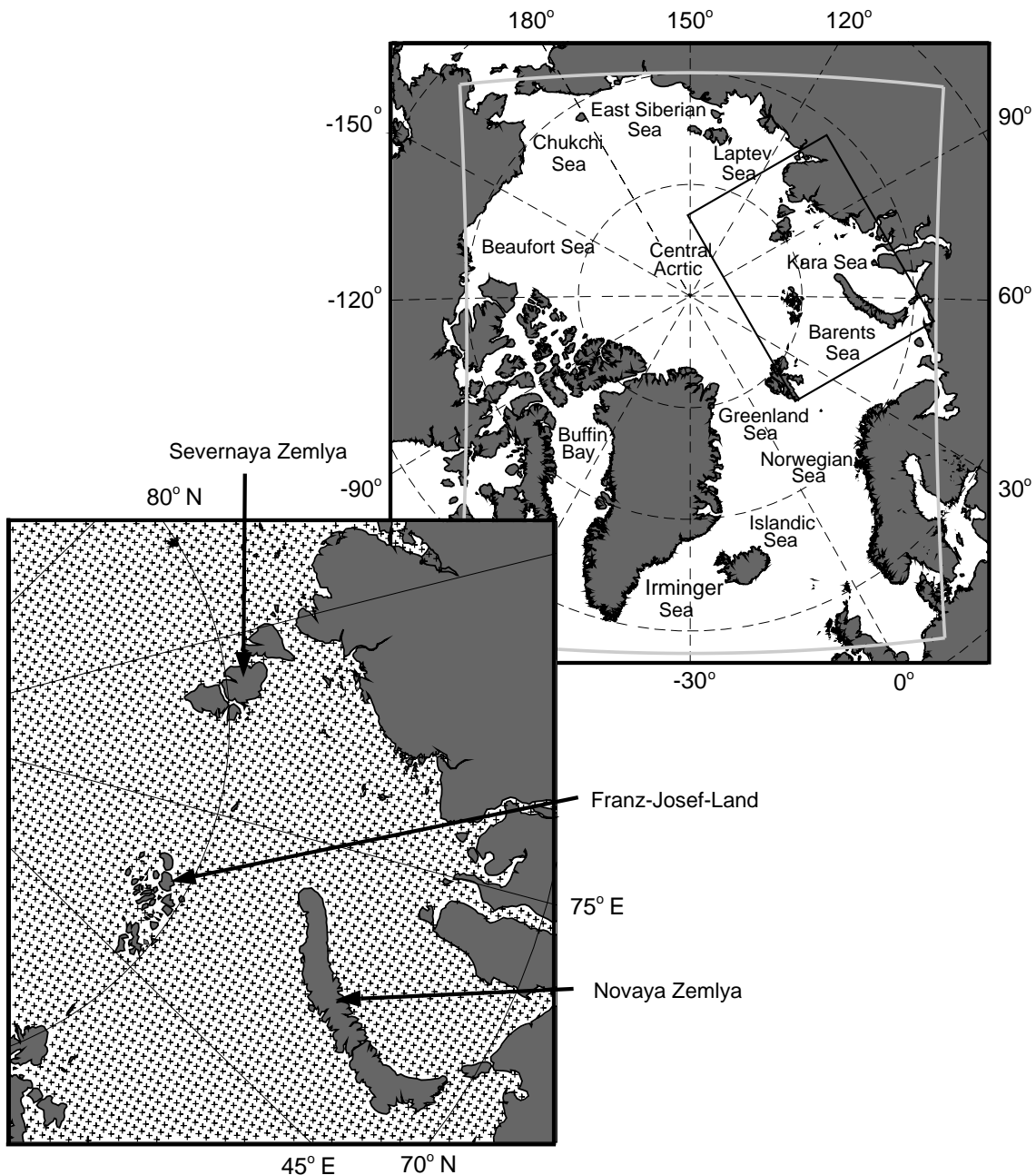
Figure 2.6: The model domain covers the complete Arctic Ocean, the Nordic Seas, and the northern North Atlantic and is indicated by the grey rectangle in the upper right part. The black rectangle indicates the location of the lower left panel, which gives an impression of the density of grid points in this recent model setup as an example for the Barents and Kara Seas.

$1°$ (~ 110 km) to $1/4°$ (~ 27 km). An illustration of the grid point density is given in Figure 2.6 for the Kara Sea region. Some of the passages that are critical to ship routing, e.g. the Kara Gate at the southern tip of the island Novaya Zemlya connecting the Barents Sea and the Kara Sea, or the Vilkitsky Strait between the southern island of Severnaya Zemlya and the northern tip of the Taymyr Peninsula connecting the Kara Sea and the Laptev Sea are resolved with several grid

points, so that statements can be made regarding the possible trafficability of these regions. Also, the archipelago of Franz-Josef-Land, which was missing in the model with the coarser resolution, was added to the model grid according to the bathymetry of the International Bathymetric Chart of the Arctic Ocean (IBCAO) (Jakobsson et al., 2001).

The grid used in the model is based on a spherical coordinate system similar to the geographical coordinate system. To avoid the singularity of the North Pole the grid is rotated and shifted in such a way that the North Pole of the spherical model grid is located in the Indian Ocean at $0°$ N and $60°$ E. The model equator is located at $30°$ W (positive x-direction) and $150°$ E (negative x-direction) and runs through the geographical North Pole, where it crosses the $0°$ model-Meridian. This leads to approximately equal grid spacing throughout the model domain. To allow natural outflow regimes from the model domain, the boundary grid cells in the Atlantic region and in the Bering Strait are defined as outflow cells.

Four-Colour Relaxation

The relaxation routine of the numerical model solves the linearized momentum equation. It is by far the most dominant routine consuming most of the computing time (almost 90%). Using a multi-colour relaxation scheme with p colours each iteration consists of p sweeps. For the first sweep, all points with coordinates $i = 1 + jp$ (where j is a non-negative integer) are relaxed. In the second sweep, all points with coordinates $i = 2 + jp$ are relaxed, where the new values at previously relaxed points are already used. This procedure continues until all points are updated. Introducing more colours to a multi-colour relaxation scheme improves the efficiency of the system. In this study $p = 4$ because, according to Llorente et al. (2000), it appeared as a good trade-off between convergence and parallel properties.

With the former red-black relaxation some components were calculated several times for one relaxation step. A four-colour relaxation has been installed instead of a red-black relaxation for the partial differential equations with cross-derivative terms. The operators used in the momentum equation have an influence beyond their nearest neighbour. In the two colour scheme, this leads to a simultaneous usage of grid points with old values and new values from the recent relaxation step. The four-colour relaxation overcomes this problem and the four point sets are decoupled completely. This provides better convergence rates and fewer relaxation steps are needed to meet the accuracy required. An illustration of the patterns is given in Figure 2.7. Detailed information on group relaxation (including the four-colour relaxation) can be found in Faddejew and Faddejewa (1973).
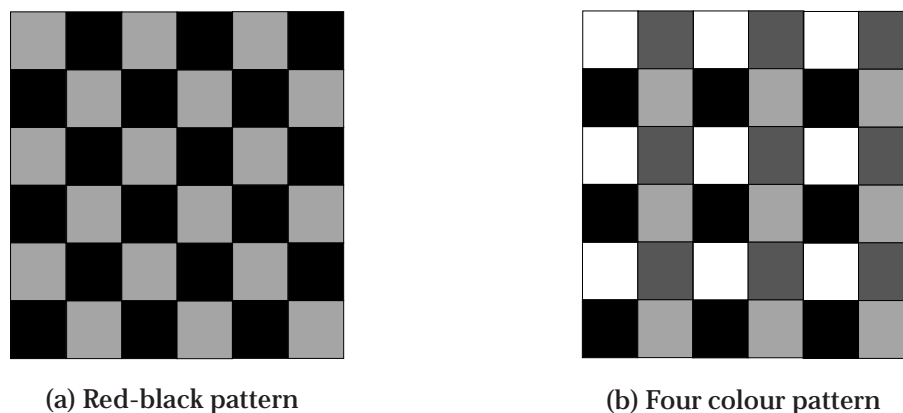
| (a) Red-black pattern | (b) Four colour pattern |

Figure 2.7: Illustration of the relaxation scheme. The two colour relaxation is commonly known as red-black relaxation, the four colour pattern shows that the four point sets are decoupled.

2.3 Forcing

The evolution of sea ice is dependent on the state of the atmosphere and the ocean as upper and lower boundary conditions. These conditions are explicitly prescribed as external forcing for the numerical model.

2.3.1 Atmospheric Forcing

The atmospheric conditions vary on short time scales. Pressure systems develop and move over periods of a few days. Some of the atmospheric forcing parameters are given on a 6-hourly basis and some are given as climatological monthly means. Both groups are described briefly below.

Sub-daily Forcing

The atmospheric forcing used in previous studies was derived from National Centers for Environmental Prediction (NCEP) re-analyses. In this study 2 m air temperature and the 10 m wind velocity and wind direction are prescribed every six hours from analysis data of the European Centre for Medium-Range Weather Forecasts (ECMWF) global model. These data are treated as surface conditions. Although both data sets (NCEP and ECMWF) have their advantages and deficiencies, the ECMWF data are more realistic in prescribing the surface fluxes (e.g. precipitation and evaporation and radiative fluxes associated with cloudiness) at high latitudes (Walsh et al., 1998). Therefore, the atmospheric forcing from ECMWF was chosen here.

The ECMWF data are given on a geographical grid with a resolution of $1.125°$. These data have to be interpolated onto the model grid. Because both

grids are fixed, the interpolation coefficients can be calculated once externally
and the indices and the weights of every grid point are read into the model only
once. The interpolation uses a bilinear technique to avoid discontinuities that
could be introduced by other methods such as the inverse distance weighted
method. The bilinear function is continuous, and although it is not differen-
tiable along grid edges, this is not necessary for use in the numerical model.

(a) ECMWF 2m-temperature field

(b) interpolated model 2m-temperature
field
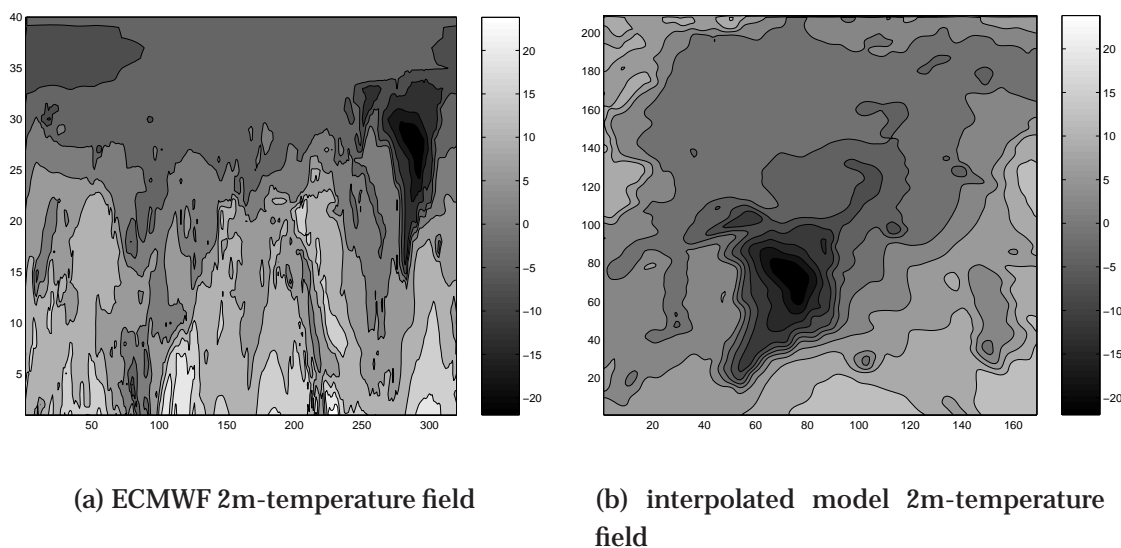
Figure 2.8: Example of an original gridded forcing field for 2 m-air temperature from
ECMWF analysis data for the Northern Hemisphere (a) and an interpolated field for
the model forcing (b). The numbers on the axis give the x- and y-coordinates for the
grids. The ECMWF data are on a 320×161 points grid, but only the northern part of the
Northern Hemisphere is displayed. The sea ice model has 169×209 grid points.

Figure 2.8 gives an example of 2 m-air temperature fields (a) as derived from
ECMWF and (b) converted for the model forcing. Greenland is clearly visible in
both fields with the lowest temperature in the region, as is the transformation
of the North Pole region from a very much stretched distribution in the original
data set to a confined range in the model input data set.

Climatological Forcing

The relative humidity U is given as a climatological monthly mean (Hilmer,
1997). The quality of humidity fields provided by forecast centers like ECMWF
or others is still unsatisfactory because of the sparse input data from weather
stations in polar regions and difficulties in measuring humidity in cold environ-
ments or estimating it from remote sensing data. However, for calculating the
latent heat fluxes the climatological means are interpolated to the applied time
step, which produces good results.

The cloud coverage $A_c \in [0, 1]$ and the precipitation rate P_w are also given as climatological monthly means. The values are linearly interpolated for each time step.

Solar irradiation (including a cloud correction) and long wave emission are parameterized with empirical formulations after Zillman (1972) (and Laevastu, 1960) and König-Langlo and Augstein (1994), respectively.

2.3.2 Oceanic Forcing

The oceanic forcing parameters are given as climatological monthly means for the heat flux from the deep ocean into the mixed layer and for the ocean surface currents. The fields are derived from a coupled sea ice-ocean model (Gerdes et al., 2001), based on a Modular Ocean Model (MOM) version from the Geophysical Fluid Dynamics Laboratory (GFDL) (Pacanowski, 1995), from a model run for years 1979 to 1992. In addition to the higher spatial resolution (corresponding to the finer sea ice model grid) the new forcing fields show better seasonal variability compared to the previous input, which consisted of a constant ocean current field and monthly mean ocean heat flux fields. The previous oceanic forcing was derived from a different sea ice-ocean model (Harder, 1996), which will be referred to as SIOM in the following.

The circulation of the uppermost ocean layer changes from a cyclonic to an anticyclonic mode every 5-7 years (Proshutinsky and Johnson, 1997). Although this inter-annual variability is not represented in the ocean current fields employed in this study, the new forcing gives a much better estimate of the seasonal ocean state than the annual mean used in previous studies. In Figure 2.9(a) the ocean surface current field used in previous studies is displayed. This field, identical for all seasons, has proven to be sufficient for the coarser grid. An example of the higher resolution of the new forcing field is shown in Figure 2.9(b) for December. It clearly shows much more detail on the current systems in the Nordic Seas and the adjacent regions leading to a better representation of sea ice drift. Together with the other oceanic forcing parameter, the oceanic heat flux Q_o, this improved ocean boundary leads to a spatial and temporal variability and thus to a more realistic description of the natural environment compared to studies with a constant ocean forcing.

The ocean heat flux fields (Figure 2.10 as example for December) show a strong variability in the Nordic Seas (namely Greenland Sea, Icelandic Sea, and Norwegian Sea) and the adjacent Barents Sea, exceeding over 400 W/m^2 in winter months and -200 W/m^2 in summer. Positive heat flux values indicate a upward flux direction (from ocean to the overlying layer - ice or atmosphere), negative values indicate a downward direction and thus a gain of energy for the
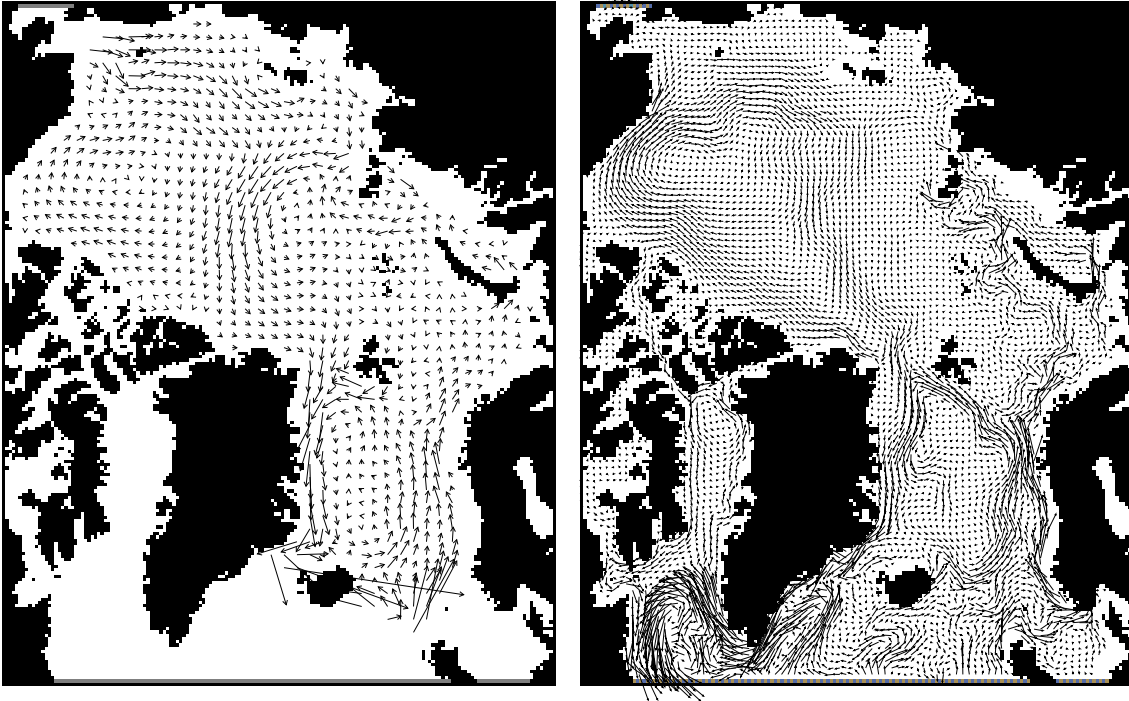
(a) Previous ocean current field for all seasons

(b) Example of the new ocean current field for December

Figure 2.9: Comparison of the ocean current fields (a) as used previously and (b) in this study. The former ocean forcing was constant in time. The newly introduced ocean current fields are deduced from MOM. They are represented by twelve climatological fields, one for each month of the year. Figure 2.9(b) displays every second arrow for December (in correspondence with the ocean heat flux shown in Figure 2.10).

ocean. The relatively low heat flux values within the Central Arctic remain constant at about 2 W/m^2 throughout the year under a persistent ice cover.

The combination of the new oceanic boundary forcing (i.e. ocean currents and ocean heat flux) improves the estimation of the sea ice cover significantly (see Chapter 4). With the old forcing, the numerical model tends to overestimate the sea ice concentration as compared to remote sensing data from SSM/I (see Section 3.2.1). But after the installation of the higher resolution ocean forcing the sea ice concentration appears to be more realistic. The most obvious improvements are visible in the marginal zones such as in the Greenland Sea and Barents Sea (i.e. north of Iceland, southwest of Svalbard and west of Novaya Zemlya).
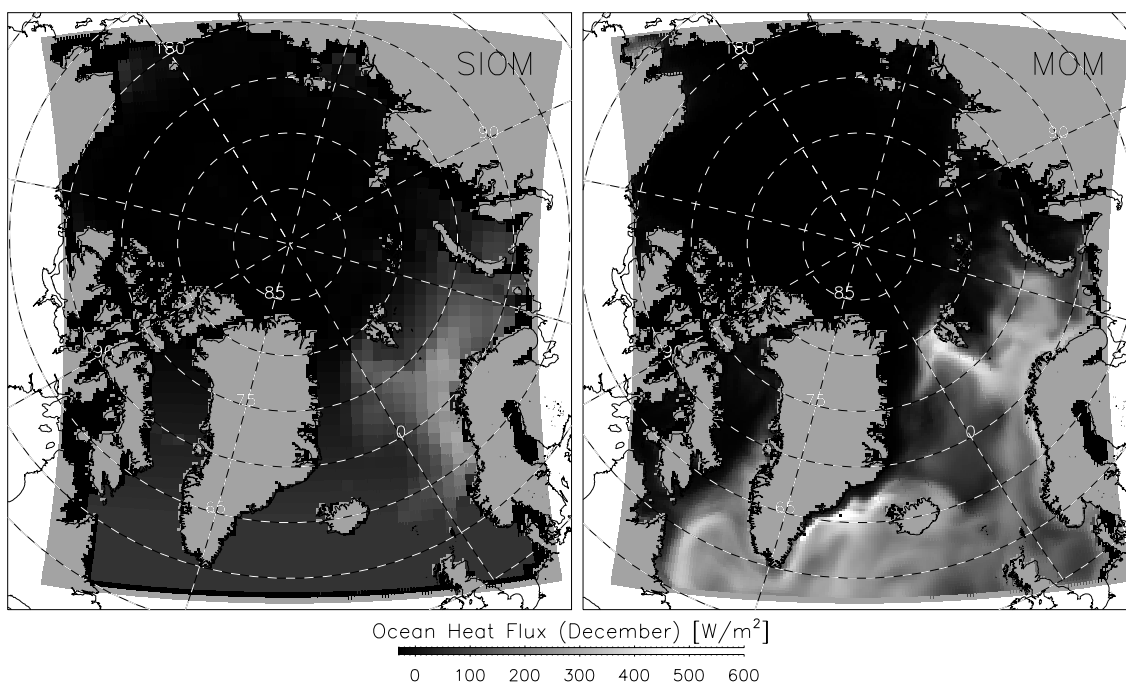
Figure 2.10: This Figure gives an example of a previous (SIOM, left) and a new (MOM, right) forcing field for the oceanic heat flux from the deep ocean into the mixed layer for December. The resolution is adopted to the new resolution of the ice model. The new fields show more variability in both regional pattern and absolute values.

2.4   Initial Conditions

The model can be run in two different modes. The first mode is a climatological run of a single year, which starts with an initially ice-free ocean. The year's run is repeated with identical forcing until an equilibrium state is reached. This period is referred to as "spin-up years". After equilibrium is reached, the constant forcing is replaced by the forcing data for each subsequent year.

The second mode is a data assimilation mode where the model integration starts with a optimized initial condition for the sea ice concentration field. Other sea ice variables are restored accordingly (see Section 6.1). Such a starting field is obtained from an un-assimilated run up to the assimilation date and afterwards the model is restored with the new condition. This mode is used if the model is run as a forecast model to yield a dependent forecast for sea ice conditions. The forecast is dependent because it relies on the atmospheric forcing fields provided by the forecast models run at weather prediction centers. The forecast of the sea ice model is, therefore, limited by the quality of the forecast of the atmospheric model. However, since the ECMWF gives a forecast score of over 60% for a regular five day forecast of the 1000 hPa geopotential (Järvinen, 1998) a dependent forecast of the sea ice model should be reliable for at least that period.

31

2.5   Summary

The dynamic-thermodynamic numerical sea ice model operated in this study is a further development of previous work as described earlier. Novel to this study is the introduction of a fast ice parameterization, which leads to a more realistic estimation of the development of polynyas and coastal flaw leads, which is necessary if the model is used for ship routing purposes. Further, a more realistic bottom topography introduces smaller islands to the model grid, for example, as barriers to the sea ice drift. In combination with the higher grid resolution key locations of the Northern Sea Route are now resolved by the model. The preparation of new forcing fields for the ocean boundary condition improves the ocean current-induced drift patterns and the thermodynamic response of the sea ice to the lower surface. Finally, new atmospheric forcing data from ECMWF are applied. For short term sea ice prediction the model can be run in forecast mode. To achieve the best possible analysis of the sea ice state as starting conditions for a forecast, assimilation of sea ice concentration fields has been introduced, and this is described in detail in Chapter 5.

Chapter 3

Remote Sensing

The Earth's surface reflects and emits electro-magnetic energy which can be detected by sensors that are not necessarily in direct contact with the observed ground. This type of observation from a remote platform (e.g. an aircraft or a spacecraft) by a measuring instrument is called remote sensing.

In the following sections some aspects of remote sensing in general and especially in polar regions are outlined and a few sensors are introduced from which information has been selected for assimilation into the numerical model and for validation purposes.

3.1 General Remarks

Satellites are positioned, both as geo-stationary (with near geo-synchronous orbit) and polar orbiting objects. Geo-stationary satellites sample the same view of the surface continuously from a height of approximately 36000 km which enables them to monitor rapidly evolving events. The sampling interval is only limited to the technical possibilities of the instruments but due to the high orbit only limited ground resolution can be achieved. Changing illumination conditions restrict visible observations to daytime. Polar regions are not observed with these satellites. At much lower altitudes (ca. 800 km) polar orbiting satellites offer global coverage and improved ground resolution. However, temporal resolution is reduced as continuous observation, as with geo-stationary satellites, is not feasible since each point of the surface is viewed only twice a day (or even less) in equatorial regions or once per orbit (at best, every 100 minutes) in polar regions, depending on the swath width of the sensor.

Solar short-wave radiation enters the atmosphere and is either reflected, scattered, or absorbed by atmospheric constituents (e.g. clouds or trace gases) or is transmitted or scattered to the surface, where it is reflected or absorbed. Both, the atmosphere and the surface emit long-wave (terrestrial) radiation

according to the Stefan-Boltzmann law (2.16). The characteristics of the reflected, scattered, and emitted radiation can be used to distinguish between different emitters and thus to infer certain features of various quantities of the atmosphere and the planetary surface on a continuous monitoring basis. Radio waves, microwaves, infrared radiation, and visible light are the most common forms of electro-magnetic radiation used in remote sensing.

Remote sensing techniques can be categorized into two generally different methods for deriving the information: active and passive methods. Active systems include a source of energy (emitter) and a detector which measures various characteristics of the return signal. Depending on the physical feature of interest it is necessary to choose the best combination of orbit (coverage and resolution) and instrument (electro-magnetic active range) for the detection of physical parameters from space. The main observable parameters are the range to the target (calculated from the time delay of the returned signal) and the characteristics of the reflected or emitted radiation of the material, which is determined by its physical properties. The resolution of a system is restricted to the so-called diffraction limit $H\lambda/D$, where H is the height (or altitude), λ is the wavelength, and D is the diameter of the lens, objective mirror, or antenna. This limit is usually of the order of metres or tens of metres for optical sensors on board low orbiting satellites and several kilometers for geo-stationary satellites. For passive microwave systems the spatial resolution is much coarser (typically tens of km) because of the larger wavelength measured.

Active methods include, for example, Radar which is used for detection and ranging in the radio band or the imaging Synthetic Aperture Radar SAR[1] in the microwave band or Lidar for the optical spectrum (including near-infrared, visible, and near-ultraviolet). Systems measuring electro-magnetic energy reflected and/or emitted from the Earth's surface without an active emitter are called passive (for example, AVHRR).

3.2 Remote Sensing of Sea Ice

Massom (1991) and Tucker et al. (1992) describe the physical properties of sea ice which are relevant for remote sensing. The main parameters are the reflectivity (albedo) or brightness temperature of sea ice and water, which can be measured directly using radiometers, and the backscatter of ice, which is mea-

---

[1]It is possible to improve resolution by using a larger antenna. Since it is impractical to place very large radar antennae in space, the spacecraft's motion and advanced signal processing techniques are used to simulate a larger antenna. This way many backscattered radar responses are obtained for one object. The synthetic aperture is therefore the distance traveled by the spacecraft while the radar antenna collected information about the object.

sured by active instruments. These properties are known from laboratory investigations as well as from many field experiments (e.g. ARCDEV, see Section 6.3). Small scale surveys have been carried out to develop instruments and calibrate algorithms for the monitoring of physical parameters like percentage coverage of sea ice or snow cover properties from space on a global scale. Such information can be used for the initialisation and validation of sea ice models and coupled GCMs and as boundary conditions for atmospheric models.

Several active and passive systems are currently in operation for the detection of physical parameters of sea ice from space. For example, the Active Microwave Instrument (AMI) on-board the polar orbiting European Remote Sensing Satellites ERS-1 and ERS-2 is run by the European Space Agency (ESA). It has a non-imaging scatterometer mode, which provides data on sea ice extent and surface roughness (e.g. Ezraty and Cavanié, 1999), and an imaging real or synthetic aperture radar. The Radar Altimeter RA-2, which is installed on ESA's ENVISAT, is another example of a non-imaging active system. Other imaging synthetic aperture radar instruments are, for instance, the Canadian RADARSAT-1 SAR and most recently RADARSAT-2 SAR. These systems are able to look through clouds and therefore provide data irrespective of weather or illumination. The spatial resolution ranges from 25 m (ERS-2) to 50 m (RADARSAT-1) within a 100 km and 450 km wide swath, respectively.

3.2.1 Microwave Imager (SSM/I)

The Special Sensor Microwave / Imager (SSM/I) is installed on-board the polar orbiting satellites of the Defense Meteorological Satellite Program (DMSP) together with the Operational Line-scan System (OLS, consisting of two telescopes scanning in the visible and infrared parts of the spectrum). The SSM/I is a multi-channel passive microwave system which measures the power emitted from a surface. The sensor measures at four frequencies. Three of them are separated into two polarizations, which gives seven channels. Polarization differences are used to deduce different surface and atmospheric parameters. The frequencies f, the polarization p, the wavelength λ, and the effective *Field-Of-View* (FOV) are listed in Table 3.1. The SSM/I scans the Earth's surface conically across-track while looking backwards with a constant ground incidence zenith angle of $53.1°$. The swath width is $\sim$1400 km and the low frequency channels are sampled every 25 km. About 14 over-passes per day provide a complete coverage of both polar regions with the exception of an area centred at each pole (approx. 200 km radius) which is excluded because of the satellites orbit geometry. For more information on the SSM/I instrument refer to Hollinger et al. (1987).

Table 3.1: SSM/I Sensor Characteristics

f [GHz]	p	λ [mm]	Noise [K]	FOV [km $\times$ km]
19.35	h,v	15.5	0.8	69×43
22.23	v	13.5	0.8	50×40
37.0	h,v	8.1	0.6	37×29
85.5	h,v	3.5	1.1	15×13

The two most widely applied methods to derive sea ice concentration from SSM/I data are the NASA Team algorithm (Cavalieri et al., 2002) and the Bootstrap algorithm (Comiso, 1995). The NASA Team algorithm uses the vertical polarization of the 19 GHz and 37 GHz channels and the horizontal polarization of the 19 GHz channel to determine ice concentrations. Two ratios are calculated from brightness temperatures T_b as follows:

$$PR(19) = \frac{[T_b(19\,v) - T_b(19\,h)]}{[T_b(19\,v) + T_b(19\,h)]} \quad , \qquad GR\left(\frac{37\,v}{19\,v}\right) = \frac{[T_b(37\,v) - T_b(19\,v)]}{[T_b(37\,v) + T_b(19\,v)]}$$

with the suffices v and h denoting the vertical and horizontal polarization of the frequency, respectively. The polarization ratio, PR, distinguishes between open water and ice, where open water has higher values. The gradient ratio, GR, generally discriminates between two ice types. First year ice corresponds to higher GR values than multi year ice. Two weather filters based on threshold values of $GR\,(37\,v/19\,v)$ and $GR\,(22\,v/19\,v)$ are applied to remedy deficiencies and spurious ice retrievals over open water because of wind, cloud liquid water, water vapor, and other atmospheric interferences. The use of brightness temperature ratios minimizes surface temperature effects on the retrieval of sea ice concentrations. However, the procedure has drawbacks in the ice edge resolution and a wind effect sensitivity of the $19\,h$ channel over open water. In the marginal ice zone the algorithm tends to underestimate thin ice concentrations and classifies widespread thin ice as a mixture of thicker ice and open water (Comiso et al., 1997).

The Bootstrap algorithm uses the vertical and horizontal polarization of the 37 GHz channel for the calculation of high sea ice concentration in the Arctic and the vertical polarizations of the 19 GHz and 37 GHz channels for lower concentrations in the Arctic and throughout the Antarctic. Seasonally varying tie-points (referring to pure, 100%, ice types) allow variability in the surface properties of the sea ice to be taken into account. A weather filter different from the NASA Team filter is used to reduce atmospheric effects. The Bootstrap algorithm is more sensitive to thin ice concentrations than the NASA Team algorithm, although the position of the ice edge is consistent between the two algorithms (Comiso et al., 1997). Recently, advances have been made using the

SSM/I's 85 GHz information for the retrieval of higher resolution sea ice parameters (Kern, 2001; Kaleschke et al., 2001).

3.2.2 Radar Altimeter (RA)

The principle of a pulse-limited altimeter measurement involves the shape and timing of a returned radar pulse. A pulse propagates through the atmosphere, hits the surface and is scattered to the receiving antenna of the instrument. As the signal reaches the surface the power of the echo increases with time, reaching a maximum as the illuminated area evolves from a point to a disc. Further broadening of the pulse results in an annulus shape with an approximately constant area and slowly decreasing power. Since most surfaces like the ocean are not flat but rather consist of point scatterers with normally distributed elevation, the echo rise time and pulse length increase from the optimal case described above.

The Radar Altimeters (RA) on-board the ERS satellites and on EnviSat operate at 13.5 GHz (Ku band) and are nadir pointing active microwave sensors. They are specially designed to measure the delay time and the form of the return signal from ocean, ice or land surfaces in two optimized tracking modes. In ocean mode, significant wave height and sea surface elevation measurements are used to estimate ocean topography, ocean currents, tides, and the geoid. With a coarser resolution the same measurements are made in ice mode to provide ice topography and other surface feature information. It is possible to retrieve the free-board of the ice cover by subtracting the geoid from the surface elevation deduced from the RA signal. Sea ice thickness can be calculated from the free-board estimate with regard to the density of sea ice and the overlaying snow cover. The upcoming CryoSat mission is dedicated to high resolution sea ice thickness estimates. The radar altimeter on-board CryoSat is especially designed for this purpose.

For more detailed description of altimeter principles and techniques refer to Elachi (1988).

3.3 Summary

In this study ice concentration data derived from SSM/I are used both for validation of the results and for assimilation (see Chapter 5) for the following reasons:

1. SSM/I data (NASA Team sea ice concentrations) have proven to be of good quality in many studies (e.g. Steffen et al., 1992; Dokken et al., 2000; Kauker et al., 2003) and are used widely in the scientific community,

2. the data cover almost the entire Arctic except for the so-called Pole-hole which is due to the orbit constraints of the satellite,

3. the sensor is independent of daylight and insensitive to clouds and is, therefore, weather independent,

4. the data have a horizontal resolution similar to the numerical model (approximately 27 km), and

5. the data are available in near-real time from the National Snow and Ice Data Center (NSIDC), USA.

Radar altimeter data from ERS are not available in near-real time and do not offer global coverage. However, the sensor is able to detect the sea-ice edge quite well and therefore the data are used for validation purposes.

Chapter 4

Modelling Experiment with new Boundary Conditions

This chapter addresses the effects of the new oceanic and atmospheric boundary conditions for the simulation of sea ice (see Section 2.3). Examples for different seasons are presented to show the improvements in the sea ice concentration fields and these results are validated with SSM/I sea ice concentration data (see Section 3.2.1).

Hilmer (2001) studied the simulated Arctic sea ice variability with a SIOM ocean boundary and NCEP and ECMWF atmospheric forcing. His model was run on a $1° \times 1°$ grid for the years 1949-1998 and applied the same physics as the model used in this study, except for the newly applied fast ice parameterisation. He showed that the model is able to reproduce observed inter-annual sea ice variability. Here, the effect of using improved forcing data on model results is tested. Three different high resolution model set-ups were run for a period starting in September 1994 and ending in December 1995. The gain in performance of sea ice concentration estimation due to changed boundary conditions in a year with an unusually low summer sea ice coverage is demonstrated. In summer 1995, observations showed minimal sea ice extent which is attributed to an unusual oceanic surface warming event transporting up to 20 TW additional surface heat flux into the Greenland Sea as compared to previous years (Karcher et al., 2003). For validation purposes, monthly mean sea ice concentrations were computed from monthly mean remote sensing data to investigate the performance of the numerical model in this unusual case.

The original set-up consisted of oceanic data derived from SIOM and atmospheric forcing derived from NCEP re-analyses (hereafter referred to as S+N run). The second combination of forcing parameters comprised the new seasonal ocean surface climatologies (derived from MOM, see Section 2.3.2) and NCEP atmospheric data (hereafter referred to as M+N run). For the third parameter set-up the NCEP data were substituted with ECMWF analyses (hereafter re-

Table 4.1: Overview of forcing combinations

Forcing variable			S+N	M+N	M+E
Oceanic forcing	Currents	No. of fields	1	12	12
		Resolution	$1°$	$\frac{1}{4}°$	$\frac{1}{4}°$
		derived from	SIOM	MOM	MOM
	Heat flux	No. of fields	12	12	12
		Resolution	$1°$	$\frac{1}{4}°$	$\frac{1}{4}°$
		derived from	SIOM	MOM	MOM
Atmospheric forcing		Fields provided	daily	daily	6-hourly
		derived from	NCEP	NCEP	ECMWF

ferred to as M+E run). The combinations of forcing fields used in this study are summarized in Table 4.1 (the forcing fields are described in Section 2.3).

As a measure of the quality of changes, the Root-Mean-Square Error (RMSE) of simulated sea ice concentration compared to SSM/I ice concentration data is calculated for each model set-up. The error is calculated using RMSE $= \frac{1}{n}\sqrt{\sum_{i=1}^{n}(\vec{x}_i(t) - \vec{y}_i(t))^2}$ where n is the number of data points i, and $\vec{x}$ and $\vec{y}$ are model and SSM/I data, respectively, at a given time t. Low values of RMSE indicate good agreement between the data sets. Lack of SSM/I data at the pole excludes this area from consideration. Time series of RMSE between SSM/I and model results for each of the different forcing sets show partly similar performance (Figure 4.1).

All model runs were initialized with the same restart conditions of sea ice volume, concentration, age, snow thickness, and mixed layer temperature. The different set-ups reproduce the first freeze-up season in good agreement with the observations, even though the performance varies significantly in different regions. During the winter season the model output (all set-ups) tends to overestimate sea ice concentration, resulting in increasing RMS-Errors which indicate a large difference between the two data sets. The agreement with observations is less pronounced for all three set-ups in summer, but increases during the following freeze-up period. However, the different boundary condition combinations produce a very similar mean RMSE for the whole model domain for the reference period.

4.1 Seasonal Investigations

In the following sections sets of model runs are compared to SSM/I data to study the influence of different forcing data combinations as defined in Table 4.1 in
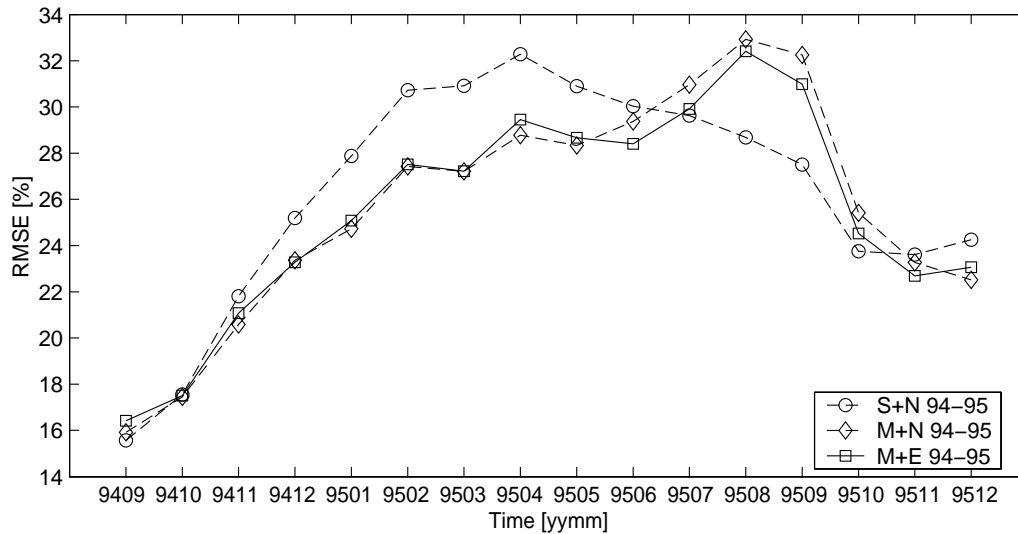
Figure 4.1: Root-Mean-Square Error of sea ice concentration for the reference period of September 1994 to December 1995. The mean RMSE for the S+N set-up is 26.26±4.93%, for the M+N set-up 25.65±4.97%, and for the M+E set-up 25.51±4.64%.

different seasons.

4.1.1   Summer

The late summer sea ice situation, represented by the September mean sea ice concentration in Figure 4.2, reveals large regional differences between the three model runs. Since all model set-ups start with the same initial condition the discrepancies have to be attributed to the type of forcing. The run with the original set-up (S+N run, see Figure 4.2(a)) clearly overestimates the sea ice concentration in the eastern part of the Russian Arctic and in Baffin Bay, where no ice is detected by remote sensing (Figure 4.2(d)). However, the situation east of Greenland and in the Chukchi Sea is in good agreement with the SSM/I data.

Introducing a different ocean forcing to the model driven with NCEP atmospheric fields (M+N run) has little effect on the RMSE value for ice concentration in September, although the total ice-covered area is even more overestimated than with SIOM oceanic forcing (see Figure 4.7). This situation is completely different for the M+E run which underestimates the sea ice conditions in the Chukchi Sea and dramatically so in the Greenland Sea. A more realistic sea ice representation can be found in the Barents and Kara Seas. Baffin Bay is ice free as seen in SSM/I data, but the Laptev Sea sea ice is still overestimated, although sea ice off the Taymyr Peninsula is not simulated as in the S+N and M+N runs. Interestingly, the ice free area east of the New Siberian Islands which is detected with SSM/I data is reproduced with this set-up.

Overall, the simulation with the M+E run shows improvements in the marginal

(a) SIOM ocean + NCEP atmosphere

(b) MOM ocean + NCEP atmosphere

(c) MOM ocean + ECMWF atmosphere

(d) SSM/I

Ice Concentration [%]

0   20   40   60   80   100
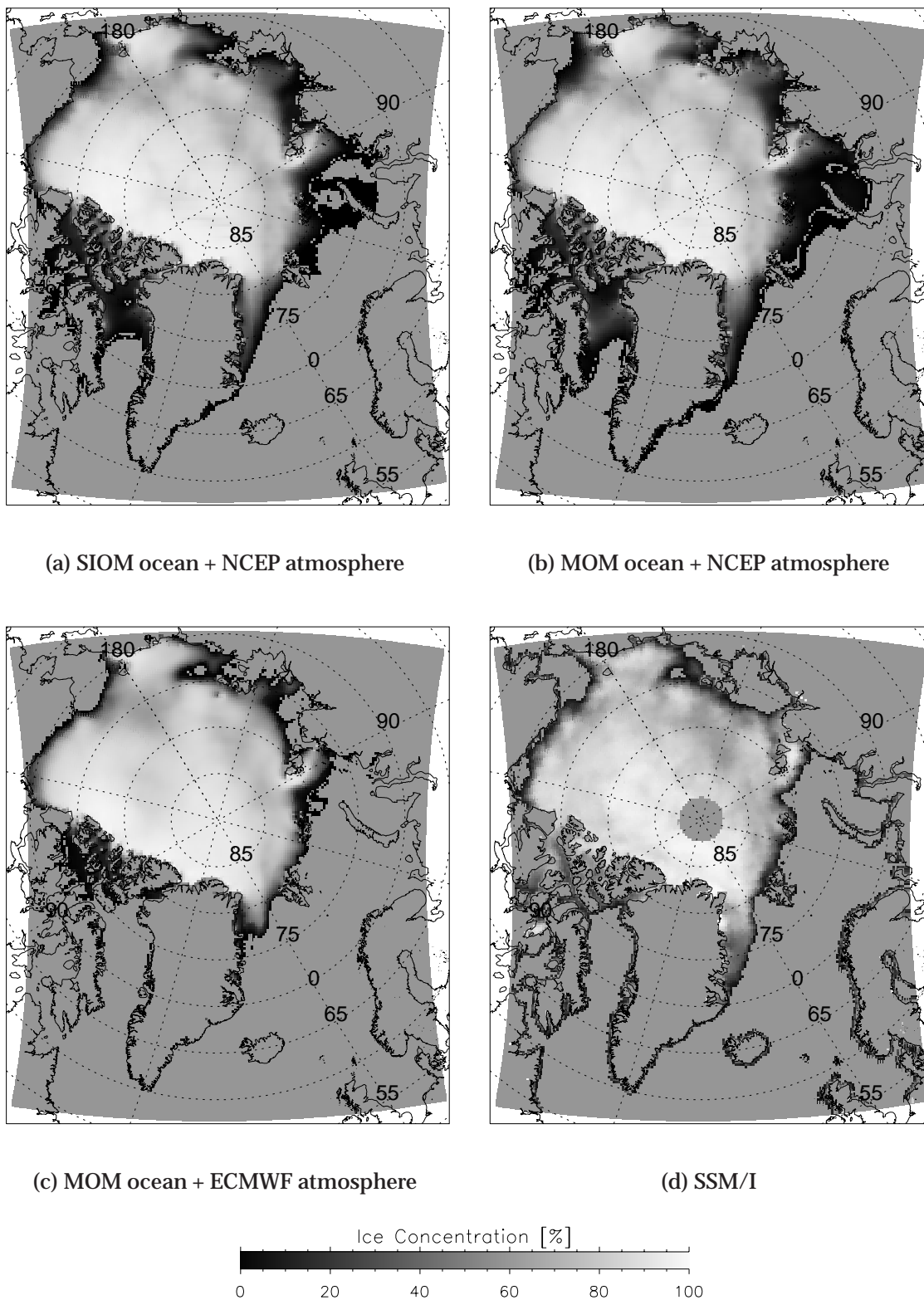
Figure 4.2: Monthly mean sea ice concentration computed with different atmospheric and oceanic boundary conditions for September 1994 as an example of summer conditions. Panel (a) shows results from a run with the original SIOM ocean boundary condition and NCEP atmospheric reanalysis data. Panel (b) shows results forced with new MOM ocean and NCEP data. Panel (c) shows results forced with MOM ocean and ECMWF atmospheric analysis, and panel (d) shows the situation as seen from SSM/I.

42

ice zone regions along the Siberian coast and in Baffin Bay compared to the S+N and M+N runs. However, the reproduction of sea ice east of Greenland is unsatisfactory. Warm ECMWF atmospheric forcing in this region seems to be responsible for the low ice concentration. Low ice concentrations resulting from the restart conditions are quickly further reduced by melting in early September, and only transport through the Fram Strait and lower surface temperatures re-establish a more realistic ice cover in the following months in the Greenland Sea.

4.1.2 Winter

November 1994 (Figure 4.3) represents the conditions in early winter. The influence of the improved ocean boundary condition is much more obvious than in the summer situation. The S+N run computes higher ice concentrations in Baffin Bay, the Greenland Sea and the Barents Sea, especially around Svalbard, compared to SSM/I data. MOM ocean current and ocean heat fields improve the simulation significantly in this region with both NCEP and ECMWF atmospheric forcing. The M+N and the M+E results show good agreement compared to SSM/I data. Although the RMSE for the M+E experiment has a similar value as for the S+N experiment, M+E shows the best performance in the Greenland Sea and simulates sea ice extent in good agreement with the observations. Too little sea ice area in the Denmark Strait appears to be due to low ice concentrations in the preceding autumn as indicated in Figure 4.2(c). Also, ice concentrations seem to be underestimated in the Kara Sea and Baffin Bay where the M+N run produces the most realistic results. The best results for the Chukchi Sea and south of the Bering Strait are generated with the S+N set-up. East of the New Siberian Islands all model set-ups show lower ice concentrations along the coastline and a landfast ice area. This is not found in the remote sensing data.

The sea ice area for February 1995 is shown as an example for late winter conditions (Figure 4.4). The general tendency to overestimate sea ice is visible for all model set-ups. All forcing combinations lead to an unrealistic sea ice extent in both the Greenland Sea and the Davis Strait. Although the M+N and M+E simulations give very similar RMS-Errors, the interaction of MOM-derived oceanic forcing with the ECMWF atmosphere gives the best representation north of Iceland and in the Davis Strait. Conditions in the eastern Barents Sea, however, are best simulated in the M+N run. Sea ice around Svalbard is badly represented in all model runs. However, the M+E run reproduces the indented sea ice edge representation found in observational data. The retreat of the sea ice edge south of Svalbard may be under-represented due to the seasonal climatological ocean forcing. Karcher et al. (2003) found a northward advection

(a) SIOM ocean + NCEP atmosphere

(b) MOM ocean + NCEP atmosphere

(c) MOM ocean + ECMWF atmosphere

(d) SSM/I
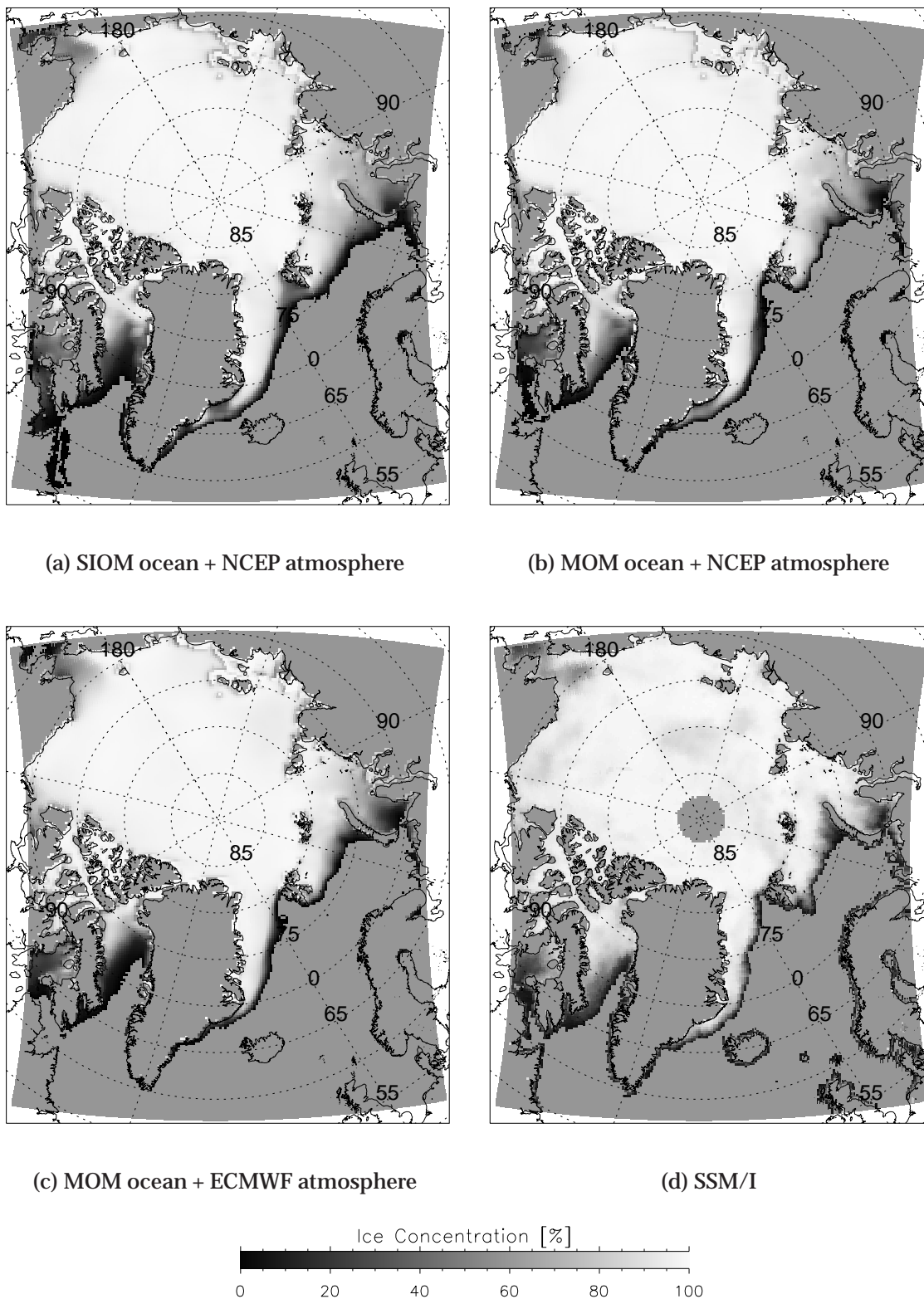
Figure 4.3: Same as Figure 4.2 but for November 1994 as an example of early winter conditions.

(a) SIOM ocean + NCEP atmosphere

(b) MOM ocean + NCEP atmosphere

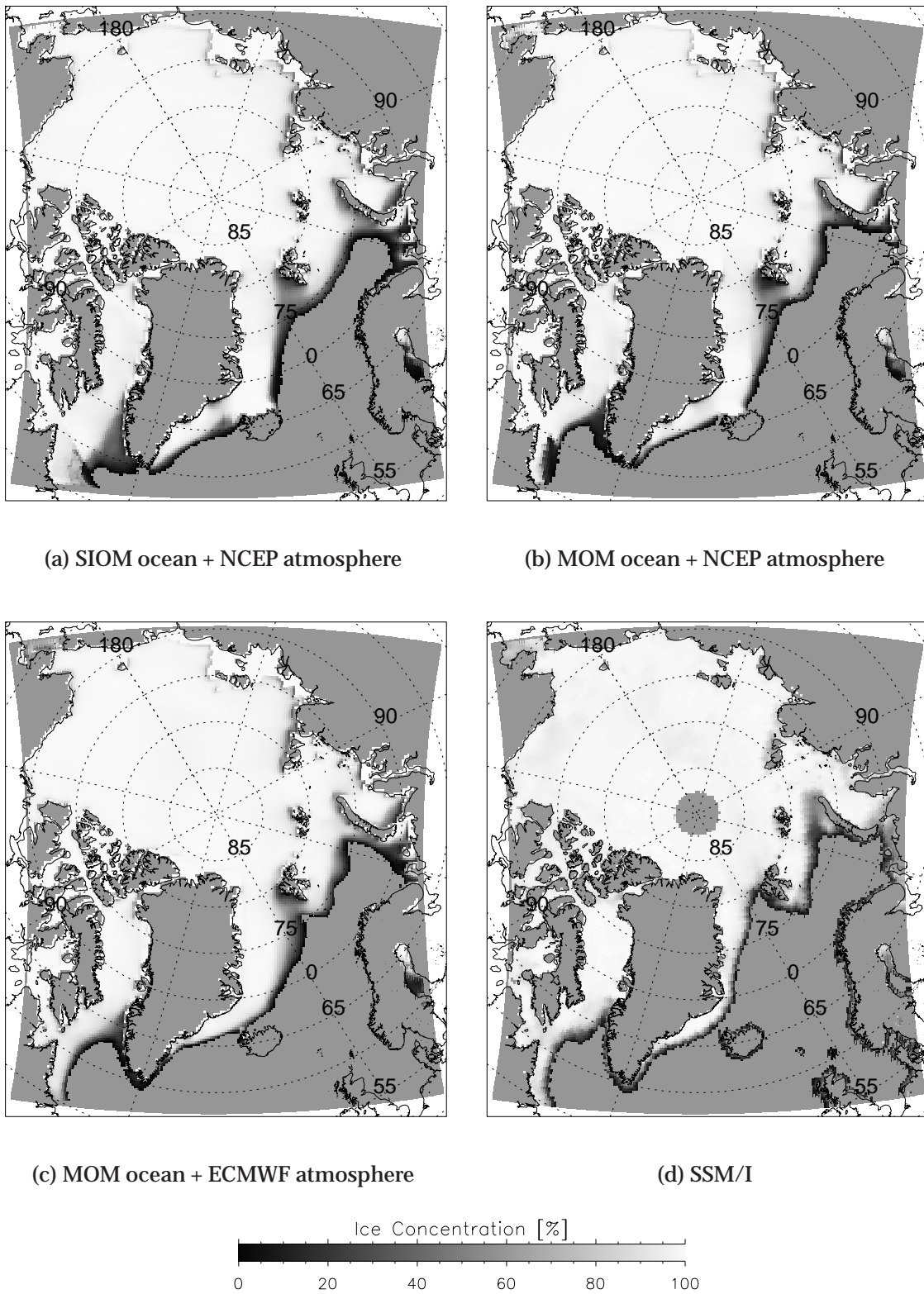(c) MOM ocean + ECMWF atmosphere

(d) SSM/I

Figure 4.4: Same as Figure 4.2 but for February 1995 as an example of late winter conditions.

of warm water from the Norwegian Sea which in turn reduced the sea ice cover in this region. The heat content of the model mixed layer is too small to melt the larger amount of sea ice advected into this area, so that sea ice concentration is overestimated in this season.

Observations over many years show a more or less persistent polynya off the Siberian coast which is the most productive region for sea ice in the Arctic. Lower ice concentrations in lee of islands like Franz-Josef-Land and Severnaya Zemlya are represented in agreement with remote sensing data. However, in the case of fast ice, there have been no analyses of spatial and temporal variability along the Siberian coast. This means that the validation of the model's fast ice results must be the subject of a future investigation (see Section 7.2).

4.1.3 Melting

June 1995 monthly mean sea ice concentration fields are displayed in Figure 4.5 to illustrate conditions during the melting season. The sea ice extent is still too large in the Greenland Sea and Davis Strait for all set-ups. Again, this can be attributed to the previous winter where all set-ups produced too much ice. Significantly overestimated ice concentrations north of Iceland remain trapped, especially in the S+N run, and are not sufficiently reduced by melting to match the SSM/I ice concentration. Continuous transport along the south-eastern coastline of Greenland and ongoing melting of sea ice in the western Irminger Sea causes thinning, as is visible in the lower ice concentrations in the southern Denmark Strait (Figure 4.5(a)). The sea ice reservoir at the northern coast of Iceland can not be "flushed" and thus the sea ice field seems to be stretched to the south-west. This can be attributed to the fact that the SIOM ocean current field provided no surface drift information for the model south of approx. $65\,^\circ$ N (see Figure 2.9(a)). In July (not shown) at the location at around $30\,^\circ$ W and $65\,^\circ$ N there is a gap in the modelled sea ice concentration field. Sea ice north of Iceland is stuck at the barrier of the island.

Lower ice concentrations in polynya regions off the Siberian coast are simulated in agreement with remote sensing data owing to the fast ice parameterization. The clearly visible Western New Siberian Polynya (see Section 2.1.5) is reproduced by all set-ups, with the M+E run giving this most realistical simulation showing lower ice concentrations along the northern coast of Severnaya Zemlya. In the eastern Laptev Sea the fast ice area between the polynya region and the coastline appears in the SSM/I data with homogeneous low ice concentrations. This may be due to difficulties of the microwave technique in summer months, when melting of snow cover on sea ice begins (Cavalieri et al., 2002) due to increasing short-wave radiation and rising air temperatures when

(a) SIOM ocean + NCEP atmosphere

(b) MOM ocean + NCEP atmosphere

(c) MOM ocean + ECMWF atmosphere

(d) SSM/I

Figure 4.5: Same as Figure 4.2 but for June 1995 as an example of meltdown conditions.

(a) SIOM ocean + NCEP atmosphere

(b) MOM ocean + NCEP atmosphere

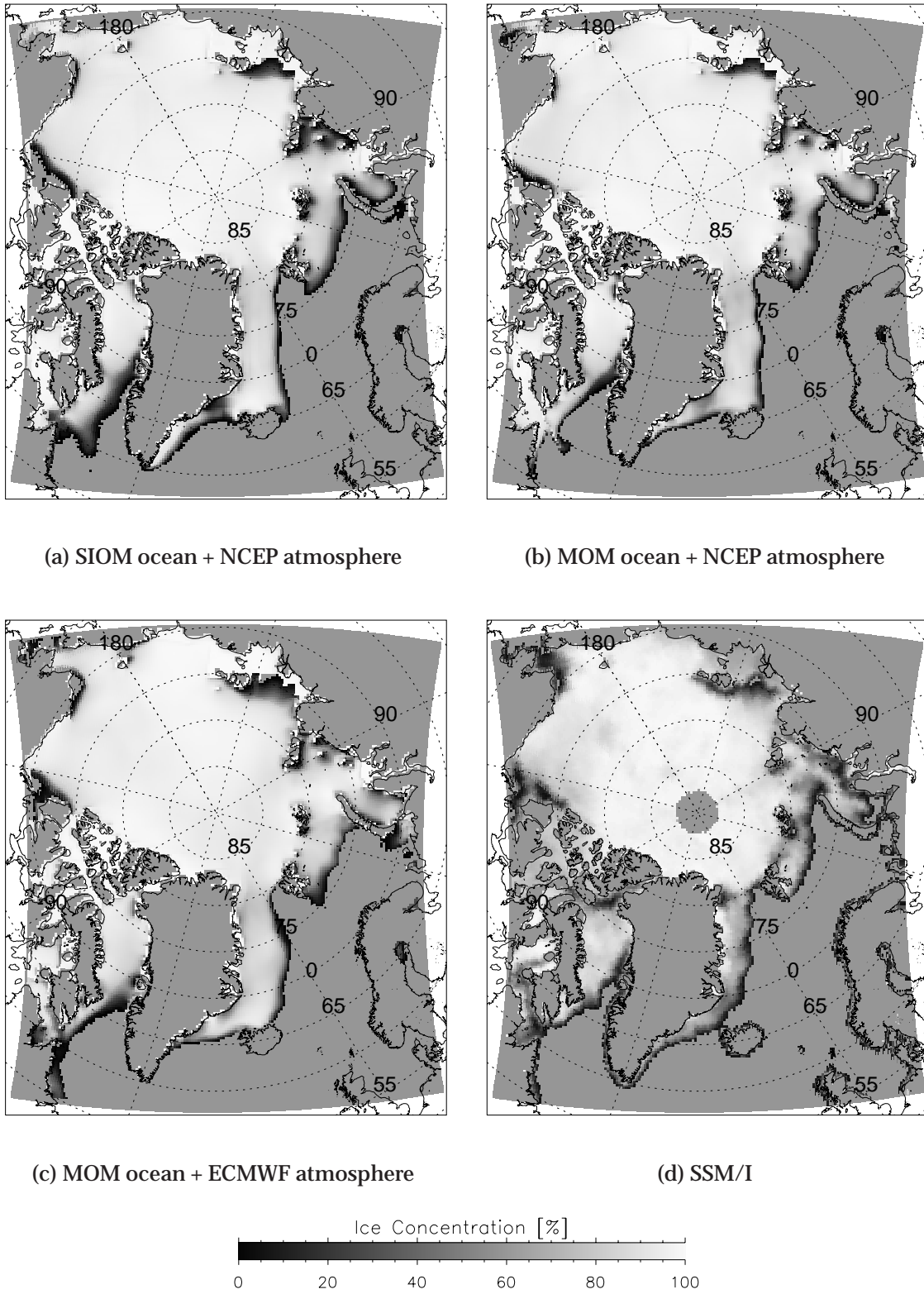(c) MOM ocean + ECMWF atmosphere

(d) SSM/I

Figure 4.6: Same as Figure 4.2 but for October 1995 as an example of freeze-up conditions.

the polar night is over. The determination of sea ice concentration from passive microwave data is then impaired by the wet surface of sea ice (for example melt-ponds) which are erroneously identified as open water.

4.1.4   Freeze-up

The simulations of the 1995 freeze-up season (see Figure 4.6) show very good agreement with SSM/I data. The S+N set-up tends to overestimate sea ice extent in the Greenland Sea and in the Denmark Strait. This is probably due to an overestimation of modelled sea ice drift in the Greenland Sea when compared to drift computed from sequential SSM/I imagery (T. Martin, 2003, pers. comm.). For a similar model set-up Hilmer (2001) found unusually high values of sea ice export through the Fram Strait for the year 1995. This can be attributed to a strong high pressure system over the Beaufort Sea in October 1995, which intensified the ice drift in the central Arctic (Transpolar Drift). Additionally, a northeastward relocation of the Islandic low pressure system towards the Norwegian Sea increases the transport along the East Greenland coast and thus a larger sea ice extent in this region. Also, the simulations of the freeze-up season start with an overestimated summer situation, which consequently results in overly high values for sea ice concentration.

4.1.5   Sea Ice Extent

The time series of sea ice extent (Figure 4.7) shows the general performance of the different numerical model set-ups. Sea ice extent derived from observations and from model results show similar behaviour for the reference period. All model set-ups depart from SSM/I data in the first winter when the model starts to overestimate sea ice concentration. This is most likely because the oceanic heat flux into the mixed layer is limited by the boundary prescription. The ocean heat flux as supplied to the model represents a heat reservoir which is used to melt sea ice if present or might be exhausted by a cold atmosphere before sea ice forms. A very cold atmosphere can, then, initiate sea ice formation quite fast and efficiently. If sea ice is already present (in winter months) an underestimation of the mixed layer heat content results in an overestimation of sea ice extent.

During the entire freezing season (shaded grey in Figure 4.7) the models simulate too much sea ice, which is not reduced in the following summer season. This leads to an overestimation of sea ice concentration in summer in addition to the underestimation of the ocean heat flux as described earlier. Only in October 1995 is the simulated sea ice extent close to the observations again but the tendency to resumed overestimation is apparent already.
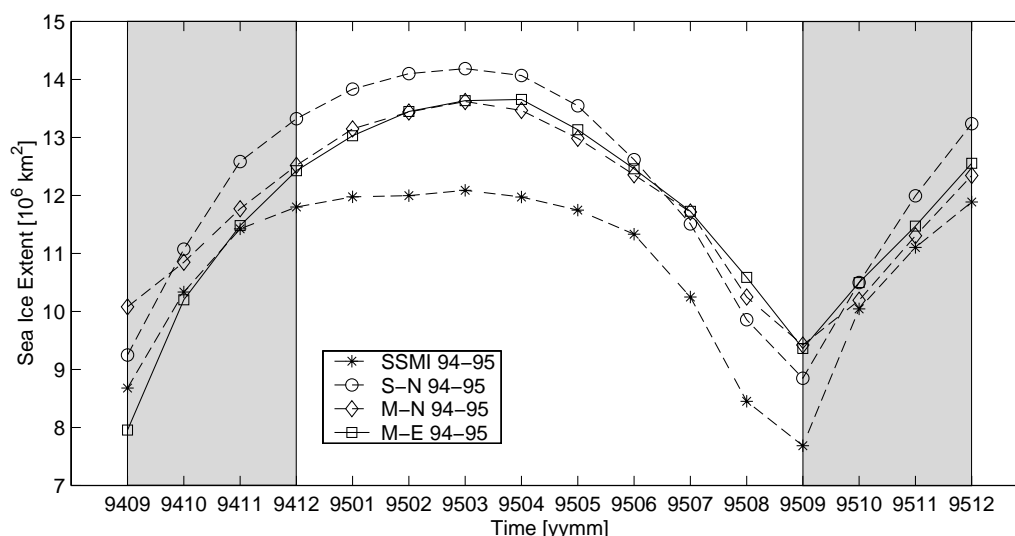
Figure 4.7: Sea ice extent for the reference period of September 1994 to December 1995. The freezing season is shaded grey.

4.2 Regional Investigations

The following two sections discuss the response of the model to various atmospheric and oceanic forcing combinations for two specific regional studies in more detail. The regional differences in the simulation of sea ice concentrations with different forcing set-ups are most obvious in the marginal seas, for example the Greenland and Barents Seas, whereas the interior of the Arctic Ocean is reproduced similarly in all set-ups.

The Greenland Sea (see Section 4.2.1) is a good example where the combination of the improved oceanic boundary condition with ECMWF atmospheric forcing produces more realistic results than with NCEP forcing. In contrast, the Barents Sea (see Section 4.2.2) is reproduced more realistically with NCEP atmospheric conditions than with ECMWF data during the reference period. To quantify these differences this section is dedicated to a regional investigation of the deviations in sea ice concentrations between the various model forcing combinations and SSM/I-data.

4.2.1 The Greenland Sea

Figure 4.8 shows sea ice concentration differences in the Greenland Sea region. The grey-scale indicates concentration values of the model simulation minus remote sensing data (SSM/I). The example shows differences between the set-ups. In November 1994 the S+N set-up overestimates the sea ice edge in the entire Greenland Sea. The same applies for the M+N set-up, but less locations (grid points) are overestimated and absolute values of overestimation are lower,
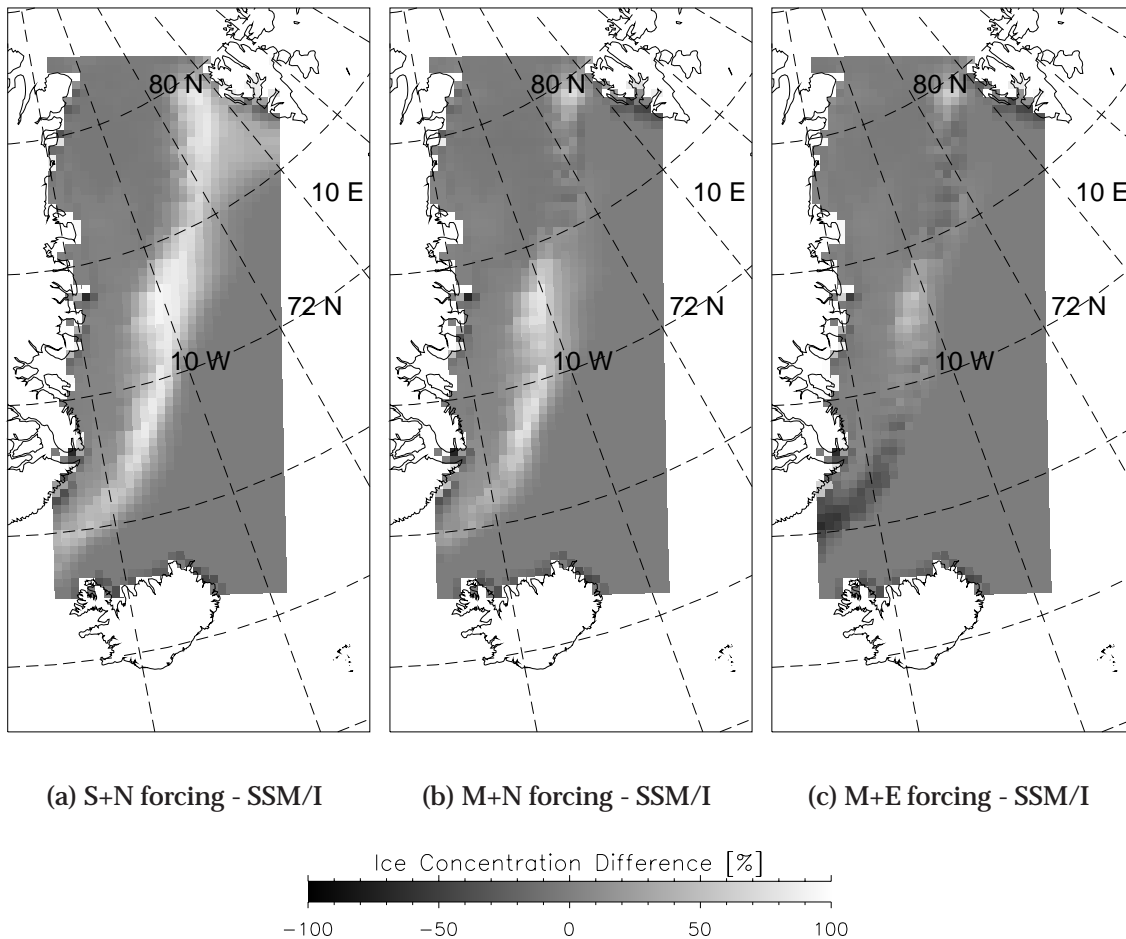
| (a) S+N forcing - SSM/I | (b) M+N forcing - SSM/I | (c) M+E forcing - SSM/I |

Figure 4.8: Sea ice concentration differences for mean sea ice concentrations in November 1994 as depicted in Figure 4.3 for different forcing combinations minus remote sensing data (SSM/I) for the Greenland Sea region. Bright areas indicate model overestimating sea ice concentrations as compared to SSM/I data, dark areas indicate model underestimation.

especially in the north. The M+E set-up tends to underestimate sea ice in the southern part of the Greenland Sea and thus simulates the sea ice edge too far north. However, the M+E combination positions the ice edge as detected by the SSM/I in the central and northern parts of the Greenland Sea.

From this analysis histograms are computed giving the number of occurrences of over- and underestimation in ten-percent intervals. Such histograms are shown in Figures 4.9, 4.10 and 4.11 as contour diagrams for the three different model set-ups. All plots show the temporal development of the differences, with time indicated on the abscissa, and the differences on the ordinate, so that the degree of overestimation can be read from these diagrams. Vertical sections through these contour plots would give a typical histogram structure for a specific date. The contour-lines are drawn on quasi-logarithmic intervals for the number of occurrences. The upper part of each plot gives the overestimation,

Figure 4.9: Monthly mean Greenland Sea sea ice concentration differences for the reference period as a contour plot of numbers of occurrence for the SIOM oceanic and NCEP atmospheric forcing combination (S+N setup).

Figure 4.10: Monthly mean Greenland Sea sea ice concentration differences for the reference period as a contour plot of numbers of occurrence for the MOM oceanic and NCEP atmospheric forcing combination (M+N setup).
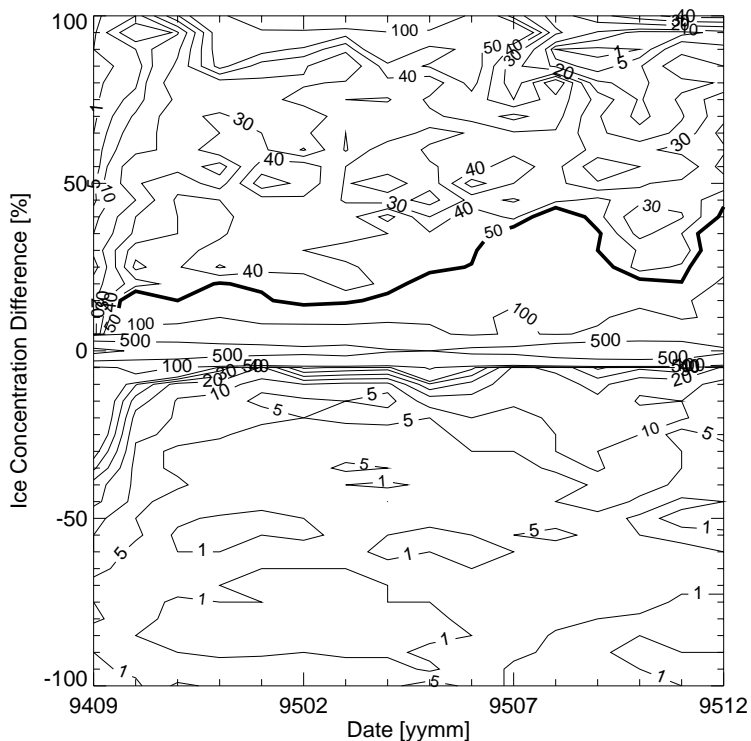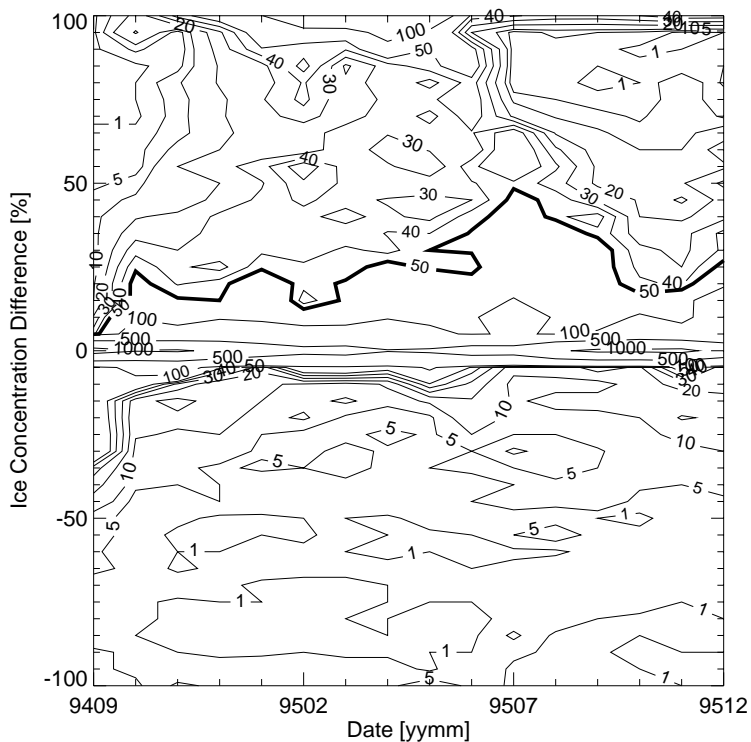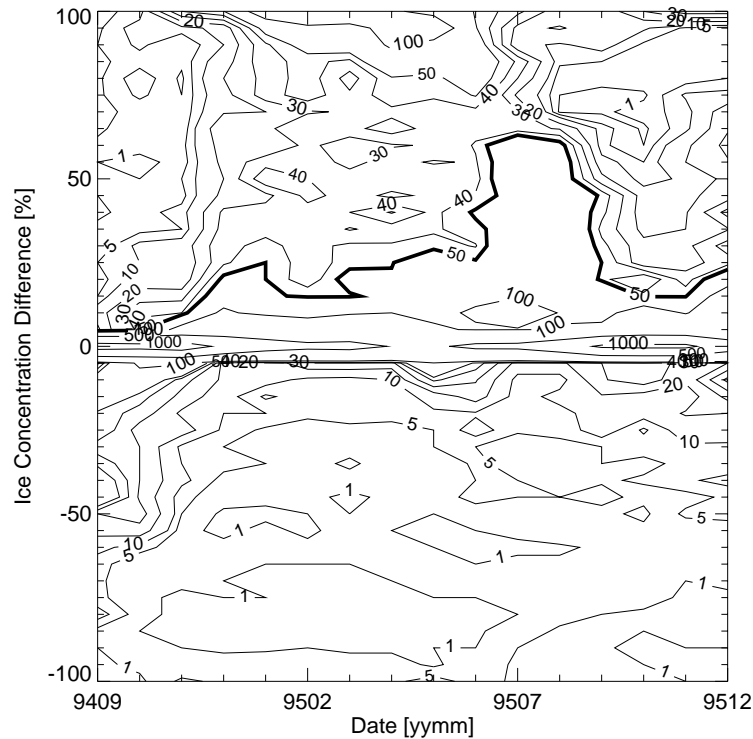
Figure 4.11: Monthly mean Greenland Sea sea ice concentration differences for the reference period as a contour plot of numbers of occurrence for the MOM oceanic and ECMWF atmospheric forcing combination (M+E setup).

the lower part the underestimation of the numerical model. The zero-line in the middle has the highest occurrences, because in general ice covered and ice free regions are reproduced realistically.

The S+N set-up (Figure 4.9) produces too much sea ice in the Greenland Sea. The overestimation increases during the course of the reference period. This is most obvious from following the isoline of 50-occurrences (plotted bold in Figures 4.9, 4.10 and 4.11) which reaches almost the 50% difference value in summer 1995. This means that sea ice concentration at nearly 50 grid points (i.e. locations) out of 1755 (or 3%) which are defined as Greenland Sea is overestimated by 50%. This isoline drops only slightly during the autumn and increases again towards the end of the period.

Similar behaviour of the 50-occurrences isoline can be seen for the M+N set-up (Figure 4.10). Again, the number of overestimated locations increases during the summer season but here the decrease during the following cold season is more pronounced. The number of occurrences of ice concentration overestimation by 100% is somewhat higher throughout the last third of the reference period compared to the S+N set-up.

The diagram for the M+E set-up as depicted in Figure 4.11 still shows an overestimation of sea ice concentration in the Greenland Sea, but the overall performance appears to be the most reasonable. Again, the isoline of 50-

occurrences increases during the reference period showing unsatisfactory simulation for the summer months of 1995. However, during the following freezing season overestimation occurs at fewer locations than with the other set-ups. Note that the number of occurrences around zero ice concentration difference is highest in the M+E set-up. This shows that the sea ice concentration is best reproduced by this forcing set-up.

4.2.2 The Barents Sea

The Barents Sea region is depicted in Figure 4.12. In contrast to the previous example in the Greenland Sea, the difference in the model response to the various forcing set-ups is clearly visible. The M+N forcing produces the smallest deviations compared to the SSM/I data, although it shows a slight underestimation of the ice extent. The sea ice concentration is clearly overestimated by the S+N set-up and clearly underestimated by the M+E set-up in the simulations for November 1994. During the course of the reference period all models tend to overestimate the sea ice concentration in the region. This can be seen in Figures 4.13, 4.14 and 4.15 showing the contour diagrams of number of occurrences of

(a) S+N forcing - SSM/I   (b) M+N forcing - SSM/I   (c) M+E forcing - SSM/I
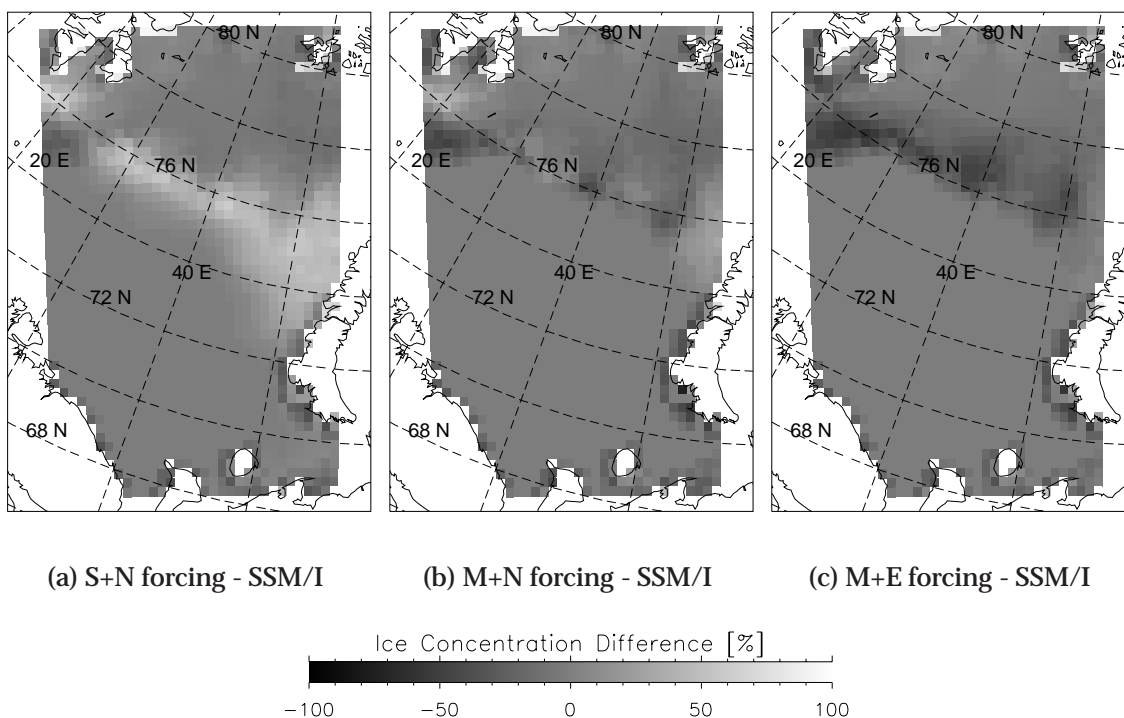
Figure 4.12: Sea ice concentration differences for monthly mean sea ice concentrations as depicted in Figure 4.3 for different forcing combinations minus remote sensing data (SSM/I) for the Barents Sea region. Bright values indicate model overestimating sea ice concentrations as compared to SSM/I data, dark values indicate model underestimation.

Figure 4.13: Monthly mean Barents Sea sea ice concentration differences for the reference period as a contour plot of numbers of occurrence for the SIOM oceanic and NCEP atmospheric forcing combination (S+N setup).

Figure 4.14: Monthly mean Barents Sea sea ice concentration differences for the reference period as a contour plot of numbers of occurrence for the MOM oceanic and NCEP atmospheric forcing combination (M+N setup).

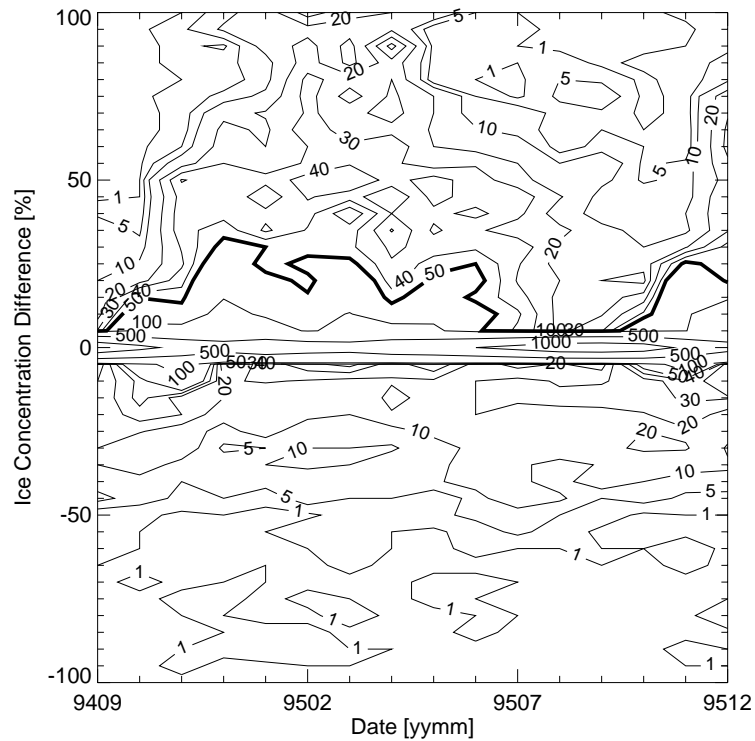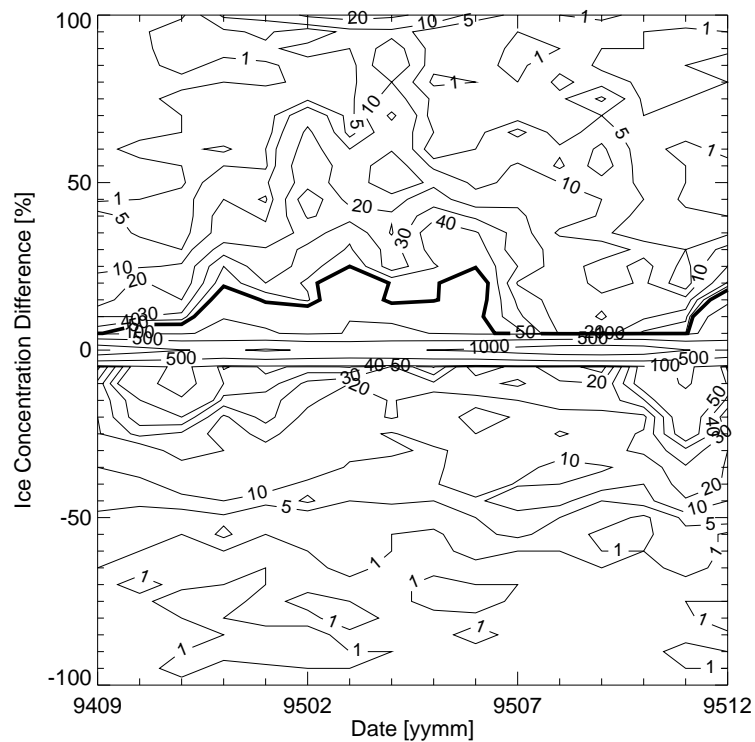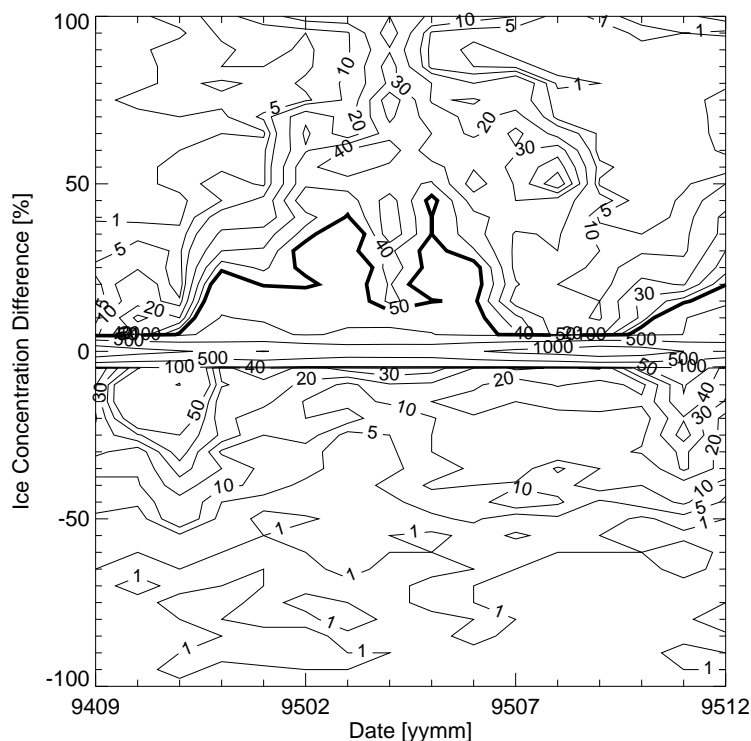**Figure 4.15:** Monthly mean Barents Sea sea ice concentration differences for the reference period as a contour plot of numbers of occurrence for the MOM oceanic and ECMWF atmospheric forcing combination (M+E setup).

sea ice concentration differences for the different forcing combinations.

In spring 1995 the overestimation of sea ice concentration is highest in all set-ups. The S+N set-up shows unsatisfactory performance simulating too much sea ice especially in the southern Barents Sea as can be seen in Figure 4.4. This applies also for the M+E set-up, which overestimates ice concentration even more. The best (but still overestimating) simulation is achieved with the M+N forcing combination. All contour plots show that the degree of overestimation decreases during the summer season for all set-ups, with the highest number of zero-differences for the M+N set-up. During the freezing period the S+N and M+E set-ups start to overestimate the sea ice concentration quite rapidly again, whereas the M+N set-up simulates more realistic results.

4.3 Summary

Looking at the RMS-Errors globally for the whole model domain (see Figure 4.1) use of different atmospheric forcing data shows little effect. The mean RMS Errors for all set-ups are very close at about $25\pm5\%$ for the reference period. However, there are differences in distinct geographical regions. Concluding from the previous sections, the Barents Sea is much more realistically simulated with

NCEP compared to ECMWF forcing during late winter and the meltdown season. On the other hand, the Greenland Sea north of Iceland is simulated better with ECMWF forcing during the same periods. The good performance of the M+N run in the marginal ice zone may be due to the interaction with the MOM-derived ocean forcing which was calculated with NCEP atmospheric forcing.

Introducing a new, more realistic ocean boundary condition to the numerical model yields more realistic sea ice conditions. Despite this, a seasonal climatological ocean is not able to reproduce inter-annual variability and events in ocean current or heat flux fields. Therefore, a coupled ocean-sea ice system performs better with forcing prescribed daily for the atmosphere and a prognostic ocean model. Kauker et al. (2003) have shown that such a coupled model simulates the statistical modes of the observed inter-annual variability of sea ice to a high degree of accuracy for the period from 1978 to 2001. However, the computation of the entire ocean requires much computational power and extends model run-times. For the use of a sea ice forecast model a fast and efficient numerical model is needed.

A study carried out by Curry et al. (2002) evaluated different atmospheric forcing data sets for use in sea ice models for the Arctic Ocean, including NCEP and ECMWF results. The Surface Heat Budget of the Arctic Ocean (SHEBA)[1] field experiment is the reference period for their analysis (October 1997 until October 1998). The authors were not able to give a particular suggestion as to which data set would be most suitable for this task. However, they found that ECMWF air temperatures tended to produce warmer values compared to the measurements, whereas NCEP air temperatures, were biased toward cooler temperatures but ECMWF winds were better than NCEP winds (at least for their reference period).

In the experiments shown here the M+E run performs best for the entire model domain even under difficult conditions which are hard to represent with climatological forcing. The improvements in key locations along the sea ice edge (around Svalbard and in the eastern Barents Sea) and the fact that ECMWF atmospheric fields are available as forecast data makes this combination most appropriate for further use. For the work described in the following sections, the numerical model will be run as a computationally fast, stand alone sea ice model with ECMWF atmospheric forcing.

---

[1]An overview of the SHEBA field experiment is given by Perovich et al. (1999)

Chapter 5

Data Assimilation

This section deals with the problem of finding the best initial conditions for the prediction of the physical properties (e.g. concentration) of sea ice cover. After an introduction of the notation used in this context (following Bouttier and Courtier, 1999), the chosen assimilation method, Optimal Interpolation (OI), is described and justified.

5.1   Introduction to Terminology

An *analysis* refers here to the best possible determination of the real state of a physical system at a given time represented in a model by a vector. If an analysis is comprehensive and self-consistent it may be useful for understanding the system and its change. But it can also be used as an initial state for a numerical simulation, or, if no observation data are available, as a pseudo-observation. Another application of an analysis is as a reference against which to check the quality of single observations.

A vital part of an analysis is a good-quality first guess of the state of the system. The plausibility of these data must be known. The true state may lie near the average of dense observations whereby suspicious data should be given little weight. This leads to a compromise between the first guess and the observations. Also, the analysis should be smooth because the physical fields are, but it is still possible that exceptional cases occur and the analysis should be able to accept those exemptions.

The information for the analysis is basically a collection of observations of the real state. An analysis reduces to an *interpolation* problem if the model state is over-determined by the observations. Under-determination due to sparse data or to data being only indirectly related to model variables is more common. Historically, the analysis of, for example, a weather situation carried out by a meteorologist (by drawing isolines on a map) was dependent on the profes-

58

sional judgment of the forecaster. Gilchrist and Cressman (1954) suggested interpolating observational data to a model grid for an analysis. A single measurement of a quantity can not be inter- or extrapolated onto a computational grid but a model can provide simulations for any point. Therefore, the aim should always be to find the model state that agrees best with the observations.

A well posed problem relies on some *background* information, e.g. an *a priori* estimate of the model state or physical constraints on the analysis problem. Such background information can be a climatology, a trivial state, or a previous analysis of a model output if the model is assumed to be consistent in time (hypothesis of persistence). It is expected that this allows the information to be accumulated in time into the model and to propagate to all variables of the model for a well-behaved system. This is the concept of the data analysis technique called *assimilation*.

Data assimilation techniques can be divided by two distinctive pairs of features into four categories:

- Sequential, intermittent assimilation:
  Using a sequential intermittent technique the assimilation procedure considers only past observations for the analysis. This method is applied in real-time assimilation systems, where the observations are processed separately, meaning that the model integration is stopped for the assimilation process and the model starts with a new initial condition.

- Sequential, continuous assimilation:
  A sequential continuous method also relies on past information, but the assimilation is carried out parallel to the model run. This results in a chronologically smooth correction of the analysis, which is much more realistic.

- Non-sequential, intermittent assimilation:
  In contrast to the sequential approach a non-sequential or retrospective method, as used in re-analysis experiments, considers both future and past observations for the analysis. But the intermittent method leads to a discontinuous result, although it is an improvement on the sequential intermittent method.

- Non-sequential, continuous assimilation:
  The non-sequential, continuous technique overcomes this problem by running model and analysis in parallel. This is the optimal procedure for re-analyses.

Many different realizations of assimilation methods and compromises of the above mentioned techniques have been developed in meteorology and ocean-

ography. They can be applied to one-, two-, or three-dimensional models of limited area as well as to global models, for example at ECMWF. Depending on numerical cost, suitability and aptness for the investigated problem adequate implementations have to be chosen. For more detailed descriptions refer to Daley (1991) or Ghil (1989).

However, a model will always have a lower resolution than reality demands and the best possible analysis will not necessarily be completely true. In this context the true state of the model is the approximately best state of the model, which can be achieved. And even if it is assumed that the observations have no instrumentational error and the analysis is equal to the true state, there will be discrepancies between the values of the observation and their modelled equivalent. Those errors will be treated as *observation errors*, although they are dependent on model discretization and not instrumental problems (Bouttier and Courtier, 1999).

5.2   Cressman Analysis - Successive Correction Method

In order to obtain a good forecast, information on the initial state should be provided for all degrees of freedom, and the model should include the complete dynamics of the system. One of the limits on the correctness of the estimated initial condition is imposed by the method used to estimate the analysis from the information contained both in the observations and the background field. The simplest method is to overwrite the background with the new data by assigning the value of the observation to the closest grid point. This is a good procedure if the observations are accurate, but the method fails when observational errors are substantial, because the errors of the assimilated condition can not be smaller than those of the observations. Also, this procedure may introduce unphysical spikes and discontinuities into the initial condition. An alternative to simply replacing the background value is to spread the influence of each observation to neighbouring grid points as in the method of successive corrections (Bergthorsson and Döös, 1955; Cressman, 1959), but the range of the influence must be determined empirically.

The previous estimate of the model state $\mathbf{x}$ - the background - may be denoted by $\mathbf{x}_b$ and a set of observations of the same parameter by $\mathbf{y}(i)$ with $i \in [1,..n]$. The observation vector $\mathbf{y}$ cannot be compared to the state vector (model state) $\mathbf{x}$ directly, but this can be done with a function called the *observation operator*, denoted by H, which is applied to the modelled field. This operator neglects observational or model errors and assumes that both state vector and ob-

servation are perfect. Discrepancies between the model state and the observations given by the vector of departures at the observation points $\mathbf{y}$-$H(\mathbf{x})$ are the key to data analysis. The differences are called 'innovation' if calculated with the background $\mathbf{x}_b$ or 'analysis residual' if calculated with the analysis state $\mathbf{x}_a$.

This analysis state $\mathbf{x}_a$ as provided by a Cressman analysis at each grid point j is calculated according to

$$\mathbf{x}_a(j) \;=\; \mathbf{x}_b(j) + \frac{\sum_{i=1}^n w(i,j)\left[\,\mathbf{y}(i) - H(\mathbf{x}_b(j))\,\right]}{\sum_{i=1}^n w(i,j)} \qquad (5.1)$$

$$\textbf{where}\quad w(i,j) \;=\; \max\left(0, \frac{R^2 - d_{i,j}^2}{R^2 + d_{i,j}^2}\right)$$

is a weighting function equal to $d_{i,j}$, the distance between grid points i and j. The weighting function $w(i,j)$ = 1 for co-located observations and grid points, i.e. $d_{i,j}^2$ = 0, decreases with increasing $d_{i,j}$ and is set to zero if $|d_{i,j}| > R$ where R is a user defined constant distance beyond which the observation has no weight.

The successive correction method (SCM)[1] is a more general variation of the Cressman analysis. In the SCM it is possible that the weight at a location where $i = j$ is less than one, so that a weighted average of background and observation is applied instead of replacing the model value by the observation. In this way, assimilations can be performed iteratively several times for a single time step, or the corrections can be distributed through several time steps for a more smooth progression. However, both methods are unsatisfactory, because it is possible to override a good background value with an erroneous observation thus producing a bad analysis. These methods do not clarify what to do if the observations are denser than the model grid points. Furthermore, the smoothness of fields and the relationships between variables are not guaranteed.

All sources of information comprising an assimilation system, i.e. observations, first guess, and known physical properties, are likely to be imperfect. Therefore, it is necessary to take the errors of observations and model estimates into account to formulate an optimal analysis system with minimal errors.

5.3   Optimal Interpolation

Another method for blending new observations with a background field is based on statistical estimation theory and called Optimal Interpolation (OI) (Lorenc, 1981; Hollingsworth and Lönnberg, 1986, and references therein). The basic idea is that the background and the observations provide two independent multivariate estimates for the model state, which can be combined to produce an

---

[1]The method of successive corrections is more recently known as observation nudging, which is basically the same.

improved estimate. The optimal estimate is a linear combination of the two estimates that provides a minimum error variance. This is usually referred to in statistical jargon as BLUE, the Best Linear Unbiased Estimator.

The uncertainties in the modelled state as well as in the observations can be considered by the modelling of errors.

- The background error, denoted by $\varepsilon_b = \mathbf{x}_b - \mathbf{x}_t$ with the average $\overline{\varepsilon_b}$ and covariance $\mathbf{B} = \overline{(\varepsilon_b - \overline{\varepsilon_b})(\varepsilon_b - \overline{\varepsilon_b})^{\mathrm{T}}}$ is the difference between the background state vector $\mathbf{x}_b$ and it's true value $\mathbf{x}_t$.

- The observation error $\varepsilon_o = \mathbf{y} - H(\mathbf{x}_t)$ with the average $\overline{\varepsilon_o}$ and covariance $\mathbf{R} = \overline{(\varepsilon_o - \overline{\varepsilon_o})(\varepsilon_o - \overline{\varepsilon_o})^{\mathrm{T}}}$ contains errors of the observation process, errors in the design of the operator H, and representativeness errors i.e. discretization errors which prevent $\mathbf{x}_t$ from being a perfect image of the true state.

- Finally, $\varepsilon_a = \mathbf{x}_a - \mathbf{x}_t$ is the estimation error of the analysis state $\mathbf{x}_a$ with the average $\overline{\varepsilon_a}$, which should be minimized. The error covariance of the analysis is denoted $\mathbf{A}$.

The OI is then defined by the following equations:

$$\mathbf{x}_a = \mathbf{x}_b + \mathbf{K}(\mathbf{y} - H[\mathbf{x}_b]) \tag{5.2}$$
$$\mathbf{K} = \mathbf{B}\mathbf{H}^{\mathrm{T}}(\mathbf{H}\mathbf{B}\mathbf{H}^{\mathrm{T}} + \mathbf{R})^{-1}$$

where the linear operator $\mathbf{K}$ is called the gain, or weight matrix, of the analysis and $\mathbf{H}$ is the linearized observation operator $\mathbf{H}(\mathbf{x} - \mathbf{x}_b) = H(\mathbf{x}) - H(\mathbf{x}_b)$ for any $\mathbf{x}$ close enough to $\mathbf{x}_b$. The fundamental hypothesis for OI states is that only a limited number of observations are important to determine the analysis increment (5.2) for each model variable. This means that only a small number p_i of observations are chosen with empirical selection criteria for a model variable $x(i)$. A corresponding list of p_i background departures $(\mathbf{y} - H[\mathbf{x}_b])_i$ is then picked and the p_i background error covariances between the model variable $x(i)$ and the model state interpolated at the observations points p_i (or in other words: the relevant p_i coefficients of the i-th line of $\mathbf{B}\mathbf{H}^{\mathrm{T}}$). Furthermore the $p_i \times p_i$ background and observation error covariance sub-matrices are formed by the restrictions of $\mathbf{H}\mathbf{B}\mathbf{H}^{\mathrm{T}}$ and $\mathbf{R}$. Now the $p_i \times p_i$ positive definite matrix formed by the restrictions of $(\mathbf{H}\mathbf{B}\mathbf{H}^{\mathrm{T}} + \mathbf{R})$ to the selected observations has to be inverted. Finally, this must be multiplied by the i-th line of $\mathbf{B}\mathbf{H}^{\mathrm{T}}$ to give the respective line of $\mathbf{K}$.

Further Methods

There are other, more complex assimilation algorithms used in numerical analysis and forecasting. However, these methods are computing-time intensive

and inappropriate for the purpose of this study, because they are used for retrospective analysis rather than real time assimilation. However, a brief description of some of the methods below shows the potential of possible future developments.

A method to overcome the least-squares problem and therefore the local data selection of the OI-technique is to solve a variational optimization problem by iteratively minimising a cost function J in the analysis. This is done, for example, for satellite data retrieval with a one-dimensional variational analysis (1D-Var) for a local investigation of a single atmospheric column. Usually, numerical weather analysis systems apply a three-dimensional variational analysis (3D-Var), because 3-D measurements of the state of the atmosphere are made for example with co-ordinated radio-soundings. For observations additionally distributed in time, 3D-Var can be generalized to a four-dimensional variational assimilation scheme (4D-Var), with the strong constraint that the model equations must solve the sequence of model states from the initial time onwards. This requires a "perfect" model and the implementation of an adjoint model to integrate the so-called tangent linear time-stepping operator M_i. This makes it difficult to realize.

For retrospective analysis the so-called Kalman Filter and it's extended version can be applied in sequential data assimilation. The result is the same as in 4D-Var if the model is perfect and both algorithms use the same data, but the Kalman Filter is defined through a sequence of 3-D analyses, instead of solving the 4-D problem globally. This technique is applied for re-analysis questions in non-real time applications.

5.4 Summary

The objective of data assimilation is to find the model state that agrees best with the observed data. This should not be mistaken as interpolation of observed data onto the model grid. The modelled values are mapped into the observation-data space for the assimilation procedure, because it is only possible to calculate model values for positions that lie between the model grid points rather than extrapolate measured data onto model grid points. The data used for the assimilation process in this work were derived from a satellite sensor (SSM/I) which provides the basis for a global data set of sea ice concentrations on a daily basis. Since both model and SSM/I data grids have a very similar spacing ($\sim$27 km), errors due to sparse data interpolation are low.

For this thesis Optimal Interpolation (OI) was chosen because it is simple to implement. A drawback of this method is that spurious noise can be introduced to the model by an analysis from different sets of observations and possibly dif-

ferent background errors. Since only one source of measured information is used in this study this effect can be neglected.

Chapter 6

Assimilation Experiments

In this chapter, two case studies of the assimilation procedure are presented for two expeditions to the Arctic. They demonstrate the performance of the numerical model as a forecast tool for sea ice conditions.

6.1 Description of the Assimilation Process

The sequence-of-operation diagram below shows how the model is run in assimilation mode and as a forecast tool. An un-assimilated model run based only on external atmospheric and oceanic forcing data is used as a background for the first assimilation step, when observations are available. After the assimilation procedure the model is run freely (only limited by the boundary conditions) until the next assimilation step. After the last assimilation step the model runs in forecast mode for up to ten days to predict sea ice conditions. Atmospheric forecast information is taken from ECMWF, which is available for up to ten days, although the forecast skill decreases from 95% for the first forecast day down to $\sim 40\%$ for the tenth forecast day (Järvinen, 1998). Assimilation steps can be included as often as observations are available (in case of SSM/I data, daily).
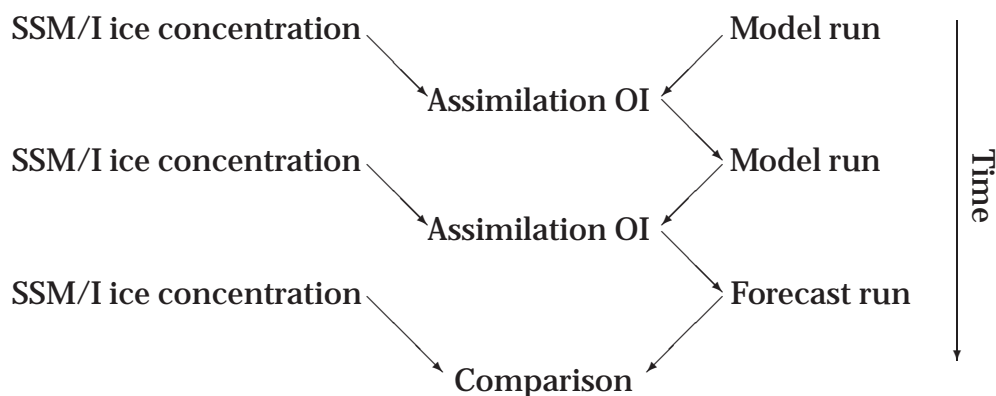
In the following examples up to five assimilation steps were performed for the simulations and the model was run freely afterwards.

Sea Ice Model Variables

In the numerical model sea ice concentration is treated as a prognostic variable. This means that the concentration at the previous time step is used to calculate concentration in the following time step. The same applies for the calculation of ice volume, from which the ice thickness is deduced by dividing the ice volume by the ice concentration. In contrast, ice drift is treated as a diagnostic variable because the acceleration term is rather small. The momentum balance is solved for each time step according only to oceanic and atmospheric drag, Coriolis force and the internal stress. Through advection, the assimilation of sea ice drift information derived, for example, from drifting buoys or SSM/I sequences into a sea ice model (Meier et al., 2000; Zhang et al., 2003) has an indirect influence on prognostic variables such as sea ice thickness.

The assimilation of sea ice concentration data into the model raises a problem: because sea ice volume is directly related to sea ice concentration the variation of the concentration field during the assimilation steps requires a corresponding variation of volume. In this study, it is assumed that the ice thickness remains constant during the assimilation step and that the sea ice volume changes with the assimilated sea ice concentration.

For the data gap of the SSM/I at the North Pole some *a-priori* information is needed in order to provide a complete field of sea ice concentration for the assimilation. For this study, the model results of the background field are used as pseudo-data. Therefore, the ice volume in these grid cells remains unchanged during the assimilation process.

6.2   Prediction Skills

The quality of a prediction is often characterized as a skill. In this study, the skill is defined as

$$\texttt{skill} = 1 - \frac{\frac{1}{n-1}\sum_{i=1}^{n}(\mathbf{x}_i(t) - \mathbf{y}_i(t))^2}{\frac{1}{n-1}\sum_{i=1}^{n}(\mathbf{y}_i(t))^2} \tag{6.1}$$

with n being the number of data points i, $\mathbf{x}$ the predicted and $\mathbf{y}$ the observed value at time t. Equation (6.1) deviates from the classical definition of explained variance in that the normalisation does not include subtraction of the mean value for the $\mathbf{x}$ and $\mathbf{y}$ fields. In this case $\mathbf{x}$ and $\mathbf{y}$ cover a dense geographical domain so that subtracting their means would give an arbitrary effect. The skill is the mean square error of $\mathbf{x}_i - \mathbf{y}_i$, normalized by $\sum \mathbf{y}_i^2$ for a given time t. Values for this skill vary between 0 and 1 where 0 means that the error of the predicted value is of the same order of magnitude as the reference and 1 means that the error is zero and so the prediction produces the reference values.

A confidence interval for the skill is defined as the standard deviation

$$\texttt{ci} = 1 - \sqrt{1 - \frac{\frac{1}{n-1}\sum_{i=1}^{n}(\mathbf{x}_i(t) - \mathbf{y}_i(t))^2}{\frac{1}{n-1}\sum_{i=1}^{n}(\mathbf{y}_i(t))^2}} \qquad (6.2)$$

which means that high values of skill have a small confidence interval and therefore a high accuracy. Lower values give a bigger confidence interval due to the fact that lower skill implies bigger errors.

6.3   ARCDEV

The Arctic Demonstration and Exploratory Voyage (ARCDEV) was carried out by the ARCDEV consortium which consists of European industry and research institutions in close co-operation with Russian institutions. All members are involved in Arctic shipping, logistics, exploration, technology and research. The objective of the project was a gas-oil transport under winter conditions from Sabeta, Russia (an experimental production site located on the Yamal Peninsula on the northwestern shore of the Ob Bay) to the port of Rotterdam, The Netherlands. The Finnish ice-strengthened motor tanker M/T UIKKU was accompanied by the Russian icebreaker KAPITAN DRANITSYN which served as a research vessel during the passage in April and May 1998. Because of the severe ice conditions in spring 1998, the convoy received additional assistance from the Russian nuclear icebreaker ROSSIYA in the Kara Sea and Ob Bay.

The time period of this cruise was chosen for an assimilation experiment because it is well documented. Therefore, there is enough data for both assimilation and validation. The cruise also serves as an application of a numerical sea ice forecast model (Lieser and Lemke, 2002). The simulation period starts in April 1998, initialized with restart values (from a climatological model run) for sea ice concentration and sea ice volume. This run is the background run for the assimilation experiment. SSM/I ice concentration data are assimilated into the numerical model every five days until 20 April 1998. After that day the model is run freely in forecast mode for a period of ten days.

Figure 6.1 shows sea ice concentration fields from (a) the model run without data assimilation forced with the M-E setup, (b) the assimilated model run with M-E forcing and (c) SSM/I data. Radar altimeter data are depicted as stripes overlaid on ice concentration fields. These data represent sea ice information derived from waveform analysis of the reflected radar pulse (T. Schöne, 2002, pers. comm.). The colour code of the stripes distinguishes between solid ground (with a given probability of sea ice) in grey and open water in white. This waveform analysis was carried out for a sub-region of the Arctic between $40\,^{\circ}$ W and

(a) Un-assimilated model run
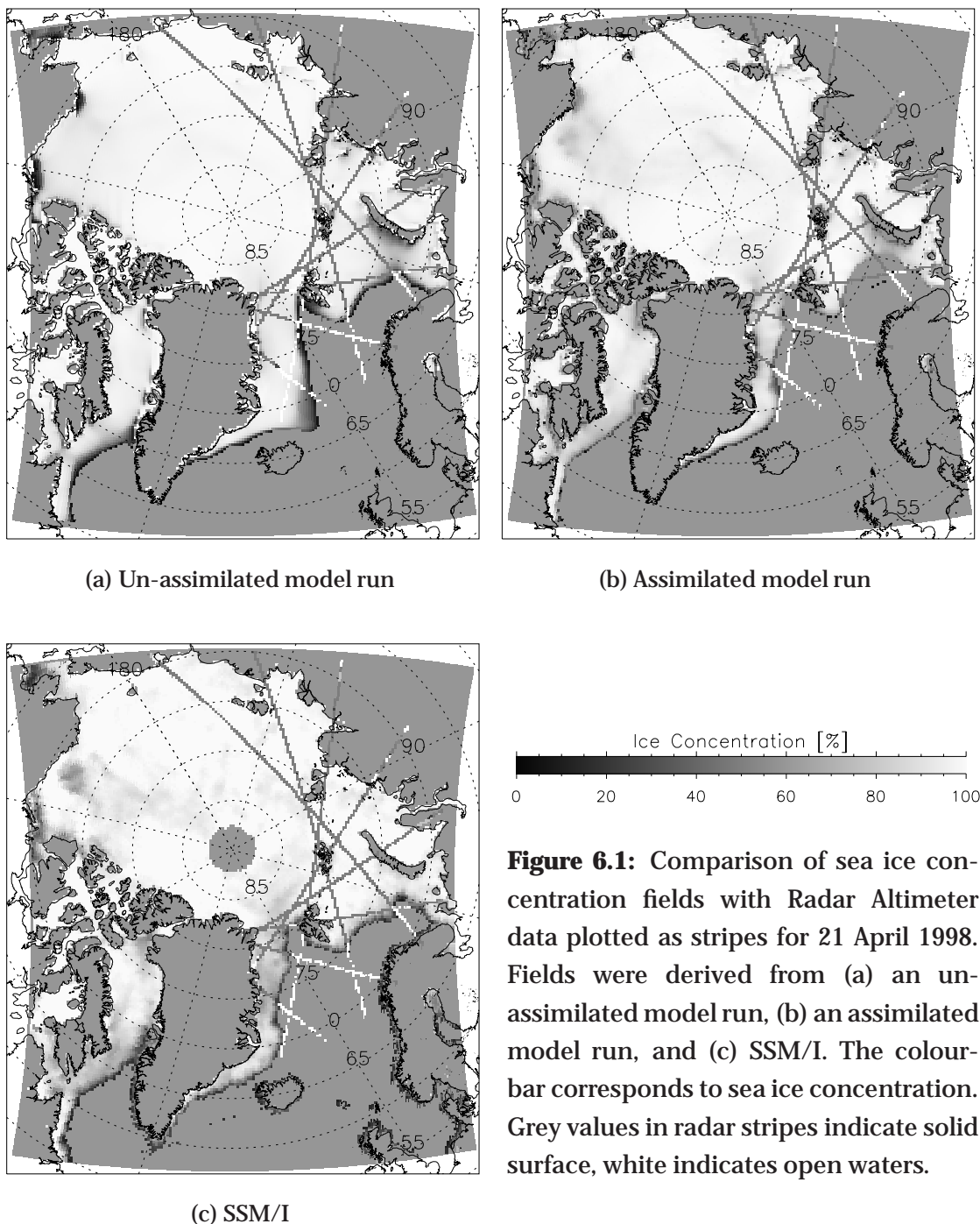

(b) Assimilated model run

(c) SSM/I

Figure 6.1: Comparison of sea ice concentration fields with Radar Altimeter data plotted as stripes for 21 April 1998. Fields were derived from (a) an un-assimilated model run, (b) an assimilated model run, and (c) SSM/I. The colourbar corresponds to sea ice concentration. Grey values in radar stripes indicate solid surface, white indicates open waters.

180° E. The data are used to validate the position of the sea ice edge in the Greenland and Barents Seas.

The stand alone (un-assimilated) model run overestimates sea ice concentration in the Greenland and Barents Seas as discussed in Chapter 4 for the years 1994 and 1995. For the assimilated model run improvements in the sea ice concentration fields in the Greenland Sea are most obvious where the RA data and the predicted sea ice edge agree well. Also, the ice edge northwest and south of Spitzbergen is reproduced well in this model run. However, sea ice concen-

trations in the eastern Barents Sea are underestimated. One reason for this discrepancy may be that the interplay of the interpolation weights with the boundary conditions seems to be less than optimal. The sea ice edge in the SSM/I data and open water indication in RA data agree with each other, partly because the passive microwave data were used for the validation of the radar signals.

The development of skill as defined in equation (6.1) is depicted in Figure 6.2 for ten days of a forecast run. The higher skill values of the assimilation experiment relative to the forecast without data assimilation clearly show the improvement which is a result of the data assimilation procedure. The numerical model with data assimilation reproduces sea ice conditions in very close agreement with the remote sensing data. The experiment without data assimilation shows lower skill values at a constant level throughout the forecast period. However, the skill for the assimilated model run decreases with time because the positive influence of the assimilated observation decreases with time. For the same reason, the standard deviation as defined in (6.2), also shown in Figure 6.2, increases with time. The modelled sea ice forecast is still dependent on the atmospheric forecast conditions, which are subject to increasing errors with time.
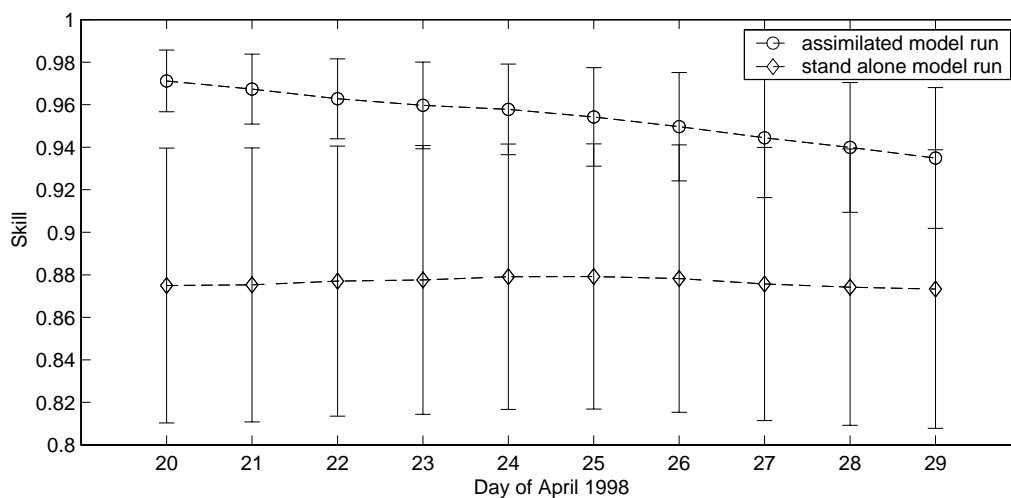

Figure 6.2: Skill of sea ice concentration model results and SSM/I data for an assimilated and a stand alone model run for the whole Arctic for late April 1998. Also shown are the standard deviations as defined in (6.2).

During the ARCDEV cruise, ice pilots aboard the Russian icebreakers suggested different routes through the Kara Sea *inter alia* on the basis of a satellite image received from Russian satellite Meteor 3/5 [1] on 28 April 1998. This image (Figure 6.3) covers an area in the central Kara Sea. The upper left part shows the northern tip of the island Novaya Zemlya. Bright values indicate snow cov-

---

[1]The satellite's tele-photometer operates at 0.5 - 0.7 μm and scans the surface with a swath width of $\sim$2600 km and a sub-satellite resolution of $\sim$3 km.
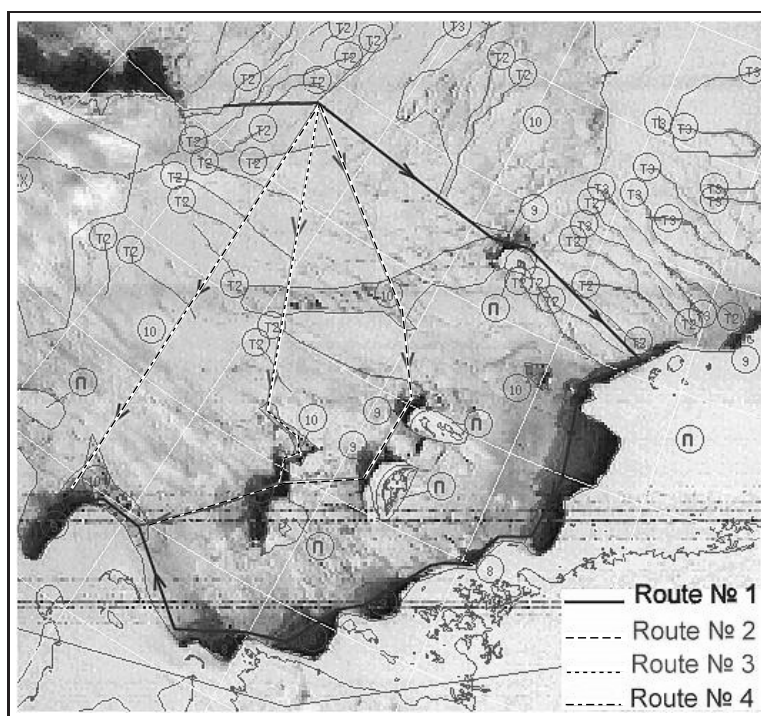
Figure 6.3: During ARCDEV four possible route alternatives from the northern tip of Novaya Zemlya to the Ob Bay were developed by AARI (Arctic and Antarctic Research Institute, Russia) ice pilots. The convoy followed Route No.1 making best use of the ice situation by going through leads and polynyas (image taken from http://arcdev.neste.com). `Data courtesy of AARI, image adapted.`

ered surfaces whereas dark values indicate open water. In the lower part, the ice edge is separated from the Russian coastline by a clearly visible coastal polynya. Ice cover between the shoreline and the open water is landfast sea ice. Four different routes were suggested from the current position (at that time north of Novaya Zemlya) to the Ob Bay (in the lower left corner of the image). Route No. 1 was chosen because it makes best use of cracks and openings in the sea ice and follows the most easily navigable track in the polynya at the fast ice edge. All other routes are of shorter distance but are more or less perpendicular to the prevailing drift and stress direction. The latter is indicated through the orientation of the numbered lines representing fractures in the sea ice cover.

For the date of the reception of the satellite image shown in Figure 6.3, sea ice concentrations predicted by the model and deduced from SSM/I data are shown in the upper and lower panel of Figure 6.4, respectively. The black rectangle in Figure 6.4 marks the position of the satellite image shown in Figure 6.3.

As can be seen from the upper panel of Figure 6.4 the predicted sea ice concentration compares well with the observations for the Kara Sea. The open water patches are at the same locations as in the satellite image. Along the northern tip of the island Novaya Zemlya the low ice concentration is shown by dark
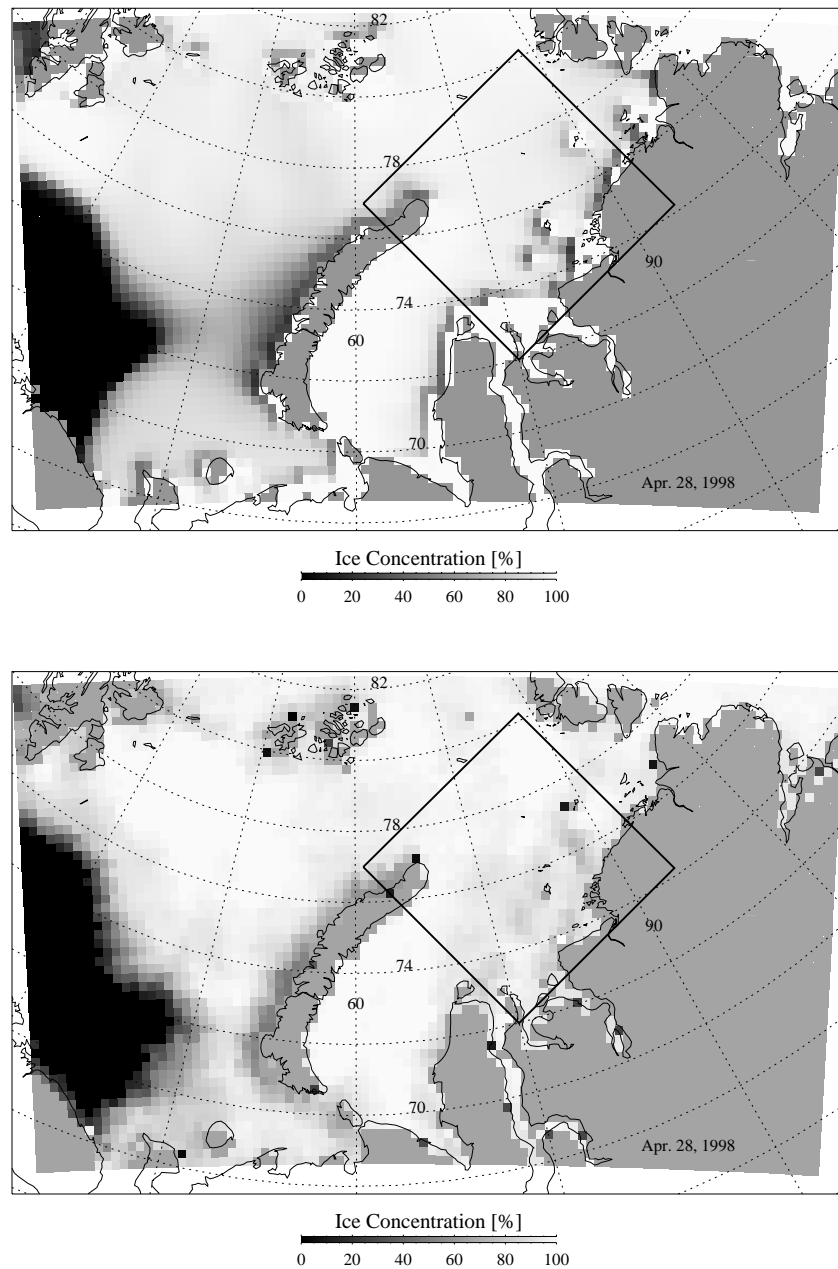
Figure 6.4: Result of a model forecast run for 28 April 1998 in the Kara Sea. The upper panel shows the calculated ice concentration. The lower panel shows the SSM/I data for comparison. The black rectangle indicates the location of the satellite image shown in Figure 6.3 provided by the Russian ice pilots.

grey values. The same is true for the region off the Siberian coast between the Taymyr and Yamal peninsulas and for the small off-shore islands. A fast ice edge is simulated and a polynya is visible with lower ice concentrations. Because of the low quality of the SSM/I data in coastal regions (Bennartz, 1999) the polynya areas are not as clearly visible in the data. However, slightly darker grey-values along the Siberian coast suggest lower ice concentration in this region. At the

western coast of Novaya Zemlya the polynya is wider and is consequently resolved in the SSM/I data.

The calculations of the numerical model have the advantage of reproducing the open water regions off the coastline. Information is lacking in these regions in the SSM/I data, possibly due to coastal interference within the signal. This can be taken into consideration during the assimilation process by setting the weights accordingly. Questionable observations can be given little weight, e.g. in coastal regions or in summer when the SSM/I tends to underestimate sea ice concentration owing to the presence of melt-ponds on the ice surface (Cavalieri et al., 2002). On the other hand, the fast ice parameterization may tend to overestimate the open water fraction in the model within single grid cells. However, observations and numerical simulations complement each other in the sense that the data assimilation technique is able to produce a best possible analysis of the real situation. The combination of the 'best of both worlds' is the great advantage and innovation of this technique for predicting sea ice conditions.
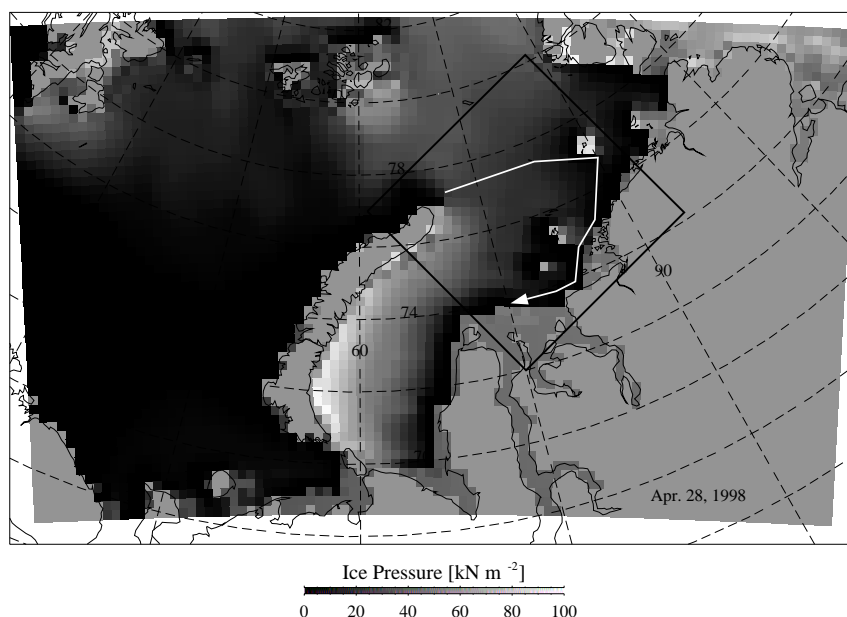

Ice Pressure [kN m^{-2}]

| 0 | 20 | 40 | 60 | 80 | 100 |

Figure 6.5: Horizontal ice pressure deduced from model results for 28 April 1998. The black rectangle indicates the location of the satellite image shown in Figure 6.3. The arrow shows the suggested Route No. 1 provided by the Russian ice pilots.

Further potential of using numerical model results for ship routing lies in the possibility of deducing other physical quantities from predicted parameters. In Figure 6.5 the horizontal ice pressure, which is a function of sea ice concentration, thickness and drift, is displayed for the area corresponding to the upper panel of Figure 6.4. The horizontal ice pressure is the force that a vertical unit area (e.g. at a ship's bow) would face in this region. From sea ice concentration

information alone (Figure 6.4) a routing suggestion is hard to make, as long as the model does not contain any information on leads or fractures in the sea ice. With the aid of deduced horizontal ice pressure fields, the suggested Route No. 1 from the Russian ice pilots (see Figure 6.3) is clearly supported (indicated by the arrow).

6.4   ARKTIS XVII/2

In August and September 2001 the German RV POLARSTERN, on cruise ARKTIS XVII/2, mainly followed the submarine geological rift system called the Gakkel Ridge in the central Arctic Ocean (Thiede et al., 2002). This scientific cruise operated in a sector from about $10°$ W to about $90°$ E up to the geographical North Pole. A cruise plot of this expedition is shown in Figure 6.6. The sea ice investigations included sea ice thickness measurements and other physical parameters that describe the sea ice conditions in the region of the so called Transpolar Drift. This drift-stream is part of the general surface circulation pattern in the Arctic Ocean which consists of two major components. One is the so-called Beauford Gyre, which rotates usually anticyclonically in the central part of the Arctic Ocean (covering mainly the Canada Basin and the Makarov Basin), the other component is characterized by a more or less straight drift that commences in the central Siberian shelf region, crosses the North Pole and continues through Fram Strait into the Greenland Sea.
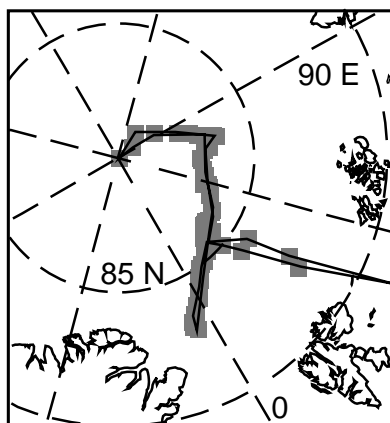
Figure 6.6: This figure shows the noon positions of R/V POLARSTERN cruise ARKTIS XVII/2 with respect to the grid-cells of the numerical model. The ship entered the Arctic Ocean from the Barents Sea, turned to the south-west (towards Greenland), turned back to north-east, made a transect to the geographical North Pole and took the same route back to the Barents Sea.

Sea Ice Thickness

Sea ice thickness was determined from measurements with an electro-magnetic induction system (EMI, for a detailed description refer to Haas et al., 1997) and hourly visual observations from the ship's bridge (Haas and Lieser, 2003). The visual observations were performed by a group of sea ice researchers on board

the vessel and describe the typical ice conditions around the ship at the turn of every hour. Although some uncertainties arose from different levels of experience of the observers, a general and quite representative overview of the summer ice situation in the Transpolar Drift in 2001 was obtained. When broken and vertically tilted sea ice floes passed a measuring stick, which was mounted on the side of the ship, their thickness was estimated. Other quantities (for example percentage coverage of sea ice) were visually estimated.

Figure 6.7 shows a comparison of sea ice thickness estimates from the different sources as a function of the day-of-year 2001 (with respect to the ship's geographical location shown in Figure 6.6). All values represent daily averages. The solid line is the modal sea ice thickness[2] inferred from EMI measurements. The dashed line is the average of all visual observations on that day. Modelled ice thickness for the grid cell of RV POLARSTERN's position with data assimilation is the line marked with "o", whereas the line marked with "x" is modelled ice thickness for the grid cell of RV POLARSTERN's position without data assimilation. At day 217 (05 August) the ship entered ice-covered waters with relatively thin ice cover and subsequently operated in heavier ice conditions with thicknesses of between 1.5 m and 2.5 m. As the ship was leaving the ice covered area again it crossed thinner ice in the marginal ice zone on days 270 and 271 in late September 2001.

The EMI measurements and visual observations were well correlated with a correlation coefficient of 0.75 (n=51). EMI measurements could not be performed every day, which results in gaps in the EMI curve. Both modelled ice thickness estimates show similar behaviour for the measurement period, although both the assimilated and the un-assimilated model runs tend to underestimate the sea ice thickness. However, the model run with ice concentration assimilation clearly shows the benefit gained from including the remote sensing information.

Both the EMI measurements and the visual observations reflect the ice thickness distribution on this cruise leg. Sea ice thickness increases rapidly while heading deeper into the pack ice and reaches the highest values around day 225 (13 August 2001) when the ship was close to the ice edge in the western-most region of the cruise. Here, the ice cover was heavily deformed as the ice passes into the Fram Strait region. Both the model run with data assimilation and without data assimilation predict the sea ice edge to be too far north, which results in the apparently thinner sea ice thickness values occurring where the observations show the thickest values. All along the cruise track the assimilated model run

---

[2]The modal ice thickness is the most frequent ice thickness representing the typical level ice thickness. In contrast, the mean ice thickness gives the mean measured thickness including rafted and deformed ice, which does not necessarily have the highest occurrence.
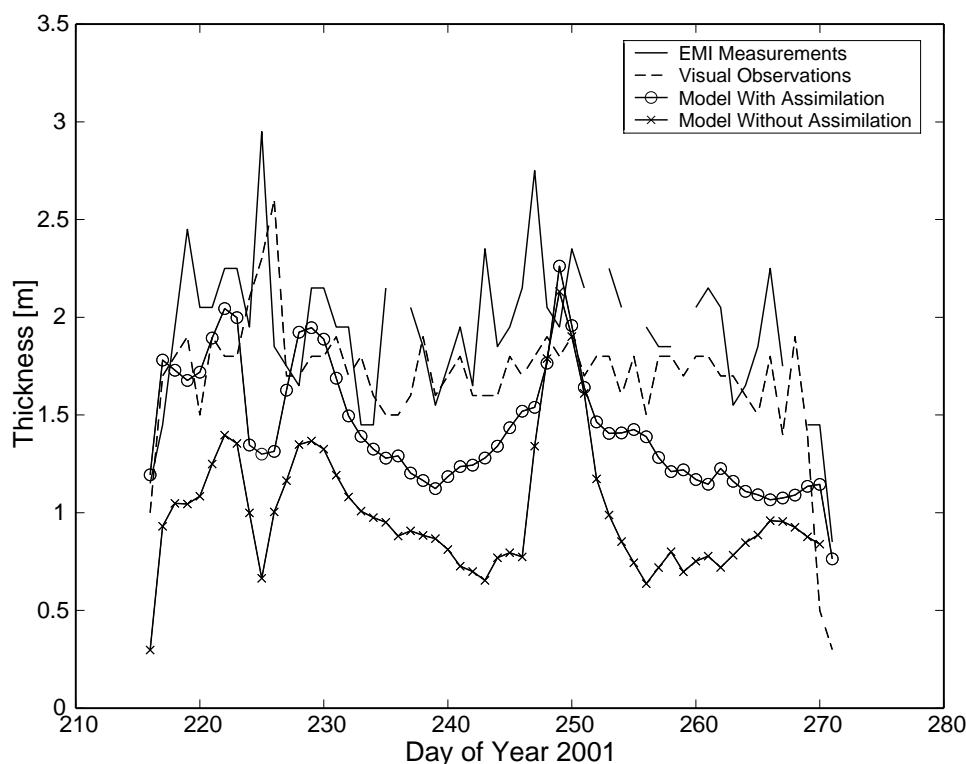
Figure 6.7: Comparison of the daily mean sea ice thickness estimates along the cruise track of RV POLARSTERN during the expedition ARKTIS XVII/2. The solid line shows measured EMI values, whereas the dashed line presents the visual observations. Lines with marks are model calculations with data assimilation (o) and without data assimilation (x). The ship entered the sea ice on day 217 (05 August 2001) and left it on day 271 (28 September 2001).

simulates the ice thickness closer to the observations than the un-assimilated run. However, the difference between measurements and simulation exceeds 25% at some locations. The second prominent peak in sea ice thickness was observed on the transect to the North Pole, which was reached at day 249 (6 September 2001). The model shows this peak for the North Pole location and the surrounding area, whereas the measurements of the thickest ice were made two days before. Both model runs (with and without data assimilation) agree in the simulation of this peak. This is not so surprising since the SSM/I data have the data gap at the North Pole and the estimates from the background run are used for the assimilation instead of real observations. On the last part of the cruise towards the sea ice edge the sea ice thickness decreases and the measurements and simulations agree within a very small range at the beginning of the freezing season in late September. This good reproduction of the fall season was already discussed in Chapter 4.

Sea Ice Drift

During the cruise, geophysical REFTEK-stations[3] were deployed on ice floes for the registration of seismic waves and position while drifting with the sea ice. In Figure 6.8 the position record-ings at twelve hour intervals are plotted as squares together with the simulated sea ice displacement (circles) from the assimilation ex-periment for a one week drifting period. The star marks the be-ginning of both tracks. Convert-ing the spherical coordinate scales ($\sim$0.2° latitude and $\sim$0.8° longi-tude) into geographical distances, it is apparent that the modelled sea ice drift agrees well with measured buoy positions. The longitudinal displacement is captured almost perfectly (0.1° longitude at 86° lat-itude is 77 m), only the value of the latitudinal displacement in the middle of the drift period is under-estimated, most probably due to low wind forcing. However, the du-ration and direction of the north-ward drift agrees well. The follow-ing southward shift is calculated with very high accuracy, although it leads to a final position which is located too far south because of an underestimation of $\sim$1km in the previous pole-ward drift. The mod-elled drift was calculated by inter-polation from the surrounding drift estimates at grid points for the ac-tual position. This sub-gridscale analysis of a Lagrangian trajectory shows that even such small-scale processes can be predicted by the model.
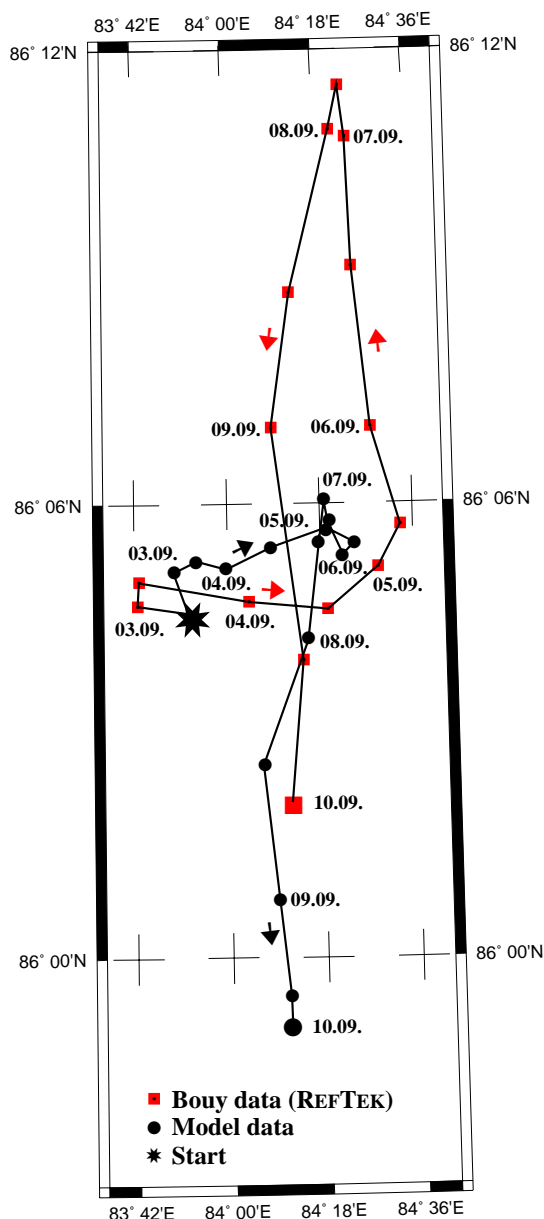

Figure 6.8: Twelve-hourly positions of a geo-physical REFTEK-Buoy deployed during ARK-TIS XVII/2 marked with squares. Corre-sponding modelled sea ice drift positions are marked with circles.

---

[3]Digital recording systems of seismic waves for stand-alone use manufactured by REFRACTION TECHNOLOGY

6.5 Summary

Two case studies of past Arctic Ocean expeditions demonstrate the use of the numerical sea ice model developed. The assimilation procedure improves the skill of prediction of sea ice conditions by about 10% for short term forecasts (5-10 days). However, the sea ice model is dependent on the accuracy of the atmospheric forcing provided by numerical weather prediction systems. A sea ice forecast is therefore limited by the quality of the atmospheric forecast in addition to the quality of the sea ice model.

For a winter cruise to the Kara Sea in 1998 ice concentration is predicted with a high accuracy of about 95% for a ten day forecast experiment. The sea ice concentration prediction is significantly improved at the sea ice edge with assimilation of SSM/I data, as seen from comparison with radar altimeter data. Ice concentrations deduced from different satellite sensors confirm the good prediction from the numerical model.

For a summer cruise to the central Arctic Ocean in 2001, sea ice thickness measurements are compared with results from model estimates. Here, the difficulties in reproducing (as discussed in Chapter 4) and predicting summer ice conditions can be seen. Ice thickness is underestimated by the model by up to 25% for some locations. This is a rather high value since ice breaking / ramming capabilities of ships can be over-strained at around 1.5 m ice thickness, so that with mean ice thickness between 1.5 m and 2 m this overestimation may be critical. Even though sea ice shows a delayed reaction to changing forcing conditions, best possible forcing is essential to estimate not only sea ice drift, but also sea ice concentration, thickness and, most important, the ice pressure. The track of a drifting buoy was predicted for a ten day period, giving a too southerly final position because of an under-estimation of a previous northward wind-driven displacement.

Chapter 7

Conclusions and Outlook

This work presents detailed regional and short term investigations of sea ice conditions simulated with a numerical, dynamic-thermodynamic sea ice model. In contrast, other studies carried out with previous versions of the model concentrated on seasonal and annual means, demonstrating the good performance of the model in climate system applications. Here, a new option was introduced by utilizing the model for short term sea ice prediction.

7.1   Summary and Discussion

The model presented here is based on previous studies carried out as described in Chapter 2. Model development consisted of increasing the horizontal resolution from a $\sim 110{\times}110$ km grid to $\sim 27{\times}27$ km point spacing for the Arctic domain. This permits a more realistic representation of the sea ice cover especially at geographic locations where the coarser resolution is unable to resolve narrow straits or small islands. With the new grid and a new corresponding bottom topography the Kara Gate (which separates the Barents Sea from the Kara Sea at the southern end of Novaya Zemlya) and the Vilkitsky Strait (a small passage between the Kara Sea and the Laptev Sea at the southern end of Severnaya Zemlya) are resolved with 6 and 10 grid points, respectively. This allows the simulation of sea ice in these key locations of the Northern Sea Route. Furthermore, a new ocean boundary condition was implemented which is appropriate for the new horizontal resolution and now includes a seasonal cycle with better representation of the ocean currents and improved ocean heat flux. The simulations of the winter season 1994-1995 and the following summer proved that the model is able to reproduce observed sea ice concentrations. To test the new boundary conditions the old and the new ocean forcing was combined with atmospheric forcing derived from NCEP and ECMWF. Both atmospheric data sets have been shown to be of sufficient quality to force the sea ice model in climato-

logical investigations. However, ECMWF winds show a more realistic behaviour as presented in a study by Curry et al. (2002), and model results obtained in this thesis from runs driven with ECMWF data compared better with observations. The reproduction of sea ice conditions for years with anomalous ocean conditions remains difficult, since only a mean seasonal cycle of ocean heat flux and currents is installed. Nevertheless, the simulation for 1995, when an ocean heat flux anomaly propagated from the North Atlantic into the Nordic Seas, showed reasonable results, for example, in the Barents Sea.

Since the intended application and main focus of this study is the short-term prediction of sea ice, the best possible analysis of the sea ice situation is essential as a starting point for a prediction. To achieve this aim, a system for introducing remote sensing information derived from SSM/I to the model by data assimilation was developed. SSM/I data are suitable for this purpose, because they are of well-known quality with the exception of the melting season. The whole Arctic Ocean is covered daily and therefore sea ice concentrations can be provided for the model regularly and in near-real time. Their horizontal resolution is very similar to the new grid spacing of the numerical model used in this study.

Inter-annual ocean variability is of less importance on short time scales (5-10 days), because the ocean reacts much more slowly to changing boundary conditions than sea ice. If the model is run in forecast mode with data assimilation, part of the inter-annual ocean information is already included indirectly in the sea ice concentration data. Sea ice dynamics, i.e. sea ice drift, react fast in response to rapidly changing atmospheric drag, for example from low pressure systems, whereas sea ice thermodynamics, i.e. melting and growth, react on longer time scales. A slowly propagating ocean heat anomaly affects both the sea ice thickness and the sea ice edge. If the observed sea ice edge is located at a different position, then the assimilation procedure corrects the sea ice edge in the analysis. This indirectly introduces information about ocean conditions into the model. This can cause problems, when a coupled sea ice-ocean model is used. A changing sea ice concentration field must be consistent with a change of other parameters of the model system. In this study, the sea ice volume is adapted to changing sea ice concentration - assuming sea ice thickness to be constant. Numerically, a new sea ice mask, describing which grid cell has sea ice cover, is given to the model. This determines the ocean surface temperature, since the ocean surface covered by sea ice is at freezing temperature, and therefore the heat content of the mixed layer. In a coupled sea ice-ocean simulation a modified sea ice concentration induces artificial fresh water and salinity fluxes to the ocean, an issue that has to be dealt with carefully. Applying a different assimilation technique Lisæter et al. (2003) assimilate sea ice concentra-

tion data into a coupled sea ice-ocean model and introduce large temperature and salinity updates into the ocean. The authors used a retrospective filtering method for a climatological study. However, the coupled system requires thorough consideration of fresh water and heat fluxes in order not to destabilize the water column and trigger spurious convection during the assimilation. For short-term sea ice forecasting a computationally fast stand-alone sea ice model is quite sufficient.

Using the Optimal Interpolation technique, satellite sea ice concentration data are assimilated into the numerical model. This increases the explained variance between model prediction and observation considerably as shown in a forecast application test study for the ARCDEV expedition. For the Kara Sea the sea ice concentration and the location of open water patches, in this case a major polynya off the Siberian coast, is predicted with high accuracy. From such numerical predictions, information on sea ice conditions such as horizontal ice pressure fields can be derived. The horizontal ice pressure describes the force that a vertical unit area would face. This could be a ship's bow trying to steam through an ice covered region.

For summer 2001, a different case study revealed difficulties in predicting sea ice thickness and drift. The sea ice edge was predicted to be too far north and therefore the sea ice thickness shows discrepancies with observations. The comparison of a buoy track with results from numerical calculations demonstrates the dependence of forecast results on the availability of optimal forcing parameters. The skill of a model can not be better than the skill of its forcing data.

Applying the best possible analysis of sea ice concentration and the optimal forcing conditions in the numerical model, a forecast of sea ice conditions for 5-10 days produces realistic results. This study shows that the model simulates reasonable sea ice conditions with seasonal oceanic and daily atmospheric forcing and a fast ice parametrization. However, data assimilation techniques require careful consideration of connected physical parameters. Presently, concentration is the most accessible sea ice parameter, since it can be monitored from remote platforms, i.e. satellites. Improved algorithms allow for a realistic estimation of sea ice concentration from passive microwave sensors. However, the sea ice edge and ice coverage are dependent on the oceanic and atmospheric conditions and, therefore, related to fresh water and salinity fluxes in the ocean and the radiation budget of the atmosphere. The feedback mechanisms and results are easier to consider in a stand-alone model than in coupled simulations.

7.2 Future Objectives

The numerical sea ice model has proved to be realistic on climatological time scales as well as on shorter time scales. Wang et al. (2003) summarized the recent advances in numerical sea ice modelling. For the model used in this study some suggestions for improvements are briefly outlined as follows.

Tides

The sea ice cover of the Arctic Ocean is modified not only by thermodynamic growth/melt or dynamic movement by the prevailing wind and ocean currents but also on shorter time and smaller regional scales by tides (Kowalik and Proshutinsky, 1994). As a guidance tool for shipping transport through ice-covered areas the numerical model should also be able to account, for example, for opening and closing of leads caused by periodic divergence and convergence due to tides. These periodic changes were reported by the early northern travellers like Nansen (1902) and are of course still observed when sailing through the Arctic Ocean. On the one hand these leads play a role for ice formation when open water is exposed to the colder atmosphere and recently formed ice is transported to the downwind side of the lead/opening. On the other hand the leads are important for the transfer of energy and matter between the ocean and the atmosphere. The most prominent tides are the semi-diurnal tides, commonly denoted M_2 and S_2, with amplitudes generally dominating the tidal constituents. But the diurnal constituents of tides, denoted K_1 and O_1, seem to be even more important in the Arctic basin as Kowalik and Proshutinsky (1993) showed with their numerical model. The interaction of wind, ocean currents and tidally-induced, periodic and residual motion has a strong influence on the sea ice cover in coastal regions. The Western New Siberian Polynya (see Section 2.1.5) is one of the prominent features caused by the interplay of the three motions. Primarily offshore winds move the pack ice into the open sea, relatively warm water is upwelled on the continental slope and due to tidal mixing heat is transferred to the surface and released to the atmosphere. Finally, residual tidal ice drift and southerly winds transport the newly formed ice from the continental slope, keeping the polynya open.

Observations made during an expedition with the German RV POLARSTERN in 2001 show the different influences of wind and ocean currents (including tides) as shown in Figure 7.1. The data were collected with a geophysical REFTEK-station deployed on the sea ice for the registration of marine reflection/refraction seismic waves for 41 hours. At the beginning, the freely drifting station was pushed by wind and ocean currents generally to the southeast, but on the following day with very calm winds the pattern is mainly caused by tidal

81

and/or inertial currents. Here it is hard to distinguish between tidal and inertial influence on the resulting motion, because the critical latitude[1] for the principal solar tidal mode S_2 is at 85.75 ° and for the principal semi-diurnal lunar tidal mode M_2 74.46 ° (Pereira, 2001). However, tidally induced movement can cause convergent and divergent sea ice conditions very easily and result in almost closed loops of drift motion. Increasing wind speed at the end of the recording time results in a more translatory movement again. Similar drift patterns have been observed many times during different cruises and even the ships manoeuverability was hampered sometimes for some hours due to convergent sea ice conditions despite low wind speeds.
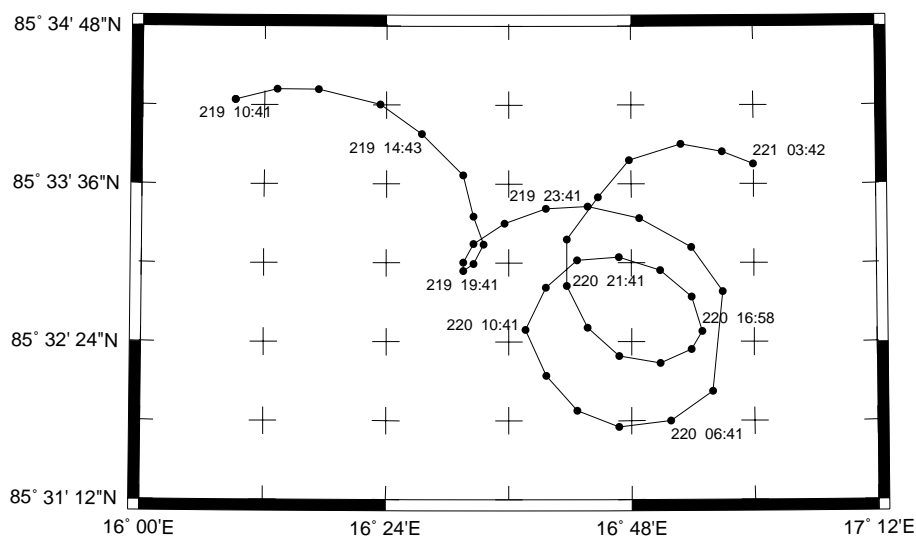

Figure 7.1: Drift of a REFTEK station deployed on sea ice during RV POLARSTERN cruise ARKTIS XVII/2 in summer 2001 for 41 hours. The drift starts at day 219 (07 August 2001) at 10:41 h and ends at day 221 (09 August 2001) at 03:42 h. The dots mark hourly position recordings.

Pressure Ridges

Sea ice roughness is an observable quantity for characterizing the sea ice state. This roughness reflects the sum of deformation energy acting on the sea ice. It is visible in pressure ridges that can form quite uniformly along floe edges and can extend for long distances (several 100 m). But roughness is also visible in heavily deformed ice which may be called a rubble field. Pressure ridges form when ice floes collide. Barriers formed in this way within a closed ice pack present a significant obstruction for ships manoeuvrability. It would be very helpful to predict the occurrence of such obstacles - not only in frequency on certain re-

---

[1]The critical latitude is the latitude at which the tidal frequency equals the Coriolis frequency and is of equal magnitude in both hemispheres.

gional scales but also the height (shape) of the ridges, giving a rough assessment of whether it might break under the repeated ramming of a ship. These dynamically built pressure ridges and also fractures and leads caused by divergent drift are referred to as linear kinematic features. Both the convergent drift and ridge formation and the opening of fractures could be predicted by the model. In this model set-up sea ice is treated as an Eulerian continuum on a relatively large scale. Hibler III. (2001) successfully tested the ability of a modified Coulombic rheology utilized with a similar numerical model as the one presented here to compute oriented lead and fracture patterns. To treat linear kinematic features in the model it may also appear advisable to change to a discontinuous Lagrangian approach and explicitly model individual ice parcels and the interaction between them, as in Hopkins and Thorndike (2002).

Discharge from Arctic Rivers

The fresh water budget of the Arctic Ocean has been studied for a long time by numerous authors (for example Prange, 2003). All agree on the importance of the Arctic Ocean for the fresh water balance in the adjacent seas. In the Arctic Ocean sources of fresh water are not limited to precipitation and melting sea ice; it is also introduced by rivers discharging into the basin. The biggest rivers are for example the Yenisey with an annual mean discharge of about 570 km^3, the Lena with an annual mean discharge of about 520 km^3, and the Ob with an annual mean discharge of about 395 km^3 running off the Russian Arctic coast. The Mackenzie (about 290 km^3 annual mean runoff) is another major contributor of fresh water from the Canadian Arctic. But there are many more rivers discharging between 30 km^3 and 150 km^3 per year. During the melt season the river water influences the fast ice areas. The relatively warm river water accelerates the breakup of the landfast ice and sometimes causes flooding of the sea ice (Bareiss et al., 1999). On the other hand, low salinity water has a higher freezing temperature which leads to earlier ice formation compared to saline sea water. Arctic run-off is expected to increase in the future due to climate change (Miller and Russel, 1995) so that the role of Arctic fresh water will be of even greater importance.

The rivers also carry sediments with them. This can be incorporated into the sea ice during the freeze-up season. Sediments are also incorporated into sea ice in the shelf areas due to turbulent mixing of the water column. This sediment in turn modifies the spectral albedo of the sea ice which can then absorb more energy during sunlight hours. Again, this results in an accelerated melting, but not necessarily in the same places where the sediment was incorporated (Kolatschek, 1998).

Fast Ice

The fast ice representation in the numerical model needs to be improved. It is of crucial interest not only for offshore activities in the oil industry but also for transport organizations and shipping companies for decision making on route planning. The time of fast ice breakup in spring or formation in autumn may limit the potential time for ship-based transport through narrow straits and passages. As was indicated by Wang et al. (2003) this issue is one of the hot topics in recent numerical sea ice-ocean models as well as the other problems mentioned above. The one-dimensional thermodynamic sea ice model which was applied by Bareiss (2002) to describe the evolution and behaviour of landfast ice in the Siberian Arctic could be implemented together with the introduction of river run-off described in the previous section.

Fast Ice

Bibliography

Aagaard, K. and R. Woodgate, 2001: Some thoughts on the freezing and melting of sea ice and their effects on the ocean, *Ocean Modelling*, **3**, 127–135.

Armstrong, T., 1985: Arctic policy concerns of the Year 2000: Global & Soviet policy concerns, in *Arctic Ocean Engineering for the 21st Century*, B. Gerwick, ed., Marine Technology Society, Washington, D.C.

Bareiss, J., 2002: *Süßwassereintrag und Festeis im der ostsibirischen Arktis - Ergebnisse aus Boden- und Satellitenbeobachtungen sowie Sensitivitätsstudien mit einem thermodynamischen Festeismodell*, Ph.D. thesis, Universtiät Trier, Trier, Germany, published by Alfred Wegener Institute: Berichte zur Polar- und Meeresforschung, **442**, 2003.

Bareiss, J., H. Eicken, A. Helbig and T. Martin, 1999: Impact of river discharge and regional climatology on the decay of sea ice in the Laptev Sea during spring and early summer, *Arctic, Antarctic and Alpine Research*, **31** (3), 214–229.

Bennartz, R., 1999: On the use of SSM/I measurements in costal regions, *Journal of Atmospheric and Oceanic Technology*, **16**, 417 – 439.

Bergthorsson, P. and B. Döös, 1955: Numerical weather map analysis, *Tellus*, **7**.

Bouttier, F. and P. Courtier, 1999: Data assimilation concepts and methods, Internal Report from ECMWF (unpublished).

Brauch, J. P., 2003: *Multidecadal and NAO related variability in a numerical model of the North Atlantic circulation*, Ph.D. thesis, Universität Bremen, Bremen, Germany, published by Alfred Wegener Institute: Berichte zur Polar- und Meeresforschung, **478**, 2004.

Carmack, E. C. and T. D. Foster, 1975: On the flow of water out of the Weddell Sea, *Deep Sea Research*, **22**, 711–724.

Cavalieri, D., C. Parkinson, P. Gloerson and H. Zwally, 2002: Sea ice concentrations from Nimbus-7 SMMR and DMSP SSM/I Passive Microwave Data, Tech. rep., National Snow and Ice Data Center, Boulder, CO.

Comiso, J., 1995: SSM/I ice concentrations using Bootstrap algorithm, NASA Report 1380, National Aeronautics and Space Agency.

Comiso, J., D. Cavalieri, C. Parkinson and P. Gloersen, 1997: Passive microwave algorithms for sea ice concentration: A comparison of two techniques, *Remote Sensing Environment*, **60**, 357–384.

Cressman, G., 1959: An operational objective analysis system, *Monthly Weather Review*, **87** (10), 367–374.

Curry, J., A. Schramm, R. Reeder, T. Arbetter and P. Guest, 2002: Evaluation of the data sets used to force sea ice models in the Arctic Ocean, *Journal of Geophysical Research*, **107** (C10).

Daley, R., 1991: *Atmospheric data analysis*, Cambridge atmospheric and space science series, Cambridge University Press.

Dokken, S., B. Håkansson and J. Askne, 2000: Inter-comparison of Arctic sea ice concentration using RADARSAT, ERS, SSM/I and *in-situ* data, *Candian Journal of Remote Sensing*, **26** (6), 521–536.

Elachi, C., 1988: *Spaceborne radar remote sensing: Applications and techniques*, IEEE Press, The Institute of Electrical and Electronics Engineers Inc., New York.

Ezraty, R. and A. Cavanié, 1999: Intercomparison of backscatter maps over Arctic sea ice from NSCAT and the ERS scatterometer, *Journal of Geophysical Research*, **104** (C5), 11471–11483.

Faddejew, D. and W. Faddejewa, 1973: *Numerische Methoden der linearen Algebra*, R. Oldenbourg Verlag, Muenchen (D), Wien (A).

Fischer, H., 1995: *Vergleichende Untersuchungen eines optimierten dynamisch-thermodynamischen Meereismodells mit Beobachtungen im Weddelmeer*, Ph.D. thesis, Universität Bremen, Bremen, Germany, published by Alfred Wegener Institute: Berichte zur Polarforschung, **166**, 1995.

Folland, C. K., T. R. Karl, J. R. Christy, R. A. Clarke, G. V. Gruza, J. Jouzel, M. E. Mann, J. Oerlemans, M. J. Salinger and S.-W. Wang, 2001: Observed climate variability and change, in *Climate Change 2001: The Scientific Basis. Contribution of Working Group I to the Third Assessment Report of the Intergovernmental Panel on Climate Change*, J. Houghton, Y. Ding, D. Griggs, M. Noguer, P. van der Linden, X. Dai, K. Maskell and C. Johnson, eds., pp. 99–181, Cambridge University Press, Cambridge, UK and New York, NY, USA.

Gerdes, R., M. Karcher, F. Kauker and C. Köberle, 2001: Predicting the spread of radioactive substances from the *Kursk*, *Eos, Transactions*, **82** (23).

Ghil, M., 1989: Meteorological data assimilation for oceanographers. Part I: Description and theoretical framework, *Dynamics of Atmospheres and Oceans*, **13**, 171–218.

Gilchrist, B. and G. Cressman, 1954: An experiment in objective analysis, *Tellus*, **6**, 309–318.

Gordon, A. L., 1986: Interocean exchange of thermocline waters, *Journal of Geophysical Research*, **91**, 5037–5046.

Haas, C., S. Gerland, H. Eicken and H. Miller, 1997: Comparison of sea-ice thickness measurements under summer and winter conditions in the Arctic using a small electromagnetic induction device, *Geophysics*, **62** (3), 749–757.

Haas, C. and J. Lieser, 2003: Sea ice conditions in the Transpolar Drift in August/September 2001: Observations during POLARSTERN cruise ARKTIS 17/2, Reports on Polar and Marine Research 441, Alfred Wegener Institute for Polar and Marine Research.

Haas, C., D. Thomas and J. Bareiss, 2001: Surface properties and processes of perennial Antarctic sea ice in summer, *Journal of Glaciology*, **47** (159), 613–625.

Harder, M., 1996: *Dynamik, Rauhigkeit und Alter des Meereises in der Arktis - Numerische Untersuchungen mit einem großkaligen Modell*, Ph.D. thesis, Universität Bremen, Bremen, Germany, published by Alfred Wegener Institute: Berichte zur Polarforschung, **203**, 1996.

Hibler III., W., 1979: A dynamic thermodynamic sea ice model, *Journal of Physical Oceanography*, **9** (4).

Hibler III., W. D., 2001: Modeling the formation and evolution of oriented fractures in sea ice, *Annals of Glaciology*, **33**, 157–164.

Hilmer, M., 1997. Numerische Untersuchungen des Einflusses atmosphärischer Antriebsfelder in Simulationen der Grenzfläche Atmosphäre-Eis-Ozean in der Arktis. Diploma thesis, Christian-Albrechts-Universität, Kiel, Germany.

Hilmer, M., 2001: *A model study of Arctic sea ice variability*, Ph.D. thesis, Christian-Albrechts-Universität, Kiel, Germany.

Hollinger, J., R. Lo, G. Poe, R. Savage and J. Peirce, 1987: *Special Sensor Microwave/Imager Users' Guide*, Naval Research Laboratory, Washington, D. C.

Hollingsworth, A. and P. Lönnberg, 1986: The statistical structure of short-range forecast errors as determined from radiosonde data. Part I: the wind field, *Tellus*, **38A**, 111 – 136.

Hopkins, M. A. and A. S. Thorndike, 2002: Linear kinematic features in Arctic sea ice, in *Ice in the Environment*, Proceedings of the 16th International Symosium on Ice, Dunedin, New Zealand, 2-6 Dec. 2002.

Jakobsson, M., R. Macnab and Members of the Editorial Board, 2001: International Bathymetric Chart of the Arctic Ocean, Technical reference and user's guide, Tech. rep., NOAA/NGDC & WDC for MGG, Boulder, CO.

Järvinen, H., 1998: Observations and diagnostic tools for data assimilation, Internal Report from ECMWF (unpublished).

Kaleschke, L., G. Heygster, C. Lüpkes, A. Bochert, J. Hartmann, J. Haarpainter and T. Vihma, 2001: SSM/I sea ice remote sensing for mesoscale ocean-atmoshere interaction analysis, *Canadian Journal of Remote Sensing*, **27** (5), 526–536.

Karcher, M., R. Gerdes, F. Kauker and C. Köberle, 2003: Arctic warming: Evolution and spreading of the 1990s warm event in the Nordic seas and the Arctic Ocean, *Journal of Geophysical Research*, **108** (C2), 3034, doi:10.1029/2001JC001265.

Kauker, F., R. Gerdes, M. Karcher, C. Köberle and J. Lieser, 2003: Variability of Arctic and North Atlantic sea ice: A combined analysis of model results and observations from 1978 to 2001, *Journal of Geophysical Research*, **108** (C6), 3182, doi:10.1029/2002JC001573.

Kern, S., 2001: *A new algorithm to retrieve the sea ice concentration using weather-corrected 85GHz SSM/I measurements*, Ph.D. thesis, Universität Bremen, Bremen, Germany.

Kolatschek, J., 1998: *Meereisdynamik und Sedimenttransport in der Arktis: Ergebnisse aus Feldstudien, Fernerkundung und Modellierung*, Ph.D. thesis, Universität Bremen, Bremen, Germany.

König-Langlo, G. and E. Augstein, 1994: Parameterization of the downward long-wave radiation at the Earth's surface in polar regions, *Meteorol. Zeitschrift*, **N.F. 3** (H. 6).

Kowalik, Z. and A. Proshutinsky, 1993: Diurnal tides in the Arctic Ocean, *Journal of Geophysical Research*, **98** (C9), 16449–16468.

Kowalik, Z. and A. Proshutinsky, 1994: The Arctic Ocean tides, in *The Polar Oceans and their role in shaping the global environment*, O. Johannessen, R. Muench and J. Overland, eds., Geophysical Monograph 85, American Geophysical Union.

Kreyscher, M., 1998: *Dynamik des arktischen Meereises - Validierung verschiedener Rheologieansätze für die Anwendung in Klimamodellen*, Ph.D. thesis, Universität Bremen, Bremen, Germany, published by Alfred Wegener Institute: Berichte zur Polarforschung, **291**, 1998.

Kreyscher, M., M. Harder, P. Lemke and G. Flato, 2000: Results of the Sea Ice Model Intercomparison Porject: Evaluation of sea ice rheology schemes for use in climate simulations, *Journal of Geophysical Research*, **105** (C 5), 11299 – 11320.

Laevastu, T., 1960: Factors affecting the temperature of the surface layer of the sea, *Comment. Phys. Math.*, **25** (1).

Lemke, P., 1987: A coupled one-dimensional sea ice-ocean model, *Journal of Geophysical Research*, **92** (C12), 13164–13172.

Lemke, P., W. Hibler III, G. Flato, M. Harder and M. Kreyscher, 1997: On the improvement of sea-ice models for climate simulations: the Sea Ice Intercomparison Project, *Annals of Glaciology*, **25**, 183 – 187.

Lieser, J. and P. Lemke, 2002: A sea ice forecast model for the Arctic Ocean, in *Ice in the Environment*, Proceedings of the 16th International Symposium on Ice, Dunedin, New Zealand, 2-6 Dec. 2002.

Lisæter, K. A., J. Rosanova and G. Evensen, 2003: Assimilation of ice concentration in a coupled ice-ocean model, using the Ensemble Kalman filter, *Ocean Dynamics*, **53** (4), 368–388, doi: 10.1007/s10236-003-0049-4.

Llorente, I. M., M. Prieto-Matías and B. Diskin, 2000: An efficient parallel multigrid solver for 3-D convection-dominated problems, Tech. rep., Institute for Computer Applications in Science and Engineering, NASA Langley Research Center, Hampton, VA.

Lorenc, A., 1981: A global three-dimensional multivariate statistical interpolation scheme, *Monthly Weather Review*, **109**, 701–721.

Massom, R., 1991: *Satellite remote sensing of polar regions : applications, limitations and data availability*, Belhaven Press, London.

McPhee, M., 1979: The effect of the oceanic boundary layer on the mean drift of pack ice: Application of a simple model, *Journal Physical Oceanography*, **9**, 388–400.

Meier, W., J. Maslanik and C. Fowler, 2000: Error anaysis and assimilation of remotely sensed ice motion within an Arctic sea ice model, *Geophysical Research Letters*, **105** (C2), 3339 – 3356.

Mesinger, F. and A. Arakawa, 1976: *Numerical Methods used in atmospheric models*, GARP Publications Series No. 17, Global Atmospheric Research Programme (GARP) WMO-ICSU Joint Organizing Committee.

Mikhailichenko, V., V. Peresypkin and L. Tsoy, 1999: Experimental voyage of tanker *Uikku* - Demonstration of the reliability of the year round navigation in the western area of the Arctic with the help of Russian icebreakers, in *POAC'99*, pp. 1039–1050, Proceedings of the 15th Int. Conf. on Port and Ocean Engineering Under Arctic Conditions, Espoo, Finland, August 23-27, 1999, Helsinki Univ. of Techn., Ship Laboratory.

Miller, J. R. and G. L. Russel, 1995: Climate change and the Arctic hydrological cycle as calculated by a global coupled atmosphere-ocean model, *Annals of Glaciology*, **21**, 91–95.

Nansen, F., 1902: The oceanography of the north polar basin, in *The Norwegian North Polar Expedition, 1893-1896, Scientific Results*, F. Nansen, ed., vol. 3, Longmans, Green and Co.

Nicolaus, M., C. Haas and J. Bareiss, 2003: Observations of superimposed ice formation at melt-onset on fast ice on Kongsfjorden, Svalbard, *Physics and Chemistry of the Earth*, **28**, 1241–1248.

Nørgaard-Pedersen, N., R. F. Spielhagen, J. Thiede and H. Kassens, 1998: Central Arctic surface ocean environment during the past 80,000 years, *Paleoceanography*, **13**, 193–204.

Owens, W. and P. Lemke, 1990: Sensitivity studies with a sea ice-mixed layer-pycnocline model in the Weddell Sea, *Journal of Geophysical Research*, **95** (C6), 9527–9538.

Pacanowski, R., 1995: *MOM 2 Documentation: Users Guide and Reference Manual ver 1.0*, GFDL Ocean Group, NOAA/Geophysical Fluid Dynamics Laboratory, Princeton, NJ., Technical Report No. 3.

Parkinson, C. and W. Washington, 1979: A large-scale numerical model of sea ice, *Journal of Geophysical Research*, **84** (C1).

Pereira, A. F., 2001: *Numerical investigation of tidal processes and phenomena in the Weddell Sea, Antarctica*, Ph.D. thesis, Universität Bremen, Bremen, Germany.

Perovich, D. K., E. L. Andreas, J. A. Curry, H. Eicken, C. W. Fairall, T. C. Grenfell, P. S. Guest, J. Intrieri, D. Kadko, R. W. Lindsay, M. G. McPhee, J. Morison, R. E. Moritz, C. A. Paulson, W. S. Pegau, P. O. Persson, R. Pinkel, J. A. Richter-Menge, T. Stanton, H. Stern, M. Sturm, W. B. Tucker III and T. Uttal, 1999: Year on ice gives climate insights, *Eos, Transactions*, **80** (41), 481,485–486.

Polyak, L., M. H. Edwards, B. J. Coakley and M. Jakobsson, 2001: Ice shelves in the Pleistocene Arctic Ocean inferred from glaciogenic deep-sea bedforms, *Nature*, **410**, 453–457.

Prange, M., 2003: *Einfluß arktischer Süsswasserquellen auf die Zirkulation im Nordmeer und im Nordatlantik in einem prognostischen Ozean-Meereis-Modell*, Ph.D. thesis, Universität Bremen, Bremen, Germany.

Preller, R., 1994: Navy sea ice forecasting system: past, present, and future, in *Sea ice observation and modelling*, Z. Yu et al., eds., China Ocean Press, Beijing, China.

Proshutinsky, A. and M. Johnson, 1997: Two circulation regimes of the wind-driven Arctic ocean, *Journal of Geophysical Research*, **102** (C6).

Ronski, S., 2002: *Ventilation der Grönlandsee*, Ph.D. thesis, Universität Bremen, Bremen, Germany, published by Alfred Wegener Institute: Berichte zur Polar- und Meeresforschung, **444**, 2003.

Semtner, A., 1976: A model for the thermodynamic growth of sea ice in numerical investigations of climate, *Journal of Physical Oceanography*, **6** (3), 379–389.

Smedsrud, L. and T. Furevik, 2000: Towards an ice-free Arctic?, *Cicerone*, **2**.

Smith, D., 1988: Coefficients for sea surface wind stress, heat flux, and wind profiles as a function of wind speed and surface temperature, *Journal of Geophysical Research*, **93** (C12), 15467–15472.

Smolarkiewicz, P., 1983: A simple positive definite advection scheme with small implicit diffusion, *Monthly Weather Review*.

Spielhagen, R. F., G. Bonani, A. Eisenhauer, M. Frank, T. Frederichs, H. Kassens, P. W. Kubik, N. Nørgaard-Pedersen, N. R. Nowaczyk, A. Mangini, S. Schäper, R. Stein, J. Thiede, R. Tiedemann and M. Wahsner, 1997: Arctic Ocean evidence for late quaternary initiation of northern Eurasian ice sheets, *Geology*, **25** (9), 783–786.

Steffen, K., J. Key, D. J. Cavalieri, J. Comiso, P. Gloersen, K. St. Germain and I. Rubinstein, 1992: The estimation of geophysical parameters using passive microwave algorithms, in *Microwave remote sensing of sea ice*, F. Carsey, ed., Geophysical Monograph 68, pp. 201–231, American Geophysical Union.

Steiner, N., 1998: *Nutzung der Meereisrauhigkeit zur Validierung und Optimierung eines großkaligen Meereismodells für die Arktis*, Ph.D. thesis, Christian-Albrechts-Universität, Kiel, Germany.

Thiede, J. et al., 2002: POLARSTERN ARKTIS XVII/2 Cruise Report: AMORE 2001 (Arctic Mid Ocean Ridge Expedition), Tech. rep., Alfred-Wegener-Institut for Polar and Marine Research, Bremerhaven, Germany.

Tucker, W. B., D. K. Perovich, A. J. Gow, W. F. Weeks and M. R. Drinkwater, 1992: Physical properties of sea ice relevant to remote sensing, in *Microwave remote sensing of sea ice*, F. Carsey, ed., Geophysical Monograph 68, pp. 9–28, American Geophysical Union.

Walsh, J. E., D. Portis and W. L. Chapman, 1998: An assessment of realanysis-derived surface fluxes in the Arctic, in *Proceedings of the First WCRP International Conference on Reanalyses*, WCRP-104.

Wang, J., R. Kwok, F. J. Saucier, J. Hutchings, M. Ikeda, W. Hibler III, J. Haapala, M. D. Coon, M. Meier, H. Eicken, N. Tanaka, D. Prentki and W. Johnson, 2003: Working toward improved small-scale sea ice-ocean modeling in the Arctic Seas, *Eos, Transactions*, **84** (34).

Zhang, J., D. R. Thomas, D. A. Rothrock, R. W. Lindsay and Y. Yu, 2003: Assimilation of ice motion observations and comparisons with submarine ice thickness data, *Journal of Geophysical Research*, **108** (C6), 3170, doi:10.1029/2001JC001041.

Zillman, J., 1972: A study of some aspects of the radiation and heat budgets of the Southern Hemisphere oceans, in *Meteorological study*, vol. 26, p. 526 pp., Bureau of Meteorology, Dept. of the Interior, Canberra, Australia.

Zyryanov, D. and R. Korsens, 2002: A numerical model for simulation of sea ice destruction due to external stress in geoscale areas, in *Proceedings of the* 1st *International PFC-Symposium on Numerical Modeling in Micromechanics via Particle Methods*, H. Konietzky, ed., Gelsenkirchen, Germany, CD-ROM publication, ISBN 90-5809-5230.

Thanks

The Alfred Wegener Institute for Polar and Marine Research (AWI) provided a very helpful organizational framework for the preparation of this work.

Among all the people who have supported me during the time working on this thesis and therefore contributing directly or indirectly to the success I'd like to express my special gratitude to:

- Prof. Ernst Augstein for offering the opportunity to prepare this PhD thesis,

- Prof. Peter Lemke for taking over the supervision, helpful comments during the evolution of this work and support in every regard,

- Prof. Klaus Künzi for examining my work,

- Dr. Josef Kolatschek for introducing me to the numerical model,

- Dr. Christian Haas for countless helpful discussions and teaching me sea ice in its natural environment,

- Dr. Tilo Schöne for providing the RA data,

- all the people at and associated with Haus F for offering their scientific know-how, especially the members of SIG, MAD and BRIOS, and Dr. Bernadette Fritzsch,

- Frank, Jill, Karen, Kirsten, Martin, Michael, and Robert for reading parts of the manuscript,

- and my family and friends for all the faith and support that I demanded.